INELASTIC NEUTRON SCATTERING AND COMPUTER SIMULATIONS OF SUPERIONIC AND LASER HOST MATERIALS

By

PRABHATASREE GOEL

Enrolment No. PHYS012008014

Bhabha Atomic Research Centre, Mumbai, India

A thesis submitted to the

Board of Studies in Physical Sciences

In partial fulfillment of requirements

For the Degree of

DOCTOR OF PHILOSOPHY

Of

HOMI BHABHA NATIONAL INSTITUTE

August 2014

HOMI BHABHA NATIONAL INSTITUTE

Recommendation of the Viva Voce Board

As members of the Viva Voce Board, we certify that we have read the dissertation prepared by Smt. Prabhatasree Goel entitled "Inelastic Neutron Scattering and Computer Simulations of Superionic and Laser Host Materials" and recommended that it may be accepted as fulfilling the dissertation requirement for the Degree of Doctor of Philosophy,

____ Date: 13th May, 2015
Chairman- Prof. S. L. Chaplot

____ Date: 13th May, 2015
Guide- Prof. R. Mittal

____ Date: 13th May, 2015
External Examiner- Prof. Priya Mahadevan

____ Date: 13th May, 2015
Member-1: Prof. S. M. Sharma

____ Date13th May, 2015
Member-2: Prof. A. K. Arora

Final approval and acceptance of this dissertation is contingent up on the candidate's submission of the final copies of the dissertation to HBNI.

I hereby certify that I have read this dissertation prepared under my direction and recommend that it may be accepted as fulfilling the dissertation requirement.

Date: 13/05/2015

Place: Mumbai

Guide: R. Mittal

STATEMENT BY AUTHOR

This dissertation has been submitted in partial fulfillment of requirements for an advanced degree at Homi Bhabha National Institute (HBNI) and is deposited in the Library to be made available to borrowers under rules of the HBNI.

Brief quotations from this dissertation are allowable without special permission, provided that accurate acknowledgement of source is made. Requests for permission for extended quotation from or reproduction of this manuscript in whole or in part may be granted by the Competent Authority of HBNI when in his or her judgment the proposed use of the material is in the interests of scholarship. In all other instances, however, permission must be obtained from the author.

(Prabhatasree Goel)

DECLARATION

I, hereby declare that the investigation presented in the thesis has been carried out by me. Whenever contributions of others are involved, every efforts is made to indicate this clearly with due reference to the literature and acknowledge of collaborative research and discussions. The work is original and has not been submitted earlier as a whole or in part for a degree / diploma at this or any other Institution / University.

(Prabhatasree Goel)

Declaration

I, hereby certify that the queries raised by the examiners of the thesis have been incorporated as suggested.

R.Mittal

(Guide)

List of Publications:

[1] Superionic behavior of lithium oxide Li_2O: A lattice dynamics and molecular dynamics study

Prabhatasree Goel, Narayani Choudhury and S. L. Chaplot

Phys. Rev. **B**70, 174307, (2004).

[2] Fast ion diffusion, superionic conductivity and phase transitions of the nuclear materials UO_2 and Li_2O

Prabhatasree Goel, N. Choudhury and S. L. Chaplot

J. Phys.: Condensed. Matter **19,** 386239 (2007).

[3] Atomistic modeling of the vibrational and thermodynamic properties of uranium dioxide, UO_2

Prabhatasree Goel, N. Choudhury and S. L. Chaplot

J. Nucl. Materials **377,** 438 (2008).

[4] Lattice dynamics of strontium tungstate

Prabhatasree Goel, R. Mittal, S.L.Chaplot and A. K. Tyagi

Pramana **71**, 1135 (2008)

[5] Fast ion diffusion, superionic conductivity and phase transitions of the nuclear materials UO_2 and Li_2O

Prabhatasree Goel, Choudhury N. and S. L. Chaplot

Trans. Indian Inst. Of Metals **62,** 141 (2009)

[6] Lattice dynamics and Born instability in yttrium aluminum garnet, $Y_3Al_5O_{12}$

Prabhatasree Goel, R .Mittal, N. Choudhury and S. L. Chaplot

J. Phys. Condensed Matt. **22,** 065401 (2010).

[7] Inelastic neutron scattering and theoretical studies on strontium tungstate, $SrWO_4$

Prabhatasree Goel, R. Mittal, M. K. Gupta, Mala N. Rao, S. L. Chaplot, S. Rols, A. K. Tyagi and Z. Petr

Chin. J. of Phys. **49**, 308 (2011).

[8] Phonon instability and mechanism of superionic conduction in Li_2O

M. K. Gupta, **Prabhatasree Goel**, R. Mittal, N. Choudhury and S. L. Chaplot

Phys. Rev. B **85,** 184304 (2012).

[9] Phonons, Lithium Diffusion and Thermodynamics of $LiMPO_4$ (M=Mn, Fe)

Prabhatasree Goel, M. K. Gupta, R. Mittal, S. Rols, S. J. Patwe, S. N. Achary, A. K. Tyagi and S. L. Chaplot

J. Mater. Chem. A **2,** 14729 (2014)

[10] Inelastic Neutron Scattering Studies of Phonon Spectra and Simulations in Tungstates, AWO_4 (A = Ba, Sr, Ca and Pb)

Prabhatasree Goel, M. K. Gupta, R. Mittal, S. Rols, S. N. Achary, A. K.Tyagi and S. L. Chaplot

Phys. Rev. B **91**, 094304 (2015)

Note: The thesis will be based on 2,3,4,5,6,7 and parts of papers 8,9 and 10. The parts involving DFT calculations in papers 8,9 and 10, presented in these papers are not included.

Conference Papers:

[1] Molecular Dynamics simulations of strontium and barium Tunstate

Prabhatasree Goel, R. Mittal and S. L. Chaplot

AIP Conf. Proc. **1313**, 328 (2010)

[2] Inelastic neutron scattering, Lattice dynamics and high pressure stability of $LuVO_4$

Prabhatasree Goel, R. Mittal, S. L. Chaplot and C. K. Loong

AIP conf. Proc. **1349**, 141 (2011)

[3] Dynamics of Plutonium dioxide

Prabhatasree Goel, R. Mittal and S. L. Chaplot

AIP Conf. Proc. **1447**, 79 (2012)

[4] High pressure phase transitions in barium tungstate

Prabhatasree Goel, R. Mittal and S. L. Chaplot

J. Phys.: Conf. Series, **377**, 012094 (2012)

Dedicated

To

My Beloved Parents

"Thanthaiyum Thayum Munnari Deivam"

(Who taught me that knowledge is a virtue,

which is never lost)

Acknowledgements

I would like to extend my sincere gratitude to Dr. S. L. Chaplot, Director, Physics Group, BARC for his guidance and critical assesment. I wish to thank Dr. R. Mittal, my guide, for his constant support, suggestions, keen interest, advice and monitoring of my progress. Many thanks are due to Dr. Narayani Choudhury, who gave some invaluable advice during my formative years. I would like to thank Mr. Mayank Gupta, my co-author in several papers for various fruitful discussions on topics very relevant to my work. I thank Dr. (Smt.) Mala N. Rao, Dr. S. K. Mishra, and all my colleagues and friends, who have extended help graciously on several occasions.

I thank my collaborators, Dr. S. Rols (ILL, Grenoble), Dr. C. K. Loong (ANL, USA), Dr. A. K. Tyagi, Dr. S. N. Achary (BARC) and Dr. Z. Petr (Russian Academy of Sciences).

My work would not have been possible without the unflinching support of my family. I wish to extend my heartfelt thanks to my husband, Shri. Vikas Goel. He has been a pillar of support, his critical suggestions and observations have enhanced the quality of my work. My daughter Tanya and son Aditya have been my inspiration, the smile on their faces made all the hard work enjoyable. I extend my special thanks to my in-laws, Shri. H. C. Goel, and Smt. Veena Goel. I wish to thank my loving sister, Ms. Anupama Raghu for her constant encouragement, for boosting my morale whenever I felt lost or forlorn. Finally, I wish to thank my parents, Shri. K. T. Narasimhan and Smt. Radha Narasimhan for their blessings, unconditional love and unwavering confidence in me. What I am today is due to them.

CONTENTS

PAGE NO.

Homi Bhabha National Institute

Ph.D. Programme

1. **Name of the Canditate : Prabhatasree Goel**
2. **Name of the constitutent Institution : Bhabha Atomic Research centre**
3. **Enrolment No. : PHYS01200804014**
4. **Title of the thesis : Inelastic Neutron Scattering and Computer Simulations of Superionic and Laser Host Materials**
5. **Board of studies : Physical Sciences**

SYNOPSIS

The study of atomic motions in a crystalline solid has always been a subject of interest. The knowledge of the average positions of atoms can explain a large number of electronic properties, material hardness, optical properties to name a few. However, macroscopic material properties like specific heat, thermal expansion, phase transitions and thermal conductivity have their origin in the vibrations of atoms in solids. Therefore it is important to describe the dynamics of the crystal lattice. These motions are not random; rather they are determined by the forces that atoms exert on each other. The collective motions of atoms in solids form travelling waves (called lattice vibrations), which are quantized in terms of “phonons”. Developing suitable lattice dynamics models in conjunction with inelastic neutron scattering experiments is highly desirable to characterise various types of solids. This is the essence of the subject of lattice dynamics.

On the experimental front, lattice vibrations are studied using myriad of techniques; namely, Raman Spectroscopy, infrared absorption (IR), Brillouin scattering, inelastic x-ray and neutron scattering. Raman and IR techniques provide direct measurements of only selected long wavelength phonons through one-phonon processes. On the other hand, inelastic x-ray and neutron scattering facilitate measurements of the phonons in the entire Brillouin zone, thereby enabling the study of phonon dispersion relations and density of states.

Owing to practical limitations, experimental studies at high temperatures and pressures may often be limited. In such cases, it is imperative that there is capability of predicting material properties under these extreme conditions. For this purpose, accurate theoretical models for exploring the entire spectrum of thermal vibrations of crystals using lattice dynamical methods are necessary. The usefulness of these models depends on their ability to explain the microscopic dynamical properties, which includes crystal structure, equation of state, phonon dispersion relations, and density of states. The data obtained from experimental techniques are used to test and validate the models of interatomic potentials. Once validated successfully, these models may further be used to predict the thermodynamic properties at high temperatures and pressures. This acquired knowledge would help other researchers working to utilize these materials in technological applications.

The author has developed models of interatomic potentials for several technologically useful compounds. These potentials have been used to compute the structural and dynamical properties under varying conditions. Using the interatomic potentials developed, molecular dynamics simulations were carried out to understand diffusion with increasing temperature and response of compound to compression. To augment the theoretical results, the author has also carried out inelastic neutron scattering experiments on single crystal and powder samples at Dhruva reactor, Trombay (India). With the help of collaborators, phonon density of states has been measured at other international neutron scattering instruments at Institut Laue Langevin, France and at Intense Pulsed Neutron Source, IPNS (USA). The author has also contributed in some instrument development work under neutron scattering programme at Dhruva reactor.

The thesis consists of six chapters. The motivation for studying the various compounds, details of the work done and the significance of the results obtained are given below in the brief description of various chapters.

Chapter 1 describes the theory of lattice dynamics and molecular dynamics simulations. The technique of inelastic neutron scattering has been described and basics of lattice dynamics and computation of thermodynamic properties of a solid have been explained. Lattice dynamical calculations of phonons may be carried out using either a quantum-mechanical *ab-initio* approach or an atomistic approach involving semiempirical interatomic potentials. This work pertains mainly to the latter approach. For small motions of atoms about their equilibrium positions, the atomic dynamics determined in the harmonic approximation is entirely specified by the second derivatives of the crystal potential. The symmetry of the crystal is the constraint which should be consistent with the model developed. The lattice dynamical calculations have been exploited to derive the high temperature thermodynamic properties and high pressure behavior of solids. The formulated interatomic potentials were further used to understand the time evolution of the compounds at different temperature and pressure using molecular dynamics simulations. Inelastic neutron scattering is best suited to study the phonon behavior of solids. The wavelength of the thermal neutrons is comparable to the interatomic distances in a crystal, and energies are also of the same order as the energy of the quantized lattice vibrations. The relation of the phonon frequencies with wave vector in a crystal is a complex one, and is called the phonon dispersion relation. On the other hand the overall frequency distribution of all the phonons in a crystal is given by the phonon density of states. Single crystals provide information of the phonon dispersion relation while polycrystalline samples give information of the phonon density of states. The experimental measurements given in this thesis has been carried out on steady state reactors as well as pulsed sources.

Chapter 2 describes our studies on superionic nuclear oxides and battery materials. Superionic conduction in fluorite-structured (UO_2 and anti-fluorite Li_2O) oxides have applications in energy storage, conversion and in nuclear industry. Fast ion conductors exhibit high ionic conductivity, whilst in solid condition, and belong to the class of superionics, which allow macroscopic movement of ions through their structure. This behavior is characterized by the rapid diffusion of a significant fraction of one of the constituent species (Li in case of Li_2O

and O in case of UO_2) within an essentially rigid framework formed by the other species. We report a cumulative study of these oxides in its normal as well as superionic phase using both lattice dynamical and molecular dynamical calculations. Lattice dynamical calculations have been done using a shell model in the quasi-harmonic approximation. We have calculated the equilibrium structure, phonon frequencies, the elastic constants, phase transitions and the specific heat, which are in excellent agreement with the available experimental data. We also predict the pressure variation of the phonon dispersion and the equation of state. The results obtained for the diffusion constant and the thermal amplitude of diffusing atoms are in very good agreement with experimental observations. The pair correlation functions, bond angle distribution and snapshots of the positions of lithium atoms over a range of time-steps, provide a microscopic picture of the local structure indicating that as in other fluorites, in case of Li_2O, the lithium ions diffuse via an interstitial mechanism but the distortions due to this movement are small. The calculated transition temperature of UO_2 is 2300 K, which compares well with experimental value of about 2600 K, while in case of Li_2O, the values are 1000 K and 1200 K respectively. At the transition temperature, diffusing atoms's diffusion coefficient is comparable to that of a liquid and is in the order of 10^{-9} m^2/s. The possible role of phonon in initiation of diffusion has also been studied in Li_2O. It is found that in the superionic regime lithium atoms may exhibit macroscopic movement along (100) direction. It can be seen that microscopic modeling or simulation is found to play a pivotal role in understanding the conduction processes at high temperatures in crystals.

Lithium transition metal phospho-olivines are useful electrode materials, owing to their stability, high safety, low cost and cyclability. Recently phonon studies and thermodynamics of $LiMPO_4$ (M=Mn, Fe) has been carried out to understand the microscopic picture of Li sub-lattice. The inelastic neutron scattering measurements at ambient conditions are in good agreement with the calculated phonon spectra using a potential model, thus validating the accuracy of the model parameters. Molecular dynamics simulations indicate large mean square displacement of Li as compared to other constituent atoms. The computed pair-correlations between various atom pairs show that there is local disorder occurring in the lithium sub-lattice with increasing temperature, while other pairs show minimal changes. The results find the two compounds to be thermally stable up to high temperatures, which is a desirable trait for its battery applications.

Chapter 3 deals with the detailed study of the lattice dynamics and high pressure behavior (Born instability) of aluminum-based synthetic garnets (YAG) ($Y_3Al_5O_{12}$, $Yb_3Al_5O_{12}$, $Lu_3Al_5O_{12}$). Yttrium Aluminum Garnet ($Y_3Al_5O_{12}$) and rare earth doped garnets are important solid-state laser host materials. Nd doped YAG has wide spread use in commercial, medical, military and industrial applications. Lattice dynamics calculations of various microscopic and macroscopic vibrational and thermodynamic properties of YAG, as a function of pressure upto 100 GPa and temperature upto 1500K has been carried out. Garnet has a complex structure with several interconnected dodecahedrons, octahedrons and tetrahedrons. Unlike other aluminosilicate garnets, there are no distinct features to distinguish between intramolecular and intermolecular vibrations of the crystal. At ambient pressure, low energy phonons involving mainly the vibrations of yttrium atoms play a primary role in the manifestations of elastic and thermodynamic behavior. The aluminum atoms in tetrahedral and octahedral coordination are found to be dynamically distinct. Garnet's stability can be discerned from the response of its phonon frequencies to increasing pressure. The dynamics of both octahedral and tetrahedral aluminum atoms undergo radical changes under compression which have an important bearing on their high pressure and temperature properties. At 100 GPa, these garnets develop a large phonon band gap (90-110 meV) and its microscopic and macroscopic physical properties are found to be profoundly different from that at ambient pressure phase. There are significant changes in the high pressure thermal expansion and specific heat. The mode Gruneisen parameters show significant changes in the low energy range with pressure. The studies show that the YAG structure becomes mechanically unstable around P = 108 GPa due to the violation of the Born stability criteria. Although this does not rule out thermodynamic crossover to a lower free energy phase at lower pressure, this places an upper bound of P = 110 GPa for the mechanical stability of YAG. Other garnets studied exhibit similar behavior.

Chapter 4 deals with the inelastic neutron scattering studies, lattice dynamics and molecular dynamics simulations on alkaline earth tungstates and vanadates (AWO_4: A=Sr, Pb, Ba, Ca and $LuVO_4$). Alkaline–earth tungstates are important for their scientific and technological applications. These compounds find their use in solid- state scintillators and optoelectronic devices. Alkaline-earth tungstates exhibit an interesting phase diagram with respect to pressure. These compounds are found to undergo pressure-driven phase transitions around 10 GPa, from tetragonal scheelite structure to monoclinic fergusonite structure. Transferable interatomic potentials have been formulated and validated by the measured inelastic neutron scattering data on all the 5 above said compounds. Phonon dispersion relation of low energy acoustic branches of $SrWO_4$ have been measured along (100) and (001) using TAS, Dhruva. The evolution of these compounds with increasing pressure has been studied using molecular dynamics simulations. In our calculations there is no evident volume discontinuity at the scheelite to fergusonite transformation. The pair correlation between various atoms has been computed. These studies indicate that in $SrWO_4$ pressure induced amorphization occurs at about 36 GPa, at 40 GPa in $PbWO_4$, 32 GPa in $CaWO_4$ and 47 GPa in $BaWO_4$. These results are in excellent agreement with reported amorphizaiton at 45 GPa in $BaWO_4$ and around 40 GPa in $CaWO_4$. The intratetrahedral bond angle distribution O-W-O in $BaWO_4$ shows that until amorphization there is no change in the WO_4 tetrahedra, beyond it changes. The pair correlation functions show that there are subtle changes in the arrangement of the AO_8 polyhedra with increasing pressure. However, the WO_4 tetrahedra remain unperturbed with increasing pressure until amorphization occurs. On amorphization, WO4 tetrahedra deforms, W's coordination increases, while AO_8 polyhedra shows considerable distortion.

Inelastic neutron scattering, lattice dynamics calculations and relative high pressure stability of $LuVO_4$ has been studied. At ambient conditions this compound crystallizes in a body-centred tetragonal unit cell of zircon phase (space group $I4_1/amd$). A transferable interatomic potential has been developed to study the lattice dynamics and model the experimentally obtained phonon density of states in $LuVO_4$. The parameters of the theoretical interatomic potential have been fitted with respect to experimentally available Raman and infrared frequencies and equilibrium structure. The stability of the zircon structure at ambient temperature with increasing pressure has been studied. Zircon phase goes into a scheelite phase ($I4_1/a$) at around 8 GPa which is in excellent agreement with reported value of 7.9 GPa.

Apart from the above said research works, the author has also contributed to certain instrumentation activities in the neutron scattering progamme at Dhruva reactor, Trombay. **Chapter 5 describes these activities briefly.** The author was involved in the assembling of a monchromator setup with vertical and horizontal focusing for the Triple Axis Spectrometer at Dhruva, Trombay. For the purpose of the monochromator assembly, as acquired perfect single crystals of copper were pressure treated to increase their mosaic spread to up to abour 0.5. These crystals were then subsequently mounted on the assembly and aligned to give good intensity.

The summary and prelude to the future directions based on this thesis work is given in Chapter 6. The gist of this thesis is that a combination of lattice dynamics calculations, molecular dynamics simulations and inelastic neutron scattering measurements can be successfully utilized to study phonons in solids and their manifestations in macroscopic properties like specific heat, thermal expansion, diffusion and equation of state. The calculations have greatly aided the planning and execution of the various experimental measurements. The interatomic potentials have been used to understand the behavior of phonons at extreme conditions and the role of phonons in anamolous behavior of solids like superionic conductors at elevated temperatures. The calculations enabled to understand the microscopic picture of the dynamics in various solids leading to the manifestations of several unique properties. The experience gained from the study of superionic conductors and their behavior with temperature will be of immense help in understanding the physics of several technologically useful battery materials, wherein the phenomena of diffusion plays an important role. The experience gained while working on instrument development would be worthwhile during future endeavors.

List of Figures

List of Tables

Chapter 1

Theory and experimental techniques

1.1 INTRODUCTION

Periodic arrangement of atoms distinguishes crystalline solids from other states of matter. Historically, crystal lattices were always assumed to be completely rigid, atomic displacements away from the equilibrium positions were not envisaged. Although, a completely rigid lattice violates the uncertainty principle, it still could explain a wide range of solid-state properties, like electronic structure, nature and strength of chemical bonding, to name a few. The underlying reason was that internal energy of a solid U is a sum of E^s and E^v, where E^s is the electronic ground state energy (static) of the fixed lattice, while E^v is the additional energy (vibrational) due to lattice motion. Since generally, $E^s >> E^v$, many properties satisfactorily understood by simply neglecting the vibrational contribution [1].

Now, classically it is known that when a system of particles in a stable equilibrium is disturbed, it performs certain vibrations, such that every particle remains in the neighborhood of its equilibrium position. Hence, in order to study solids at microscopic level, one needs to know the average positions and dynamics of atoms. Many important physical properties like phase transitions, thermal expansion, specific heat and thermal conductivity have their origin in the dynamics of atoms [2-5]. Vibrational modes of a crystal are called phonons. In other words, phonons are quanta of lattice vibrations. The phonons are characterized by three parameters, namely, their wave vector, energy and polarization vector. The polarization vector defines the relative atomic vibrations along three orthogonal directions. These atomic motions are not random, and are determined by the forces that atoms exert on each other. This energy-wavelength relation of the thermal motions of the atoms is the essence of lattice dynamics.

Experimental studies of lattice vibration include techniques like Raman spectroscopy, infrared absorption, inelastic neutron scattering (INS), inelastic X-ray scattering, etc. Raman and infrared (IR) spectroscopy are complementary to neutron scattering. INS and complementary techniques such as Raman and infrared (IR) spectroscopy provide some of the most valuable tools in assessing models of material properties. Inelastic neutron and inelastic X-ray scattering [6,7] can directly probe the phonons in the entire Brillouin zone, whereas optical techniques probe only the the long wavelength optically active phonons.

Experimental studies at high pressures and temperatures are often limited and accurate models for theoretical studies of various materials are of utmost importance. Applicability of an interatomic model for a given substance is solely dependent on its ability to successfully explain a variety of microscopic dynamical properties, crystal structure, equation of state etc [1,8]. The data obtained from neutron scattering and optical experiments are used to test and validate models of interatomic potentials [1,8], which in turn could be used to predict thermodynamic properties at high pressures and temperatures.

A combination of lattice dynamical calculation, molecular dynamics calculation and neutron inelastic scattering is used to study phonons in a variety of oxides. The experiments provide valuable information about the phonon dispersion relation and density of states, while the models enable microscopic interpretation of the experimental data. The materials studied are useful nuclear oxides, superionic oxides, battery materials and laser host materials.

This chapter has been organized as follows: The theoretical formalism of lattice dynamics and thermodynamic properties of a solid are given in section 1.2. The details about the computational techniques are put forth in section 1.3. Formalism and computational details of molecular dynamics is described in section 1.4. Theory and details about the experimental techniques for inelastic neutron scattering are described in sections 1.4 and 1.5, respectively. Section 1.6 deals with details of molecular dynamics simulations and finally section 1.7 explains the motivation for carrying out these studies.

1.2 LATTICE DYNAMICS AND THERMODYNAMIC PROPERTIES OF SOLIDS

1.2.1 Theoretical formalisms

Born-Oppenheimer or adiabatic approximation is the basis for the formalism of lattice dynamics. As nuclei are several thousand times heavier than electrons, they follow nuclear motion adiabatically. Hence, electrons essentially contribute an additional effective potential for nuclear motion. Therefore, lattice vibrations are associated only with nuclear motion. In this Chapter only summary of the mathematical formalism for a perfect crystal is described. A complete account of the formal theory of lattice dynamics can be found in literature [2-4]. For small displacements of the atoms $\mathbf{u}\begin{pmatrix} \mathrm{l} \\ \mathrm{k} \end{pmatrix}$ about their equilibrium positions $\mathbf{r}\begin{pmatrix} \mathrm{l} \\ \mathrm{k} \end{pmatrix}$(where, l denotes the l^{th} unit cell (l= 1, 2,….N) and k is the k^{th} type of atom (k=1,2,…..n) within the unit cell), the crystal potential energy can be written as a Taylor expansion. The expansion is retained only up to the second derivative in the so called harmonic approximation, as follows:

$$\phi = \phi_0 + \phi_1 + \phi_2 \qquad (1.1)$$

where

$$\phi_0 = \phi\left(\boldsymbol{r}\begin{pmatrix} l \\ k \end{pmatrix}\right)$$

$$\phi_1 = \sum_{lk\alpha} \left.\frac{\partial \phi}{\partial u_\alpha\begin{pmatrix} l \\ k \end{pmatrix}}\right|_o u_\alpha\begin{pmatrix} l \\ k \end{pmatrix}$$

$$= \sum_{lk\alpha} \phi_\alpha\begin{pmatrix} l \\ k \end{pmatrix} u_\alpha\begin{pmatrix} l \\ k \end{pmatrix}$$

$$\phi_2 = \frac{1}{2}\sum_{lk\alpha}\sum_{l'k'\beta} \left.\frac{\partial^2\phi}{\partial u_\alpha\begin{pmatrix} l \\ k \end{pmatrix}\partial u_\beta\begin{pmatrix} l' \\ k' \end{pmatrix}}\right|_o u_\alpha\begin{pmatrix} l \\ k \end{pmatrix} u_\beta\begin{pmatrix} l' \\ k' \end{pmatrix}$$

$$= \frac{1}{2}\sum_{lk\alpha}\sum_{l'k'\beta} \phi_{\alpha\beta}\begin{pmatrix} l & l' \\ k & k' \end{pmatrix} u_\alpha\begin{pmatrix} l \\ k \end{pmatrix} u_\beta\begin{pmatrix} l' \\ k' \end{pmatrix}$$

where the suffices α and β denote Cartesian coordinates.

In the equilibrium configuration, the force on every atom must vanish. This lead to the result

$$\phi_\alpha\begin{pmatrix} l \\ k \end{pmatrix} = 0 \quad \text{for every } \alpha,\ k,\ l$$

Hence $\phi_1 = 0$

Thus in the harmonic approximation

$$\phi = \phi_0 + \frac{1}{2}\sum_{lk\alpha}\sum_{l'k'\beta} \phi_{\alpha\beta}\begin{pmatrix} l & l' \\ k & k' \end{pmatrix} u_\alpha\begin{pmatrix} l \\ k \end{pmatrix} u_\beta\begin{pmatrix} l \\ k' \end{pmatrix} \tag{1.2}$$

Accordingly, the equation of motion of the $(lk)^{th}$ atom becomes

$$m_k\, \ddot{u}_\alpha\begin{pmatrix} l \\ k \end{pmatrix} = -\sum_{l'k'\beta} \phi_{\alpha\beta}\begin{pmatrix} l & l' \\ k & k' \end{pmatrix} u_\beta\begin{pmatrix} l' \\ k' \end{pmatrix} \tag{1.3}$$

From (1.3) it is clear that $\phi_{\alpha\beta}\begin{pmatrix} l & l' \\ k & k' \end{pmatrix}$ is the negative of the force exerted on atom (lk) in the α direction due to unit displacement of the atom $(l'k')$ in the β direction. The quantity - $\phi_{\alpha\beta}$ is referred to as the force constant.

The crystal periodicity suggests that the solutions of eq (1.3) must be such that the displacements of atoms in different unit cells must be same apart from phase factor. The equations of motion (1.3) are solved by assuming wave like solutions of the type

$$u_\alpha\begin{pmatrix} l \\ k \end{pmatrix} = U_\alpha(k\,|\,\mathbf{q})\exp\{i(\mathbf{q}.\mathbf{r}\begin{pmatrix} l \\ k \end{pmatrix} - \omega(\mathbf{q})t\} \qquad (1.4)$$

Here **q** is the wave vector and $\omega(\mathbf{q})$, the angular frequency associated with the wave.

Substituting (1.4) in (1.3)

$$m_k\omega^2(\mathbf{q})U_\alpha(k\,|\,\mathbf{q}) = \sum_{k'\beta} D_{\alpha\beta}\begin{pmatrix} \mathbf{q} \\ kk' \end{pmatrix} U_\beta(k'\,|\,\mathbf{q}) \qquad (1.5)$$

where, m_k is the mass and $\mathbf{r}\begin{pmatrix} l \\ k \end{pmatrix}$ the position coordinate of the k^{th} atom.

Here, the dynamical matrix $D_{\alpha\beta}\begin{pmatrix} \mathbf{q} \\ kk' \end{pmatrix}$ is given by

$$D_{\alpha\beta}\begin{pmatrix} \mathbf{q} \\ kk' \end{pmatrix} = \sum_{l'} \phi_{\alpha\beta}\begin{pmatrix} l & l' \\ k & k' \end{pmatrix} \exp\{i(\mathbf{q}.[\mathbf{r}\begin{pmatrix} l' \\ k' \end{pmatrix} - \mathbf{r}\begin{pmatrix} l \\ k \end{pmatrix}])\} \qquad (1.6)$$

The 3n coupled equations of motion are obtained. As stated earlier, the adiabatic approximation is assumed wherein the electrons adiabatically follow the nuclear vibrations and provide an effective nuclear potential. However, this does not imply that the atoms are rigid during vibrations. The electric field set up by the displacements of the ions is modified by their electronic polarizibility which in turn modifies the force on them and affects the phonon frequencies. This may be described by a shell model [3,5], in which each ion is regarded to be composed of a rigid or non-polarizable core and a charged shell with effective charges X (k) and Y(k) respectively. The core and shell are connected by a harmonic spring constant K(k). Thus, the shell can be displaced relative to the core causing a dipole, which in turn leads to a proper description of dielectric behavior of the crystals. One can calculate the dynamical matrices between the pairs, core-core, core-shell, shell-core and shell-shell, denoted as D^{CC}, D^{CS}, D^{SC} and D^{SS}. We then have the following equations involving the displacement vectors associated with the core (U) and polarization (W).

$$m\omega^2 U = D^{CC}U + D^{CS}W \tag{1.7}$$

$$0 = D^{SC}U + D^{SS}W \tag{1.8}$$

Eliminating W, we get

$$m\omega^2 U = [D^{CC} - \{D^{CS}(D^{SS})^{-1}D^{SC}\}]U \tag{1.9}$$

and one obtains the dynamical matrix

$$D = D^{CC} - D^{CS}(D^{SS})^{-1}D^{SC} \tag{1.10}$$

For simplicity, the short-range forces between atoms are included only between the shells. The frequencies of the normal modes and eigenvectors are determined by diagonalizing the dynamical matrix through a solution of the secular equation

$$\det|\, m_k \omega^2(\mathbf{q})\ \delta_{kk'}\delta_{\alpha\beta} - D_{\alpha\beta}\begin{pmatrix}\mathbf{q}\\ kk'\end{pmatrix}| = 0 \tag{1.11}$$

Solving eq (1.11) 3n eigen values are obtained which are $\omega_j^2(\boldsymbol{q})$, (j=1,2,…,3n). Because, the dynamical matrix is Hermitian, the eigen frequencies are real and its eigen vectors may be chosen as orthonormal. The components of the eigen vectors $\xi_j(\mathbf{q})$ determine the pattern of displacement of the atoms in a particular mode of vibration.

The displacements of the atoms in one of these normal modes, labeled by (**q**j), correspond to a wave like displacement of atoms and are given by

$$u_\alpha\begin{pmatrix}l\\ k\end{pmatrix} = \xi_\alpha(k\,|\,\mathbf{q}j)\exp\{i(\mathbf{q}.\mathbf{r}\begin{pmatrix}l\\ k\end{pmatrix}\}P\begin{pmatrix}\mathbf{q}\\ j\end{pmatrix} \tag{1.12}$$

where, $P\begin{pmatrix}\mathbf{q}\\ j\end{pmatrix}$ is the normal coordinate and $\xi_\alpha(k\,|\,\mathbf{q}j)$ is the normalized eigenvector of the normal mode (**q**j), where j runs from 1 to 3n and is used to distinguish between the 3n normal modes at **q**. Corresponding to every direction in **q**-space, there are 3n curves $\omega=\omega_j(\mathbf{q})$, (j=1,2,…3n). Such curves are called phonon dispersion relations. The index j, which distinguishes the various frequencies corresponding to the propagation vector, characterizes various branches of the dispersion relation. Though, some of these branches are degenerate because of symmetry, in general they are distinct. The form of dispersion relation depends on the crystal structure as well as on the nature of the interatomic forces. However, a cyclic crystal always has three zero frequency modes at $\boldsymbol{q}$=0, which correspond to lateral translation of the crystal along three mutually perpendicular directions. These three branches are referred to as acoustic branches. The remaining (3n-3) branches have finite frequencies at $\boldsymbol{q}$=0, which are labeled as optic branches.

The centre to the lattice-dynamical problem therefore is to calculate the dynamical matrix, which is usually done by constructing a suitable model for the force constants or by using a suitable crystal potential. Corresponding to the 3n degrees of freedom for any wave vector **q**, there are 3n eigenvectors each having 3n components. Group-theoretical analysis at various high-symmetry points and directions in the Brillouin zone are used to derive the symmetry vectors for block diagonalization of the dynamical matrix. This allows the classification of the phonon modes into different irreducible representations enabling direct comparison with single crystal Raman, infrared and neutron data.

The phonon density of states is defined by the equation

$$g(\omega) = D' \int_{BZ} \sum_{j} \delta(\omega - \omega_j(\mathbf{q}))d\mathbf{q} = D' \sum_{jp} \delta(\omega - \omega_j(\mathbf{q}))\, d\mathbf{q}_p \tag{1.13}$$

where D' is a normalization constant such that $\int g(\omega)d\omega = 1$; that is, $g(\omega)d\omega$ is the ratio of the number of eigen states in the frequency interval $(\omega, \omega + d\omega)$ to the total number of eigenstates. 'p' is the mesh index characterizing **q** in the discretized irreducible Brillouin zone and $d\mathbf{q}_p$ provides the weighting factor corresponding to the volume of p^{th} mesh in **q**-space.

1.2.2 Thermodynamic Properties of solids

The formalism discussed in the previous section calculated phonon energies in the harmonic approximation. But this approximation [3-5] does not allow for thermal expansion, hence cannot account for the increase in specific heat beyond the value $3Nk_B$

with increasing temperature, multiphonon process etc. The number of phonons excited in thermal equilibrium at any temperature is given by Bose-Einstein distribution

$$n(\omega)\left[=\frac{1}{\exp(\hbar\omega/k_BT)-1}\right]$$

At high temperatures, $\hbar\omega_j(\mathbf{q}) \ll k_BT$, the number of phonons in a given state is directly proportional to the temperature and inversely proportional to their energy. Anharmonic effects are relatively small at low temperature. These effects become more important at high temperatures. This change at high temperatures affects physical properties of the crystal. In the quasiharmonic approximation [3-5], (where, the vibrations of atoms at any finite temperature are assumed to be harmonic about their mean positions appropriate to the corresponding temperature), the thermodynamic properties of a crystal are based on the averages of energies associated with the 3nN vibrations corresponding to the number of degrees of freedom of the n atomic constituents in the N unit cells of the crystal.

Using statistical thermodynamics any thermodynamic quantity can be obtained from the partition function, Z, which when evaluated in terms of the eigen energies is defined as.

$$Z=\exp\left(\frac{-\phi(V)}{k_BT}\right)\prod^{\mathbf{q}j}\frac{\exp\{\frac{-\hbar\omega_j(\mathbf{q})}{k_BT}\}}{1-\exp\{\frac{-\hbar\omega_j(\mathbf{q})}{k_BT}\}} \qquad (1.15)$$

where ϕ is the potential energy of the crystal. The free energy at constant volume, *F* (the *Helmholtz* free energy), is obtained from:

$$F = -k_B T \ln Z = \phi(V) + \int \{\frac{1}{2}\hbar\omega + k_B T \ln[1 - \exp(\frac{-\hbar\omega}{k_B T})]\} g(\omega) d\omega \qquad (1.16)$$

and,

$$S = -\frac{dF}{dT} = k_B \int \{-\ln[1 - \exp(\frac{-\hbar\omega}{k_B T})] + \frac{(\frac{\hbar\omega}{k_B T})}{[\exp(\frac{\hbar\omega}{k_B T}) - 1]}\} g(\omega) d\omega \qquad (1.17)$$

The energy, E of the crystal with volume V is

$$E = F - T\frac{dF}{dT} = \phi(V) + E_{vib} \qquad (1.18)$$

where $\phi(V)$ is the static lattice energy and E_{vib}, the vibrational energy at temperature T.

$$E_{vib} = \int \{n(\omega) + \frac{1}{2}\} \hbar\omega g(\omega) d\omega \qquad (1.19)$$

where $n(\omega)$ is the population factor given by

$$n(\omega) = \frac{1}{\exp(\hbar\omega / k_B T) - 1} \qquad (1.20)$$

The specific heat $C_v(T)$ is given by

$$C_v(T)=\frac{dE}{dT}=k_B\int\left(\frac{\hbar\omega}{k_BT}\right)^2\frac{e^{\left(\frac{\hbar\omega}{k_BT}\right)}}{\left(e^{\left(\frac{\hbar\omega}{k_BT}\right)}-1\right)^2}g(\omega)d\omega \tag{1.21}$$

The calculated phonon density of states can be used to compute the specific heat. While lattice dynamical calculations yield C_V, the specific heat at constant volume, experimental heat capacity data correspond to C_P, the specific heat at constant pressure. The difference C_P-C_V is given by,

$$C_p(T)-C_v(T)=[\alpha_v(T)]^2BVT \tag{1.22}$$

Where, α_V is the volume thermal expansion and B is the bulk modulus defined as $B=-V\frac{dP}{dV}$.

The volume thermal expansion coefficient in the quasiharmonic approximation is given by

$$\alpha_V=\frac{1}{BV}\sum_i \Gamma_i C_{Vi}(T) \tag{1.23}$$

where Γ_i is the mode Grüneisen parameter of the phonons in state i(=**q**j, which refers to the j^{th} phonon mode at wavevector **q**), which is given by

$$\Gamma_i=-\frac{\partial ln\omega_i}{\partial lnV} \tag{1.24}$$

Calculation of thermal expansion in the above fashion is applicable when explicit anharmonicity of phonons is not very significant, and the thermal expansion arises mainly from the implicit anharmonicity, i.e., the change of phonon frequencies with volume. The higher order contribution to thermal expansion arising from variation of bulk modulus with volume [9,10] is also included. These results have three main applications. Firstly, they enable us to understand the observed thermodynamic properties of the solids, facilitating the development of models to explain the quantitative details of experimental observations. Secondly, the results can be used as a predictive tool for calculating the thermodynamic properties of materials within extreme environments that cannot be reproduced in the laboratory. Thirdly, we can use these results to understand crystal stability and phase transitions.. The procedure is found satisfactory in thermal expansion calculations of Li_2O, UO_2, $LiFePO_4$, $LiMnPO_4$, $Y_3Al_5O_{12}$ etc.

1.3 COMPUTATIONAL TECHNIQUES

Lattice dynamics can be studied by a variety of methods. One approach involves fitting of empirical values of force-constants between various pairs of atoms to available experimental data. This approach is ideally suited only for simple solids, where the effective interactions between atoms are of short range, which are negligible beyond the first, second or third neighbors. Such an approach becomes cumbersome for large compounds with several atoms. As we need to calculate the anharmonic properties, thermal expansion, equation of state etc., an approach based on force constants would not be useful. The most significant part involved in lattice dynamical calculations is the setting up of the “dynamical matrix” which depends on the derivatives of the crystal potential (force-constants). An uniform prescription for calculating the crystal potential and its derivatives for various crystals would be the ideal scenario. The other approach involves using either a quantum-mechanical *ab-initio* approach [11,12] or an atomistic approach involving semiempirical interatomic potentials. Ab-initio density-functional calculations are now used frequently. Because of the structural complexity of compounds studied for the thesis work, involving a large number of atoms in the unit cell, an atomistic approach involving interatomic potentials is still very useful for studying high pressure–high temperature properties. In this thesis, atomistic approach has been used to study the vibrational properties of the compounds studied. The form of potentials used [13] for the calculations are:

$$V(r)=\{\frac{e^2}{4\pi\varepsilon_o}\}\{\frac{Z(k)Z(k')}{r}\}+a\exp\{\frac{-br}{R(k)+R(k')}\}-\frac{C}{r^6} \qquad (1.25)$$

where r is the separation between the atoms of a type k and k', Z(k) and R(k) are empirical charge and radius parameter of the atom type k, $1/(4\pi\ \varepsilon_{o)}$ = 9 x 10^9 Nm^2 /$Coul^2$, a=1822 eV, b=12.364. The last term in eq.(1.25) is applied only between certain atoms. The polarisibility of certain atoms has been introduced in the framework of the shell model.

The above potential function is used for the lattice dynamical calculations of Li_2O, UO_2, $LiFePO_4$, $LiMnPO_4$ (Chapter 2), garnets (Chapter 3), tungstates and vanadates (Chapter 4).

As a further improvement, a covalent potential (Morse potential)[3,13] is also included between certain atoms.

$$V(r)=-D\exp[-n(r-r_o)^2/(2r)] \qquad (1.26)$$

where, n, D and r_o are the empirical parameters of the potential. This potential has been used to characterize WO_4 bonds in tungstates, VO_4 bonds in vanadates and PO_4 bonds in olivines.

The parameters of the potential are determined using the conditions of the structural and dynamic equilibrium of the crystal. This procedure [14] has been very successful in the case of several compounds as discussed later in various Chapters of this thesis. Structural constraints used are that at T=0 the free energy is minimized with respect to the lattice parameters and the atomic positions of the crystal at zero pressure, and the structure is close to that determined by the diffraction experiments. The dynamic equilibrium requires that the calculated phonon frequencies have real values for all the wave vectors in the Brillouin zone. The parameters of potentials should also reproduce various other available experimental data, namely, elastic constants, optical phonon frequencies or the range of phonon spectrum, *etc.* At high pressures, the crystal structures are obtained by minimization of the free energy with respect to the lattice parameters and the atomic positions. The equilibrium structure thus obtained is used in lattice-dynamics calculations.

The aim of this work is the development of an interatomic potential which gives good description of the experimental data with the minimum number of adjustable parameters. These models have been fruitfully used to determine vibrational excitations and properties in the solids, such as: (i) the frequency of phonons as a function of the wave vector (i.e. the phonon dispersion relation), (ii) the pattern of displacement of atoms during various modes (polarization vector of the phonons), (iii) the frequency distribution of phonons, (iv) the thermodynamic properties of the solid such as the equation of state, specific heat, free energies, *etc.* and (vi) the variation of phonon frequencies due to pressure, temperature, etc.

The software DISPR [15] has been used to carry out these calculations.

1.4 THEORY OF INELASTIC NEUTRON SCATTERING

Wave-like behavior of particles beam can be used to study microscopic behavior of matter. Thermal neutrons have energies ~ up to 100 meV which are similar to phonon energies. The zero electrostatic charge on neutrons ensures that neurons do not interact with electrons but with the nucleus. The spin of the neutrons can be utilized to study magnetic behavior of the matter. Hence, neutrons can exchange part of their energy or momentum with an excitation in the system. They may lose part of their energy in creating an excitation in the system or may gain energy by annihilation. Thus, the nature of the excitation can be probed by measuring the energy and momentum of the neutrons both before and after the scattering event from a system. Equation (1.3) gives the energy and momentum conservation of neutrons before and after interaction with a sample.

$$\mathrm{E_i} - \mathrm{E_f} = \hbar\omega(\mathbf{q}, \mathrm{j}) \tag{1.27}$$

$$\hbar(\mathbf{k}_\mathrm{i} - \mathbf{k}_\mathrm{f}) = \hbar\mathbf{Q} = \hbar(\mathbf{G} \pm \mathbf{q}) \tag{1.28}$$

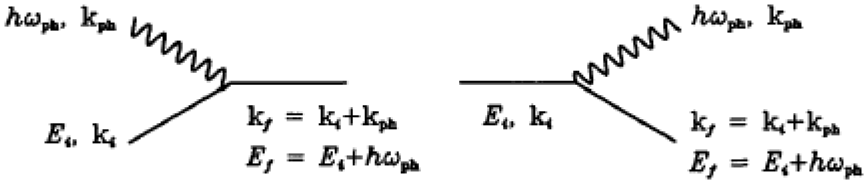

Fig. 1.1: *Scattering of neutron by one phonon, showing scattering involving absorption (left) and creation (right) of a phonon [16].*

Where, k_i, k_f are incident and the scattered neutron wave vectors and **Q** is the wave vector transfer (scattering vector) associated with the scattering process. **q** is the wave vector of the excitation with energy $\hbar\omega$ (=E), **G** is a reciprocal lattice vector, E_i, E_f are the incident and scattered neutron energies and $\hbar\omega$ is the energy transfer to the system in the scattering process. The +(-) sign indicates that the excitation is absorbed(created) in the scattering process. Hence, the experimental technique of neutron scattering to determine the nature of excitations in the system involves study of the inelastic spectrum of scattered neutrons. In fact these properties make neutrons the unique probe to study phonons in the entire Brillouin zone, unlike Raman and infrared methods which probe phonons only near the zone centre.

In the scattering process, the inelastic scattering cross-section is directly proportional to the dynamical structure factor S(**Q**, ω) (characteristic of the system), which is the double Fourier transform of the space-time correlation function of the constituents of the system including the phonon. Peaks in S(**Q**,ω) correspond to these elementary excitations [17,18]. The measurements on single crystals give information about the **q** dependence of phonon (phonon dispersion relation), while polycrystalline samples provide frequency distribution of the phonons (phonon density of states g(ω)).

1.4.1 Inelastic neutron Scattering from single crystals: Phonon Dispersion Relations

The neutron scattering structure factor [17,18] due to a one-phonon inelastic process is given by

$$S^{(1)}_{coh}(\mathbf{Q},\omega) = A'\sum_{\mathbf{q}j}\frac{\hbar}{2\omega(\mathbf{q}j)}\{n(\omega)+\frac{1}{2}\pm\frac{1}{2}\}\left|F^{(1)}_{j}(\mathbf{Q})\right|^{2}\delta(\mathbf{Q}-\mathbf{G}\pm\mathbf{q})\delta(\omega\mp\omega(\mathbf{q}j))$$

(1.29)

where,

$$F^{(1)}_{j}(\mathbf{Q}) = \sum_{k} b^{coh}_{k}\frac{\mathbf{Q}.\xi(\mathbf{q}j,k)}{\sqrt{m_k}}\exp\{-W_k(\mathbf{Q}))\exp(i\mathbf{G}.\mathbf{r}(k)) \qquad (1.30)$$

where A' is the normalization constant and b_k, m_k and **r**(k), neutron scattering length, mass and the coordinate of the k^th^ atom, respectively. ξ is eigen vector of excitation, $F^{(1)}_{j}(\mathbf{Q})$ is one-phonon structure factor, exp(-W_k(**Q**)) is the Debye-Waller factor. $\hbar\mathbf{Q}$ and $\hbar\omega$ are the momentum and energy transfer on scattering of the neutron, respectively, while n(ω) is the phonon- population factor given by eq. (1.20).

From the expression for one-phonon coherent inelastic neutron scattering, we realize that neutron groups would be observed whenever the energy and momentum conservation are simultaneously satisfied and the group would occur corresponding to a certain ω and q. Hence neutron spectrometers are designed to measure E_i, E_f, φ and ψ- the incident neutron energy, scattered neutron energy, the scattering angle and an angle which defined the orientation of the single crystal sample so that ω and q corresponding to the centre of scattering neutron group can be determined. The upper and lower signs (eq. 1.29) in ± or ∓ correspond to loss and gain of the energy of the neutrons, respectively. The two delta functions in eq. (1.29) stand for the conservation of momentum and energy. This is the procedure for measurement of the phonon dispersion curves in a system. Longitudinal mode (**q**//ξ), **G**//**q** is the necessary condition, for transverse modes, $\mathbf{q}\perp\xi$, one requires $\mathbf{G}\perp\mathbf{q}$.

In case of simple structures, the eigen vectors may be determined entirely from the symmetry of the space group. Thus the structure factors $F_j(\mathbf{Q})$ may be entirely determined from the crystal structure. In case of complex structures, the space-group symmetry only classifies the phonons into a number of irreducible representations. The number of phonons associated with each representation is same as that of number of symmetry vectors. The eigen vectors could be any linear combinations of the symmetry vectors associated with the irreducible representation. With the help of the interatomic model, eigen vectors of the individual modes can be obtained, which can be used to compute the individual structure factors. For the final comparison of experimentally determined dispersion curves with model predictions, it is crucial to know the correspondence of modes. As the scattered intensity is related to $\mathbf{Q}.\xi(\mathbf{q}j,k)$, modes belonging to some representations become invisible for particular directions of **Q** and eventually for particular Brillouin zones. This aids phonon mode identification considerably. But, often branches simultaneously visible are so close to each other in frequency, that they require careful analysis, repeated measurements at many wave-vectors in the $(\mathbf{Q},\omega)$ space. Thus, favourable large neutron-scattering cross-section regions may be identified in the (Q,ω) space in order to plan the experiments. These techniques have been used by the author to study phonon dispersion relation in $SrWO_4$ (Chapter 3).

1.4.2 Inelastic neutron scattering from powder samples: Phonon density of states

In measuring phonon dispersion relation using single crystal, **Q** has a definite orientation with respect to the reciprocal space. In the case of scattering from a powder sample, different grains with different orientations occur with equal probability. Thus an average over all available orientations is akin to averaging over all the values of Q. Hence in the limit of large **Q**, correlations between atomic motions become small and S(**Q**,ω) becomes independent of **Q** (except for some smoothly varying **Q** dependent factors), one gets S(ω), the density of excitations at the frequency ω, weighted with the neutron scattering lengths. But obtaining dispersion relation over the entire Brillouin zone is not possible, so coherent scattering data from the powder sample is usually analyzed in the incoherent approximation.

$$S_{inc}^{(1)}(Q,\omega) = \sum_k \frac{b_k^2}{< b^2 >} e^{-2W_k(Q)} \frac{Q^2}{2m_k} \frac{g_k(\omega)}{\hbar\omega} (n(\omega) + \frac{1}{2} \pm \frac{1}{2}) \tag{1.31}$$

where, the partial density of states $g_k(\omega)$ is given by

$$g_k(\omega) = \int \sum_j |\xi(\mathbf{q}j,k)|^2 \delta(\omega - \omega_j(\mathbf{q})) d\mathbf{q} \tag{1.32}$$

Thus, the scattered neutrons provide the information on the density of one-phonon states weighted by the scattering lengths and the population factor. The observed neutron-weighted phonon density of states is a sum of the partial components of the density of states due to the various atoms, weighted by their scattering length squares.

$$g^n(\omega) = B' \sum_k \{\frac{4\pi b_k^2}{m_k}\} g_k(\omega) \tag{1.33}$$

where B' is a normalization constant. Typical weighting factors $\frac{4\pi b_k^2}{m_k}$ for the various atoms in the units of barns/amu are: Al: 0.055; Fe: 0.201; Ca: 0.075; Li 0.196; Mn 0.107 and O: 0.265 to name a few.

An inelastic spectrum from a powder sample contains contribution from multiphonon scattering. Usually, for a broad one-phonon spectrum, multiphonon contributed a continuous spectrum, thereby increasing the background. The scattering function in the harmonic expression is,

$$S(Q,\omega) = S^{(0)} + S^{(1)} + S^{(n)} \qquad (1.34)$$

Each term corresponds to scattering processes involving m phonons, and the scattering function has only a weak structure in the frequency domain so that the higher order terms (>1) usually contributes only to the background scattering. The multiphonon contribution to the total scattering is usually estimated in the incoherent approximation using Sjolander's formalism [19] using the lattice dynamical model in which the total contribution is treated as a sum of the partial components of the density of states from various species of atoms. The experimental one-phonon spectra is obtained by subtracting the calculated multiphonon contribution from the experimental data.

1.5 EXPERIMENTAL TECHNIQUES FOR INELASTIC NEUTRON SCATTERING

Numerous techniques [17,18,20] have been developed to determine the change in energy and momentum of the scattered neutrons. But in this work, only the measurements using the triple-axis spectrometer and neutron time-of-flight technique are described.

1.5.1 Triple-Axis Spectrometer

Triple-Axis Spectrometer (TAS) is the most versatile and useful instrument in the field of inelastic neutron scattering. One can probe almost any coordinates in energy and momentum space in an orderly fashion. The 3-axis correspond to the axis of rotation of the monchromator, the sample and the analyzer. Monochromator defines the momentum and magnitude of incident neutron beam. Analyzer followed by a neutron detector, analyses the scattered beam in a similar manner.

Each measured intensity corresponds to an arbitrary point in the (Q, ω) space. There are two modes of measurements on the TAS. The first one is the constant Q scan, in which momentum transfer is held fixed while scattered intensity is measured as a function of energy transfer. The second method is the constant E scan, where both k_i and k_f are held fixed, so that the k_f dependence of the integrated intensity is a constant and the measured intensity should be proportional to S(Q, ω).

The resolution of the spectrometer can be changed by replacing the crystals and collimators. Fig. 1.1 shows the schematic diagram of the triple-axis spectrometer at Trombay, India [21]. The simplest method of analyzing the spectrum is by a $(\theta_A - 2\theta_A)$ scan of analyzer and detector combination, in which one may observe a neutron group at some $2\theta_A$.

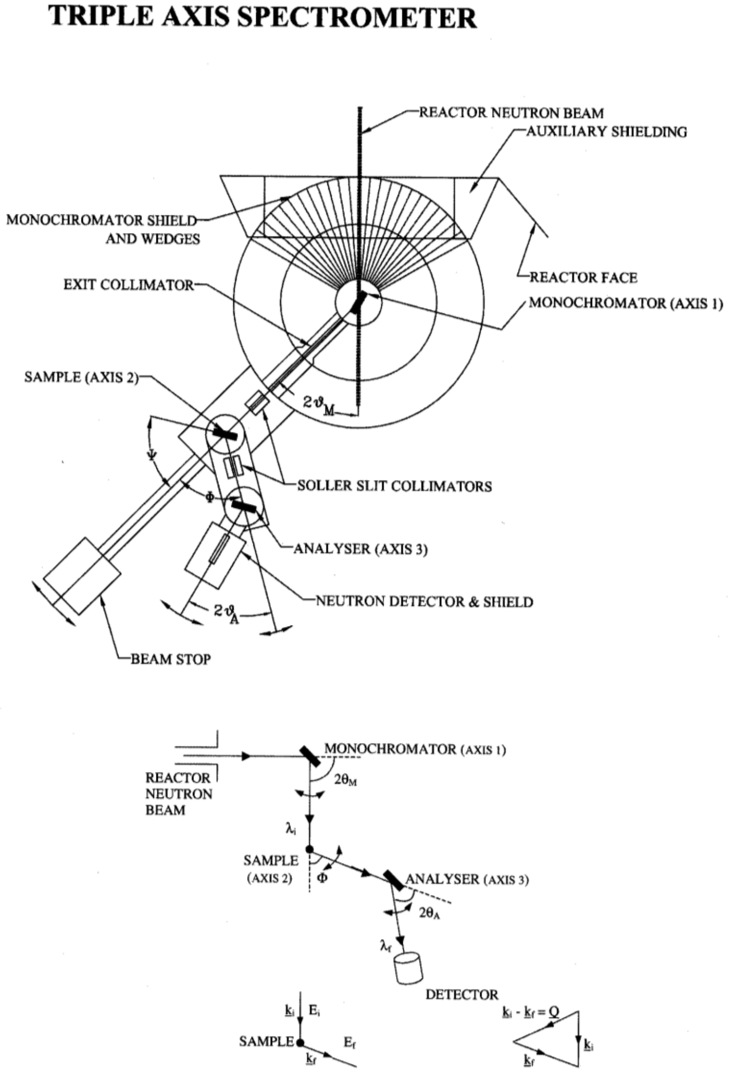

Fig. 1.2(Upper) *Layout and* ***(Lower)*** *schematic diagram of the triple-axis spectrometer at the Dhruva reactor, Trombay, India (after Ref. [2]).*

The monochromator used at TAS, Dhruva reactor, is a copper (111) monochromator and the analyzer is a pyrolytic graphite (0002) crystal. A pyrolytic graphite filter is used to reduce the contribution from the second order reflection. In another configuration, a Be-filter is used as analyzer which transmits all neutrons below 3.5 meV. The spectrometer covers scattering angles ranging from 10° to 100°. The intensity of the scattered neutrons is measured by a BF_3 gas counter. Measurements are made in the energy loss mode, in the constant Q, fixed E_f configuration. The elastic energy resolution is about 15% of the incident neutron energy. The resolution of the spectrometer can be changed by replacing the crystals and collimators.

In this thesis, phonon dispersion relation has been measured in single crystal of $SrWO_4$. Low energy branches have been measured along (001) and (100) directions using TAS at Dhruva.

1.5.2 Time-of-flight technique

Time of Flight (TOF) technique is based on the measurement of the time taken by a polychromatic neutron beam to travel from the source to the detector. An interaction with the sample results in either gain or loss of energy of the neutrons, as a result their velocities change. These changes the arrival time at the detector counter. While TAS deals with point wise scan, time-of-flight spectrometer detects a large ($\mathbf{Q}$,ω) space volume in a single run. This is done by the simultaneous use of several detectors equipped with the respective TOF electronics. The change in energy and the scattering vector $\mathbf{Q}$is obtained by measuring the flight time and the scattering angle of the neutrons from a beam pulsing device (chopper) to the detectors. The energy of the neutrons is fixed before or after the scattering process.

Phonon density of states in $LiMPO_4$ compounds (M = Fe, Mn) and AWO_4 (A = Ba, Sr, Pb and Ca) have been measured using IN4C TOF spectrometer at ILL, Grenoble, France. Details of the experiments are given in chapters 2 and 4 respectively

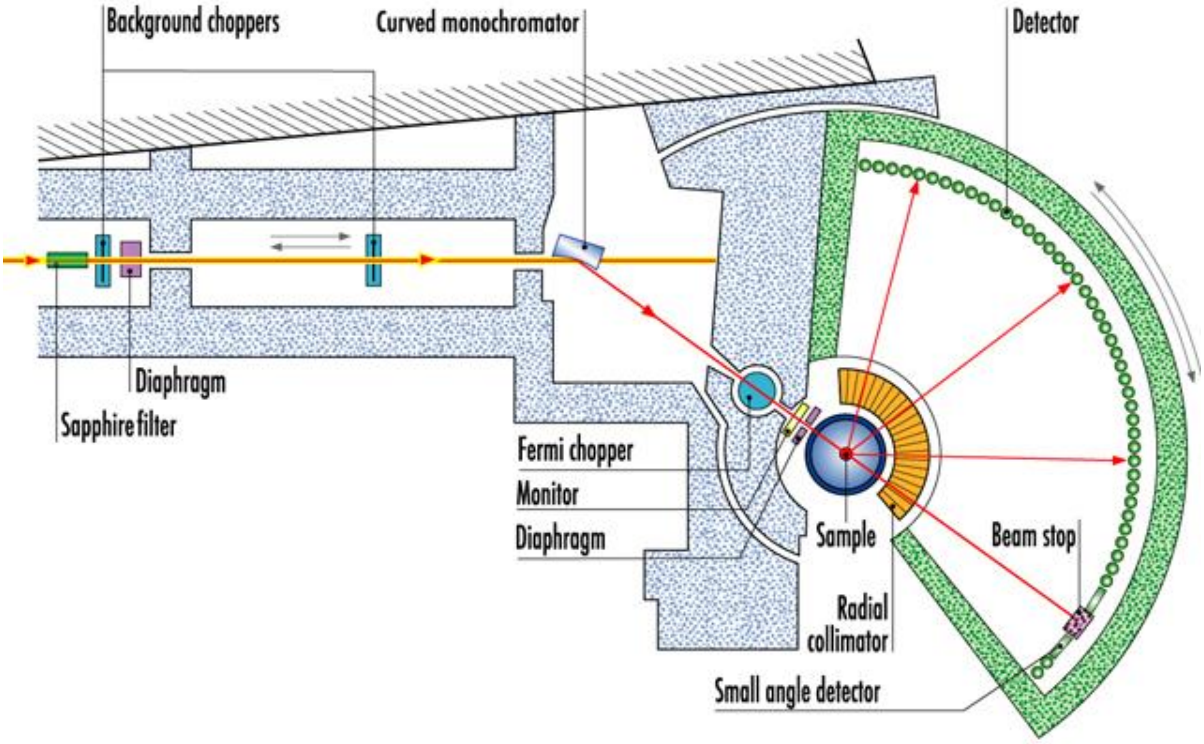

Fig. 1.3. *Time of Flight Spectrometer IN4C at Institut Laue Langevin, Grenoble, France (Courtesy: www.ill.fr)*

1.6 MOLECULAR DYNAMICS SIMULATIONS

Molecular Dynamics Simulation (MDS) is a computer simulation method used to yield information of both static and dynamical properties of a system. It is a technique in which trajectories of a system of interacting particles are computed numerically by solving their equations of motion [22-24]. The centre to this approach is to calculate the forces on the particles. The force may be obtained either from an interatomic potential, from force constants or from quantum mechanical first principles method. Hence it can be classical MDS or ab-initio MDS. This thesis presents calculations using classical approach.

Molecular dynamics simulations provide a method to study crystals at high temperature, taking into account the anharmonic interactions. Simulations involve characteristic parameters of temperature (T), volume (V), total number of particles (N), external stress (S) etc. Atomic positions and velocities at any instant of time give these parameters. These quantities in turn may be controlled by suitably constraining the atomic trajectories. Common simulations employed usually have (NVT), (NPT), (NVE) fixed. The technique has been used to study dynamical properties, i.e., to evaluate equilibrium time-correlations functions of the system.

In these computer experiments, we are interested in the motion of the atomic units comprising the lattice, in other words, the time or frequency dependence of atomic positions or correlation. Correlation functions are related to different properties. Correlation, between quantities A and B is defined as,

$$C(t) = \lim_{T\to\infty} \int_0^T A(\tau)B(t+\tau)\,d\tau \tag{1.35}$$

Where B(t +τ) is a physical quantity B at a time t + τ and A(τ) the value of a physical quantity A at time τ. The correlations can be self correlations, i.e, <A(0)A(t)>, called the auto-correlation function and cross-correlation <A(0)B(t)> respectively. Direct transport coefficients like viscosity, thermal conductivity etc., are related to autocorrelation functions where properties like diffusion are related to cross-correlations like thermal diffusion.

In our case, the main objective is to study phonons, the appropriate quantity of interest is S(**Q**,ω). This is related to time-correlation function F(**Q**,t)-the intermediate scattering function of the density operator $\rho_{\mathbf{Q}}(t)$ through the relation,

$$S(\overrightarrow{Q},\omega) = \frac{1}{2\pi}\int_{-\infty}^{\infty} e^{i\omega t}\, F(\vec{Q},t)\,dt \tag{1.36}$$

and,

$$F(\vec{Q},t) = \frac{1}{N} < \rho_{\vec{Q}}(t)\rho_{\overline{-Q}}(0) > \tag{1.37}$$

For an atomic system, the density operator is given by,

$$\rho_{\vec{Q}}(t) = \sum_{i=1}^{N} b_i\, e^{i\vec{Q}.\vec{r}_i(t)} \tag{1.38}$$

where, $r_i(t)$ being the instantaneous position of the ith atom at time t and b_i its scattering amplitude, then

$$S(\vec{Q},\omega) = \lim_{\tau\to\infty}\frac{1}{N\tau}\left|\rho_Q(\omega)\right|^2 \tag{1.39}$$

The above equation is used for computation of $S(\vec{Q},\omega)$. This scattering function has contributions from one-phonon, two-phonon and other higher order contributions along with interference terms. One can get at the one phonon contribution alone by making an expansion of the $e^{i(\mathbf{Q}.\mathbf{r}_i(t))}$ in terms of the powers of small displacements of the atom from its equilibrium consideration of the lowest order term only. Then, the one phonon approximation of S(**Q**,ω) is,

$$S_1(\vec{Q},\omega) = \frac{e^{-2w}}{N} \lim_{\tau\to\infty} \frac{1}{\tau} \left|\overrightarrow{\rho_{\vec{Q}}(t)}\right|^2 \tag{1.40}$$

The velocity auto-correlation function $< v(0)v(t) >$ is related to the frequency distribution of the system through the relation,

$$g(\omega) \propto \int_{-\infty}^{\infty} \frac{< v(0)v(t) >}{< v >^2} e^{-i\omega t} dt \tag{1.41}$$

The pair distribution function measures the probability of finding a pair of atoms a distance r apart, relative to the probability expected for a completely random distribution at the same density.

$$g(r) = \frac{V}{N^2} < \sum_i \sum_{j\neq i} \delta\left(\vec{r} - \overrightarrow{r_{ij}}\right) > \tag{1.42}$$

In practice, the delta function is replaced by a function which is non-zero at small range of separations, and a histogram is compiled of all separations falling within such range. Transport coefficients are defined in terms of the response of a system to a perturbation. Diffusion coefficient related the particle flux to a concentration gradient. In this work, transport coefficient have been calculated from equilibrium correlation functions, by observing Einstein relations,

$$D = \frac{1}{3}\int_0^{\infty} < v(t).v(0) > dt \tag{1.43}$$

and,

$$2tD = \frac{1}{3} < |\vec{r}(t) - \vec{r}(0)|^2 > \qquad (1.44)$$

The model system considered in the simulation is a macro cell consisting of N crystallographic unit cells. The unit cells are arranged usually so as to yield macro cell with almost identical dimensions along the three crystallographic directions. The state of each atom is determined by three coordinates of position and three components of velocities of the atom at any given instant of time. The collection of these coordinates and velocities gives a point in a phase-space. The system is initiated into a non-equilibrium state by either displacing the atoms by a certain but small amounts from their equilibrium positions or by giving certain random initial velocities to the atoms keeping the net momentum on the crystal to be still zero. Temperature is implicitly determined by the amount of total energy given to the system in the form of initial momentum or the positional data to the individual atoms. The position and velocities of the atom change from instant to instant as a result of the many body interactions in the system, subjected to certain interatomic potential. Equations of motion are solved to determine the state of the system as a function of time. Periodic boundary conditions help in the overcoming of the surface effects. The time step is selected such that it is nearly equal to $(1/10)^{th}$ $2\pi/\omega_{max}$. Integration of the phase space information carried out over a number of time steps chosen suitably gives the static and dynamic correlation functions and their Fourier transform. Thus, it can be seen that MD simulation can be used to provide useful information on:

i) Conventional lattice dynamical results like phonon frequencies, frequency distribution etc.

ii) Phase transitions

iii) Superionic conductivity.

A MDS calculation performed in conjunction with experimental and other theoretical work provides useful insights in to the system studied. It helps in envisaging the changes occurring in a system under extreme conditions which may or may not be possible in a real time experiment. The calculations presented in this thesis have been carried out using MOLDY [Chaplot, unpublished].

1.7 Motivation

This thesis work is a consolidated work on technologically important oxides. These oxides find several uses in industry. A basic study on their vibrational, thermodynamic and high pressure properties would result in understanding their numerous properties. This would in turn help in the improved utilization of these compounds in their various technological applications. The above discussed theoretical and experimental techniques have been employed to study the lattice dynamics, thermodynamic properties and response of the compounds to high pressure. Chapter 2 discusses the studies on superionic compounds and battery materials. Chapter 3 deals with Yttrium based garnets, which are laser host materials. Chapter 4 concerns the studies on tungstates and vanadates which are also laser host compounds. Chapter 5 briefly describes some neutron instrumentation work in which the author was involved.

REFERENCES

[1] N. W. Ashcroft and N. D. Mermin, *Solid State Physics* (Harcourt College Publishers, 1976)

[2] S. L. Chaplot, N. Choudhury, S. Ghose, M. N. Rao, R. Mittal and P. Goel, European Jouranl of Mineralogy **14**, 291 (2002).

[3] G. Venkataraman, L. Feldkamp and V. C. Sahni, *Dynamics of perfect crystals* (The MIT Press, Cambridge, 1975).

[4] M. Born and K. Huang, *Dynamical theory of crystal lattices* (Oxford University Press, London, 1954).

[5] P. Bruesch, *Phonons: Theory and experiments I* (Springer-Verlag, Berlin, Heidelberg, New York, 1982).

[6] R. Lubbers, H. F. Grunstendel, A. I. Chumakov, G. Wortmann, Science **287**, 1250 (2000).

[7] M. W. Schwoerel-Bohning, A. T. Macrander, D. A. Arms, Phys. Rev. Lett. **80**, 5572 (1998).

[8] N. Choudhury, S. L. Chaplot and K. R. Rao, Phys. Chem. Minerals **16**, 599 (1989).

[9] V. K. Jindal and J. Kalus, Phys. Stat. Sol. (b) **133**, 89 (1986).

[10] R. Bhandari and V. K. Jindal, J. Phys.: Condens. Matter **3**, 899 (1991).

[11] R. M. Wentzovitch, C. da Silva, J. R. Chelikowsky and N. Binggeli, Phys. Rev. Lett. **80**, 2149 (1998); R. M. Wentzovitch, J. L. Martin and G. D. Price, Phys. Rev. Lett. **70**, 3947 (1993).

[12] R. J. Hemley, G. Kresse and J. Hafner, Phys. Rev. Lett. **80**, 2145 (1998); L. Stixrude and R. E. Cohen, Nature **364**, 613 (1993).

[13] S. L. Chaplot, Phys. Rev. B **45**, 4885 (1992).

[14] S. L. Chaplot, Phys. Rev. B **37**, 7435 (1988).

[15] S. L. Chaplot, unpublished (1992).

[16] *Introduction to Lattice Dynamics*, M. T. Dove, Cambridge University Press (1993)

[17] P. Bruesch, *Phonons: Theory and experiments II,* (Springer-Verlag, Berlin, Heidelberg, New York, 1986).

[18] D. L. Price and K. Skold, in *Methods of experimental physics: Neutron scattering Part A*, edited by K. Skold and D. L. Price (Academic Press, Orlando, 1986), Vol. **23**; J. M. Carpenter and D. L. Price, Phys. Rev. Lett. **54**, 441 (1985).

[19] A. Sjolander, Arkiv fur Fysik **14**, 315 (1958).

[20] G. E. Bacon, *Neutron diffraction* (Oxford University Press, Oxford, 1975).

[21] S. L. Chaplot, R. Mukhopadhyay, P. R. Vijayaraghavan, A. S. Deshpande and K. R. Rao, Pramana (J. Phys.) **33** (1989) 595.

[22]*Computer Simulation of Liquids,* M. P. Allen and D. J. Tildesley, Oxford University Press (1991)

[23] *Current trends in Lattice Dy*namics, ed. K. R. Rao, Indian Physics Association, Bombay (1978)

[24] *Thermodynamic Properties of Solids,* Eds. S.L.Chaplot, R. Mittal and N. Choudhury, Wiley-VCH Verlag GmbH & KGaA (2010)

Chapter 2

Phonons, diffusion and superionic behavior in nuclear oxides and battery materials

2.1. INTRODUCTION

UO_2 and Li_2O both belong to the class of superionics, which allow macroscopic movement of ions through their structure. Rapid diffusion of a significant fraction of one of the constituent species occurs within an essentially rigid framework of other species [1]. In UO_2, it is the uranium, which forms the rigid framework while in Li_2O it is the oxygen sub lattice, which is rigid [2,3,4]. UO_2 is of technological importance owing to its use as a nuclear fuel [5,6,7,8,9]. Knowledge of the thermodynamic and transport properties of nuclear fuel at high temperatures is of great interest. Li_2O finds several technological applications ranging from miniature light -weight high power density lithium ion batteries for heart pacemakers, laptop computers, *etc*. Owing to its high melting point, low volatility and high Li atom density, Li_2O is considered a leading contender for future fusion reactors to convert energetic neutrons to usable heat and to breed tritium necessary to sustain D-T reactions [10,11,12].

Ever increasing energy demands has always promoted research for the elusive perfect battery material, thus paving way for a safer, secure, sustainable energy alternative [13-18]. Lithium transition metal phospho-olivines [19,20,21] have emerged as one of the leading contenders in this race. Since the time they were proposed by Padhi [18,20] et al, they have been actively considered as a potential and viable alternative to the conventional cathode materials like $LiCoO_2$. $LiMPO_4$ have large theoretical capacity [20,21] and a large operating voltage[16,20]. The importance is further accentuated by their stability [22,23], high safety, low cost, low toxicity and cyclability. The electrochemical [24-27] properties of these materials determine Li intercalation and deintercalation[26], vital to their functioning as useful electrode materials. They in turn are determined by their basic structural and thermodynamic properties. Despite enormous works pertaining to battery research [24-30], many aspects of their basic vibrational and other physical properties have not been copiously studied. In this chapter, results obtained on nuclear oxides and battery materials are given in sections 2.2 and 2.3 respectively.

2.2 NUCLEAR OXIDES

Microscopic modeling or simulation is necessary to understand the conduction processes at high temperatures in these crystals. The fluorite UO_2 (Li_2O is an anti-fluorite) is a face-centered cubic structure belonging to the space group O^5_h (*Fm3m*). Oxygen (Lithium) atoms are in the tetrahedral sites. These compounds show a type II superionic transition [1,10] attaining high levels of ionic conductivity following a gradual and continuous disordering process within the same phase. Several theoretical [31-40] and experimental [41-47] works have been reported on numerous fast ion conductors like Li_2O, CaF_2, BaF_2, PbF_2, $SrCl_2$, CuI [48-51] *etc*. The main impetus for these studies has been to unravel the causes behind the process of fast ion conduction. In case of Li_2O, further interest has been to study Li diffusion from the point of view of tritium generation for future fusion reactors. The significance of such studies in UO_2 need not be exaggerated, as its high temperature studies have been motivated by its use as a nuclear fuel for nuclear fission reactors. The thermophysical properties of this oxide have important implications when assessing the issues regarding safe operation of reactors. These oxides behave similarly to other superionic halides. The extensive diffusion is characterized by a large decrease in the elastic constant C_{11} and specific heat anomaly at the transition temperature, T_c [51-57]. Neutron scattering measurements [58] indicate that the anionic sub lattice in UO_2 becomes heavily disordered in the region of 2300 K. Measured elastic constants [59,60] do show a softening above 2400 K in the region where fast ion behavior is expected in UO_2, but the variation below this temperature is already very large. There is a high increase in specific heat [61,62] at high temperatures in UO_2. Li_2O shows a sudden decrease in the value of the C_{11} elastic constant at the transition temperature, T_c~1200 K (the melting point is 1705 K), but there seems no drastic change in the specific heat [63,64]. Both these compounds comply with the general belief that fluorites (anti-fluorites) in general show a diffuse transition at about 0.8 T_m (T_m = melting point, T_m of UO_2 is 3120 K). Above the transition temperature the diffusion coefficient of one of the constituent atom becomes comparable to that of liquids. Detailed study of the processes occurring in the crystal lattice at elevated temperatures is essential to understand the transitions.

The author has looked at the probable interstitial regions where lithium might reside while diffusing such a way that the local structure remains largely unperturbed. Extending further, using lattice and molecular dynamics, author has tried to determine the probable directions of diffusion of the lithium ions and the role of phonon and elastic instabilities. An analysis with potential model calculations has been carried out. The behavior of phonon modes along symmetry directions at volumes corresponding to superionic regime using potential model calculations has been done. The decrease in the elastic constants with increasing temperature has been studied. Superionic fluorites are found to exhibit rapid decrease in elastic constants particularly C_{11} and a specific heat anomaly around the transition temperature. But Li_2O does not exhibit any specific heat anomaly as observed experimentally which is in agreement with our earlier computations. Finally author has tried to figure out easy direction of movement of the Li ion which is crucial in understanding diffusion mechanism in a given system. In this work the author has tried to deduce the most probable direction of movement by studying the energy profile for Li movement along various high symmetry directions. This does not rule out lithium's diffusion in other directions, but simply indicates one of the easy directions of diffusion. The study of the high temperature behavior and their implications could play a pivotal role in understanding and improving the myriad technological applications of this immensely useful oxide.

The present study is aimed at formulating a suitable interatomic potential to explain the vibrational properties of the oxides in concurrence with the available experimental data.. The main objectives of the present study are: (i) to determine a suitable interatomic potential model to calculate the phonon spectrum, specific heat, other thermodynamic and elastic properties, which would be in good agreement with the various experimental observations; (ii) to carry out molecular dynamics simulations using the parameters obtained from the lattice dynamics calculations to elucidate diffusion behavior and the thermodynamic properties of the oxides at elevated temperatures, and

(iii) to study the possiblilty phonons in the initiation of diffusion, i.e, to understand in particular any phonon mode triggering the phenomenon of sub-lattice melting. Also, author has studied the easy direction of diffusion of the lithium atoms.

2.2.1 Theoretical Details

The calculations have been carried out in the quasiharmonic [65] approximation using the interatomic potentials consisting of Coulomb and short-range Born-Mayer type interaction terms as described equation (1.25) in chapter 1. The model parameters (charge Z and radius R) are Z_{Li} = 0.75e, R_{Li} = 0.129 nm, R_O = 0.175 nm, shell charge Y_O = -2.0 and shell constant is 6500 eV/nm^{-2} . In case of UO_2, Z_U = 2.9e, R_U = 0.21 nm, R_O = 0.175 nm, shell charge is -2 and shell constant is 11000 eV/nm^{-2}.

Group theoretical symmetry analysis was undertaken to classify the phonon modes belonging to various representations. Because of the selection rules only phonon modes belonging to certain group theoretical representations are active in typical single crystal Raman, infrared and inelastic neutron scattering measurements. These selection rules are governed by the symmetry of the system and the scattering geometry employed. The theoretical scheme for the derivation of the symmetry vectors is based on irreducible multiplier representations [66] and construction of symmetry adapted vectors, which are used for block diagonalizing the dynamical matrix [67]. These permit the assignment of the phonon modes belonging to various representations. For fluorites, group theoretical analysis provides a classification of the frequencies at zone center (**Γ**-point) and the high symmetry directions (**Δ**, **Σ** and **Λ**), into the following representations:

Γ: $2T_{1u} + T_{2g}$, where T_{1u} and T_{2g} phonon modes are triply degenerate

(00ζ): $2\Delta_1 + \Delta_2 + 3\Delta_3$

(ζζ0): $3\Sigma_1 + 2\Sigma_2 + \Sigma_3 + 3\Sigma_4$

(ζζζ): $3\Lambda_1 + 3\Lambda_3$

where, the Λ_3 and Δ_3 phonon modes are doubly degenerate. Based on the crystal symmetry, Li_2O is expected to have one infrared active mode (T_{1u}) and one Raman active optical mode (T_{2g}). The classifications of the phonon modes into different irreducible representations enable direct comparison with single crystal Raman, infrared and neutron data.

The phonon frequencies, the elastic constants, the specific heat and the equation of state at ambient conditions have been calculated. The phonon dispersion at high pressure up to 100 GPa have also been computed. The dispersion corresponding to volumes corresponding to superionic regime has also been computed in Li_2O to understand the role of phonons in the initiation of fast ion conduction. The most probable direction of movement of Li has been elucidated by studying the energy profile along various high-symmetry directions. These results have been compared with the available experimental data wherever available.

Molecular dynamics simulations have been successfully used to study the process of diffusion in these compounds, changes occurring in the lattice at microscopic level, the mechanism of diffusion by observing the snapshots of Li movement in the superionic regime. The technique has been used to look for decrease in elastic constants, C_{11} in particular, which is a characteristic feature of superionic compounds. The possibility of role of phonons as a precursor to fast ion diffusion has been studied. The easy direction of vacancy assisted lithium movement in the superionic regime has been investigated by studying the energy profile for lithium movement along different high-symmetry directions.

2.2.2 Li_2O

2.2.2.1 Results and Discussion

2.2.2.1a Phonon dispersion and density of states

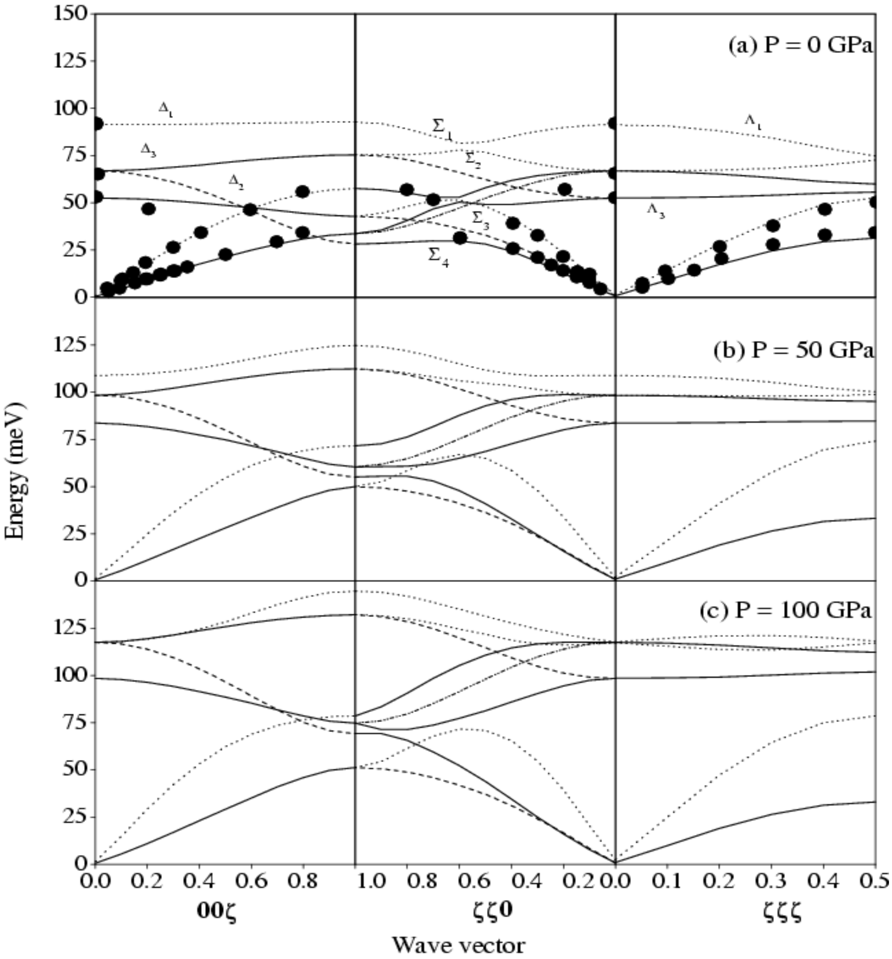

Fig.2.1. *Phonon dispersion relation in Li_2O, at (a) 0 GPa, (b) 50 GPa and (c) 100 GPa. Solid symbols are experimental results from neutron scattering [46].*

The calculated values of the lattice parameter, bulk modulus and elastic constants compare well with the experimentally obtained data as presented in Table 2.1. From the phonon dispersion relation along [110], we can obtain the value of C_{11}-C_{12} for cubic systems, which is in good agreement with its corresponding experimental value. Since C_{12} is derived indirectly using the values of C_{11} and (C_{11}-C_{12}), it appears to be overestimated, as compared to the experimental results [42]. The calculated phonon dispersion relation in lithium oxide is given in Fig. 2.1 at three different pressures. It shows that the agreement of the calculations with the single crystal neutron [46], Raman and infrared data [47] is excellent.

Table 2.1: *Comparison between calculated and experimental lattice [2] parameters and elastic constants [42] at ambient conditions. The numbers in the parenthesis are the errors in the last significant digit.*

Physical Quantity	**Experimental**	**Calculated**
Lattice parameter (nm)	0.460 (1)	0.461
Bulk Modulus	81.7(62)	103
C_{11} (GPa)	202 .0 (55)	213
C_{44} (GPa)	58.7 (8)	52
C_{12} (GPa)	21.5 (66)	56
$C_{11} - C_{12}$ (GPa)	180.5 (86)	157
Anisotropy factor ($2C_{44}/(C_{11}$-C_{12}))	0.65 (5)	0.66

With the increase in pressure, our calculations do not indicate any softening of the phonon modes. In general, all the frequencies have hardened with pressure; especially phonons in the energy interval between 50 and 75 meV at P = 50 GPa show a shift of about 25 meV towards the higher end, while the topmost branch shifts by only about 15 meV. With further increase in pressure to 100 GPa, the above frequencies harden further by 15 meV. The calculated values of the lattice parameter, bulk modulus and elastic constants of the compounds compare well with the experimentally obtained data as presented in Table 2.1. From the phonon dispersion relation along [110], we can obtain the value of C_{11}-C_{12} for cubic systems, which is in good agreement with its corresponding experimental value. Since C_{12} is derived indirectly using the values of C_{11} and (C_{11}-C_{12}), it appears to be overestimated, as compared to the experimental results [42].

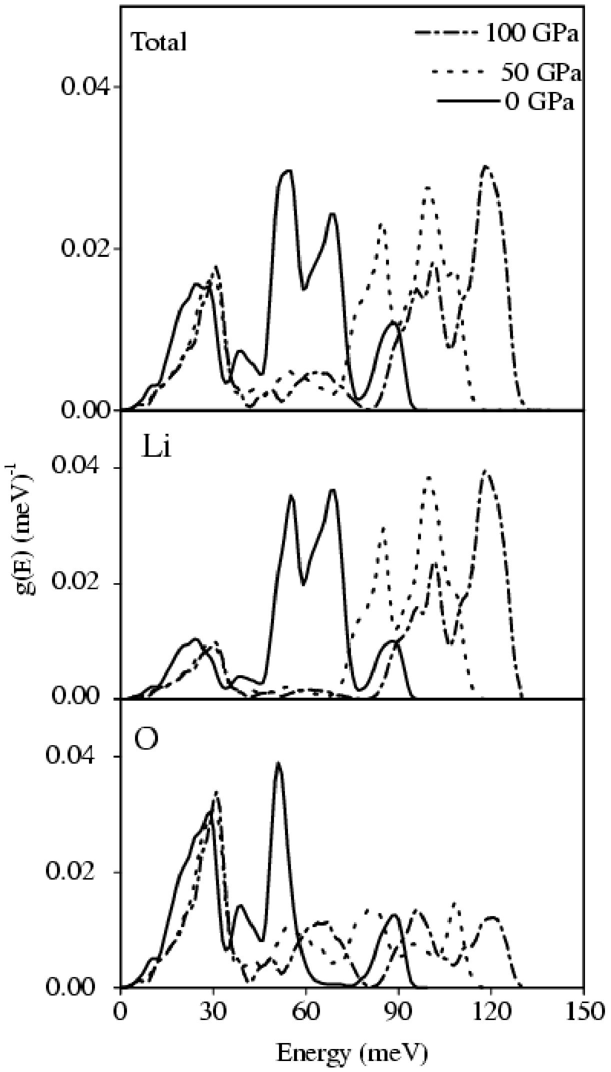

Fig. 2.2: *Phonon density of states along with partial density of states of lithium and oxygen at different pressure*

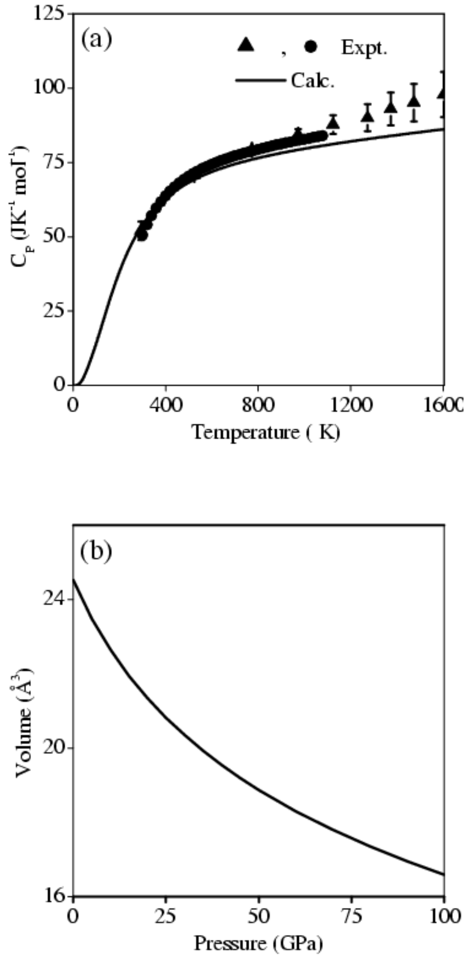

Fig. 2.3: ***(a)*** *Specific heat at constant pressure compared with experimental data [42,44] (circles and triangles).* ***(b)*** *The equation of state for* Li_2O.

These observations are further substantiated from the total density of states, and the partial densities for Li and O atoms in Fig. 2.2. The energy span at P = 0 GPa is between 0-90 meV, at P = 50 GPa, it is up to 120 meV, while at P = 100 GPa it spans up to 135 meV. As can be seen from the figure, the peak around 50 meV at P = 0 GPa has shifted to higher energy with pressure increase, while the peak around 20 meV is more or less undisturbed. From the partial densities, we can conclude that the oxygen contribution is much greater on the lower energy end, which remains unperturbed by pressure changes, suggesting its greater stability compared to lithium. At P = 0 GPa, lithium ion's contributions lie mainly in the interval 45-75 meV, likewise oxygen atom's contribution lies mainly in the interval 0 and 60 meV. There is a contribution from both atoms at 90 meV. At P = 50 GPa, lithium atoms contribute between 75-120 meV while oxygen atoms contribute up to 120 meV. At 100 GPa, lithium contributes mainly between 85-135 meV, while oxygen contributes till 135 meV. At all the three pressures, the lowest peak for both the atoms is practically indistinguishable.

The calculated specific heat, $C_P(T)$, has been compared with the available experimental data [42,44] in Fig. 2.3(a). The comparison is very good up to about 1100 K beyond which the fast ion behavior sets in and the slope of the experimental data is much greater compared to calculations.

This is expected owing to the quasi-harmonic approximation in lattice dynamics calculations. The equation of state, i.e., the variation of the volume of the primitive cell with pressure, is given in Fig. 2.3(b), however experimental data for the same is unavailable for comparison. There is a smooth decrease in volume with increase in pressure. Li_2O undergoes a first order transition to cottunite structure, according to our calculations it is not driven by dynamical instabilities [43b].

2.2.2.1b Diffusion of Lithium, snapshots of lithium movement

The diffusion coefficient of lithium ion has been compared with experimental [45] data in Fig 2.4. The experimental [45] transition temperature of the normal to fast ion phase is about 1200 K at zero pressure whereas the calculated value lies at about 1000 K, which is in good agreement. The application of a static pressure of 5 GPa increases T_c only marginally by 200 K to about 1200 K.

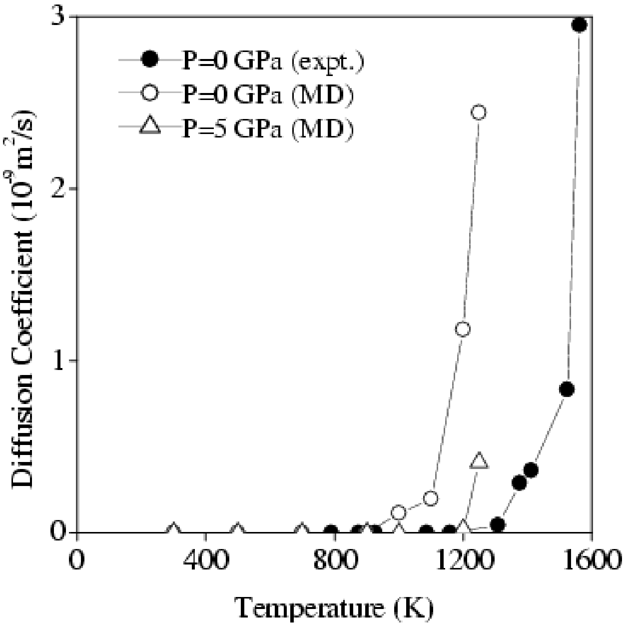

Fig. 2.4: *Diffusion coefficient of Li and its variation with temperature and pressure as obtained from molecular dynamics simulations. Solid circles are experimental [45] results at ambient pressure.*

The thermal amplitude of lithium atom is compared with experimental results [2] in Fig 2.5(a), which is in very good agreement. The change in the slope of the plot at the superionic transistion, which is seen in the experiment, is brought out clearly. The variation of the volume of the unit cell with temperature, as obtained from molecular dynamics simulations is plotted in Fig. 2.5 (b), which shows a good agreement with experiment [42]. The implicit thermal expansion calculated from quasiharmonic lattice dynamics arising from the volume dependence of phonon frequencies is also plotted, which accounts for only a part of the observed thermal expansion.

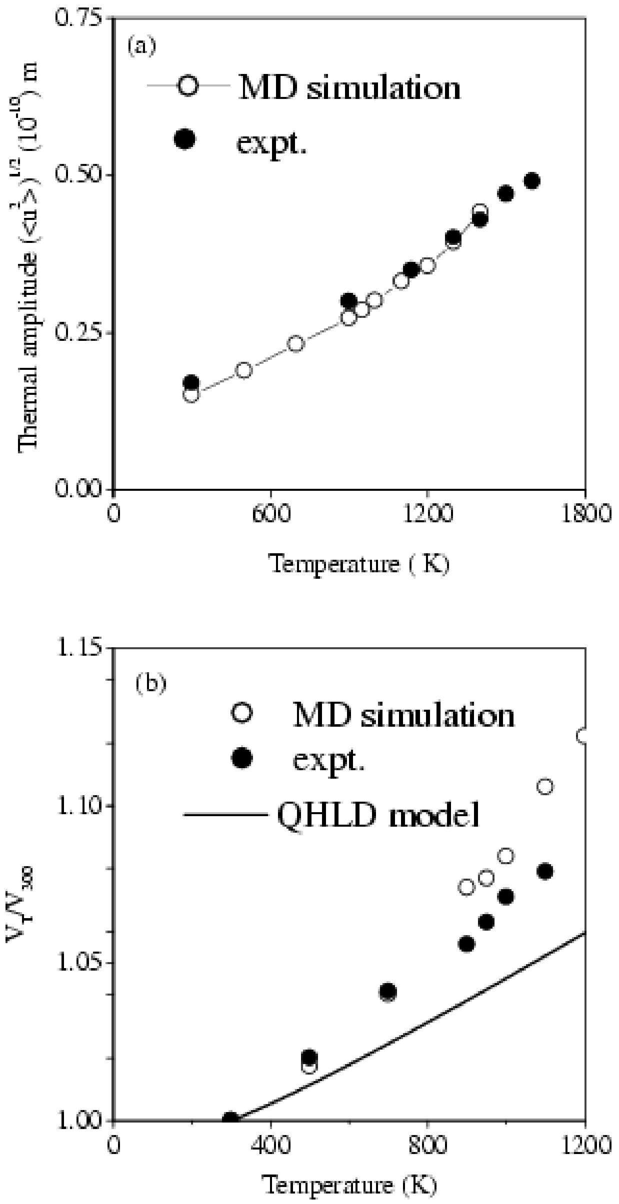

Fig. 2.5: *(a) Calculated (open circles) thermal amplitude of lithium as a function of temperature at ambient pressure in comparison with experiment [2] (solid circles). (b) Variation of lattice volume with temperature at ambient pressure with experiment [42]. Full line is derived from quasiharmonic lattice dynamics calculations.*

The disturbances in the crystal structure accompanying the superionic transition are limited to the lithium sub lattice. This conclusion is further strengthened by the pair correlation functions of Li-Li, Li-O and O-O in Fig 2.6(a). But it is also noteworthy to mention that the disturbances in the lithium sub lattice occur gradually as seen from the broadening in the pair correlation functions of Li-Li with increasing temperature. On similar lines, we can understand the angle distribution of Li-O-Li bond in Fig. 2.6 (b), which again shows no drastic changes near the fast ion transition. This reiterates the notion that the disturbances occurring in the lattice are highly localized and the local environment is only moderately disturbed.

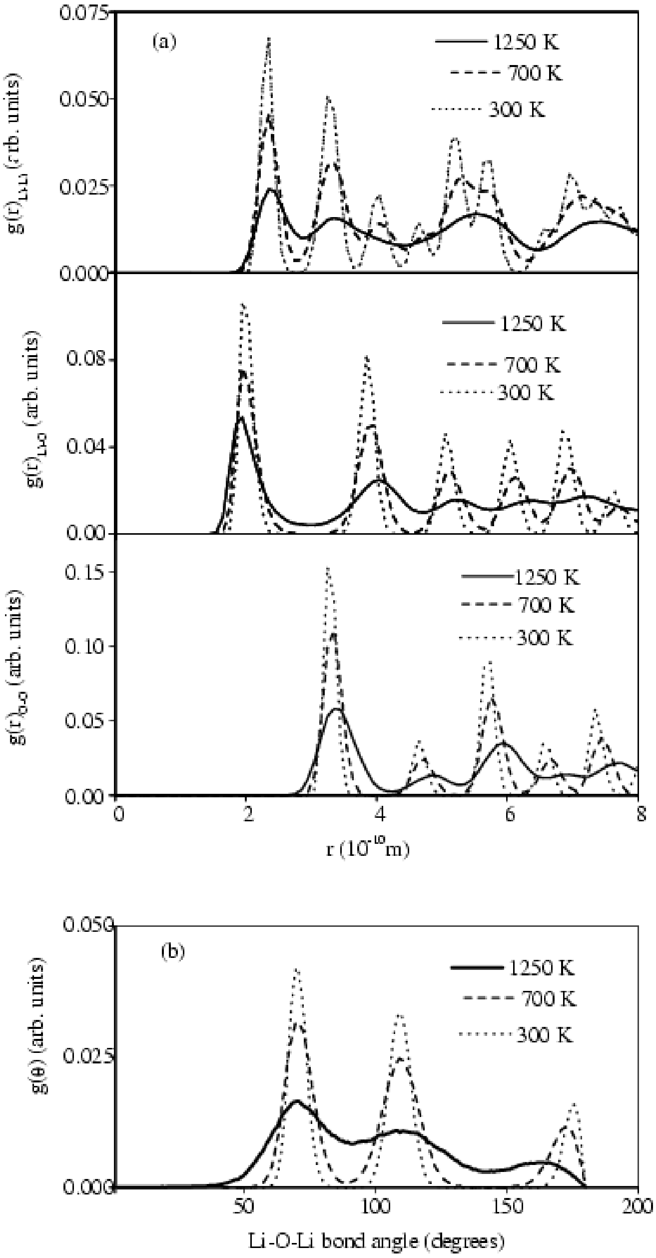

Fig. 2.6 (a) *Pair correlation functions of LI-Li, Li-O and O-O and* ***(b)*** *angle correlation function of LI-O-Li bond angle in* Li_2O *at different temperatures and ambient pressure as obtained from MD simulations.*

(a) Atom A

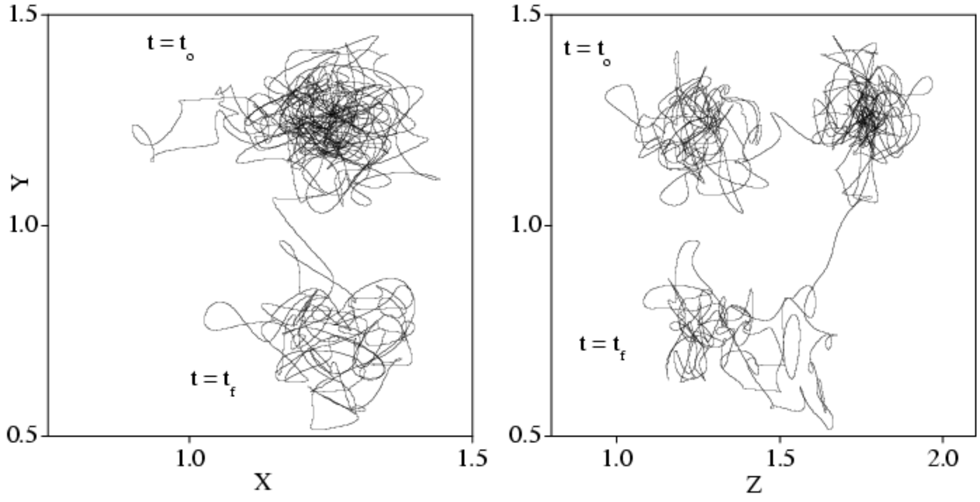

(b) Atom B

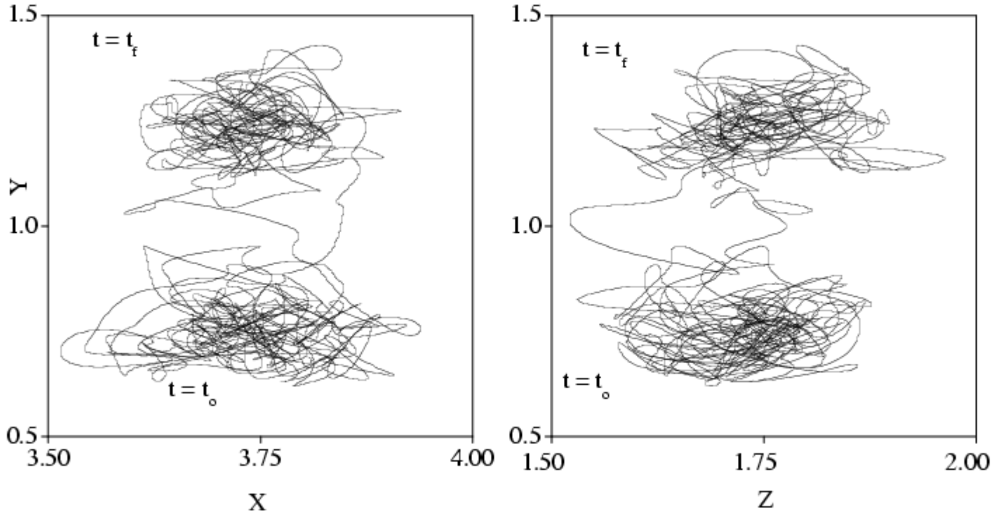

Fig. 2.7: *Snapshots of the movement of given lithium atoms **(a)** atom A and **(b)** atom B in a duration of 10 ps in the XY and YZ planes at 1250 K at ambient pressure. The values in the x-axis are actually multiples of lattice parameter at 1250 K.*

The oxygen sub lattice remains unperturbed as seen from the plots in Fig. 2.6. The position – time plots of certain Li atoms, for a time duration of 10 picoseconds at 1250 K in XY and YZ planes are given in Fig 2.7. The Li atom A at an initial position (the positions are actually multiples of the lattice parameter) of (1.25,1.25,1.25) moves to a second position (1.25,1.25,1.75) with a jump time of approximately 0.065 picoseconds, residence time being more than 3.3 picoseconds at the initial position. It then moves to the third position of (1.25,0.75,1.25). The residence time at the second position is 3.9 picoseconds. Before moving to the third position, it undergoes some transit zig- zag motion in the octahedral region surrounding the coordinate (1.25,1.65,1.5).On the other hand atom B starts at an initial coordinate of (3.75,0.75,1.75) and then moves to the second position (3.75,1.25,1.75) in the time duration for which these atoms were tracked. These results indicate that the lithium atoms jump from one tetrahedral position to another, passing the octahedral interstitial regions during transit; at any given instant the probability of an atom sitting in the octahedral position is rather small.

Similar results have been reported for CuI [39,40], where ionic density distribution shows no or very little occupation of the octahedral sites with increase in temperature. Average potential energy curves obtained for CuI [39] depicts that energy is a minimum at the tetrahedral sites and rises rapidly as the octahedral site is approached. The lithium atoms essentially move from one tetrahedral position to another randomly, yet maintaining the local order and structure to a great degree.

2.2.2.1c. Phonons in superionic regime

Having ascertained the process of fast ion difusion the author has looked at the changes occurring in the phonon dispersion in the superionic regime. The phonon dispersion using the potential model at lattice parameters corresponding to ambient (a = 4.60 Å) and superionic (a = 4.90 Å) regime are shown in Fig.2.8. As expected the phonon frequencies along all the three direction are found to soften with increase of volume. The softening is found to be small for all the modes except for the lowest transverse acoustic (TA) branch along [110] at zone boundary.

The eigen vector of TA mode has been plotted (Fig. 2.9) corresponding to the unit cell parameter of a= 4.88 Å. Lithium atoms in the alternate layers move opposite to each other along [001] while oxygen's are at rest. The easy direction for lithium movement is along [001] (as discussed below). Hence increasing the temperature could lead to migration of lithium ions from one site to another vacant site along [001] direction, which can easily be visualized from the figure.

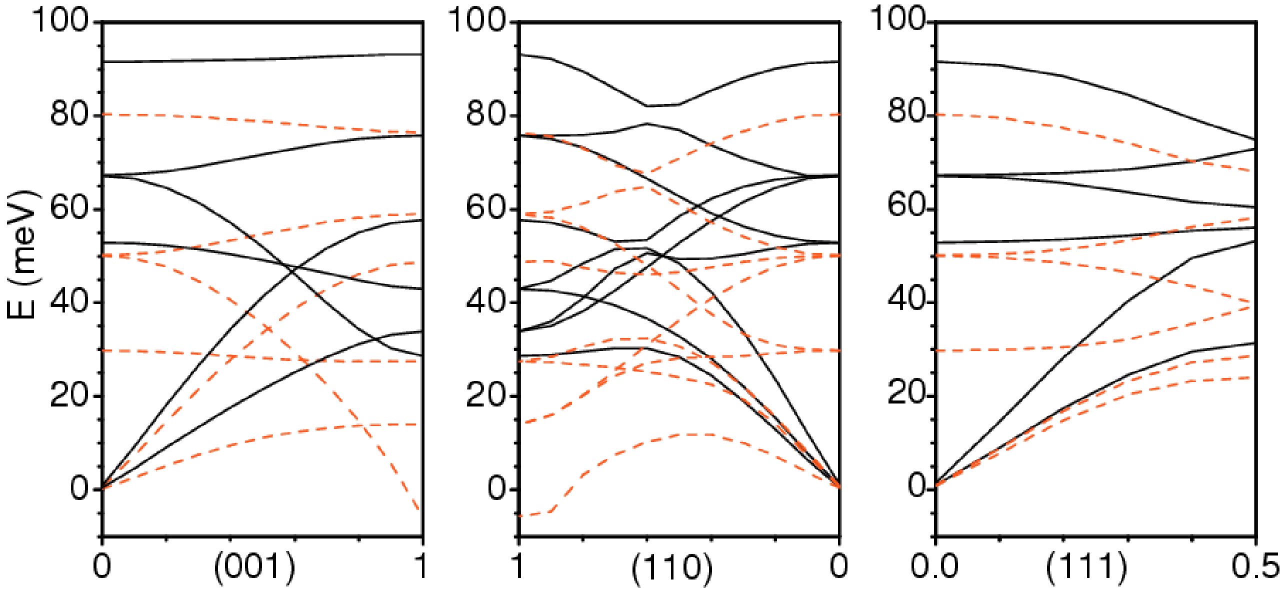

Fig. 2.8: *Phonon dispersion using quasiharmonic approximation at a = 4.6 and 4.9 Å (full black and red dashed lines). These values of the lattice parametes were obtained from MD simulations. Phonon energies shown below E = 0 have imaginary values indication unstable modes.*

Fig. 2.10 gives the change in the transverse acoustic frequency with increasing lattice parameter, using potential model calculations. The lowest TA mode along [110] at zone boundary is found to soften sharply at volume in the superionic regime. At the superionic transition, some of the lithiums might just have sufficient energy to move from their ideal positions and start diffusing. It is possible that the softening of these modes might be the precursor to the process of diffusion. Fracchia [32] et al have also reported softening of zone boundary mode along [001] in Li_2O.

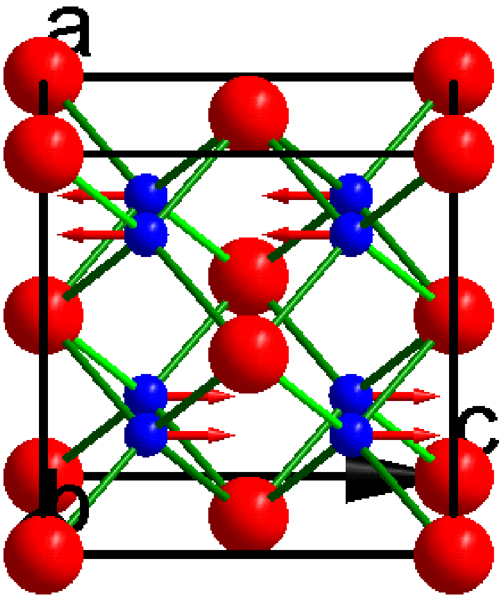

Fig. 2.9: *Motion of individual atoms for zone boundary TA mode along the [110] direction at a = 4.88 Å. The lengths of arrows are related to displacement of the atoms. The absence of an arrow on an atoms indicates that the atom is at rest.* ***b*** *is perpendicular to the plane. O= red (dark gray) spheres, Li = blue (medium gray) spheres.*

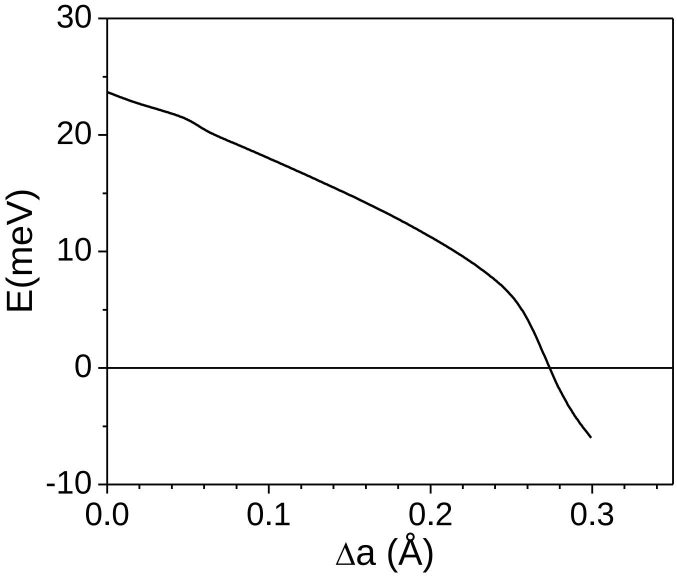

Fig. 2.10: *Softening of zone boundary TA phonon along [110]. The equilibrium a parameter is 4.6 Å.*

2.2.2.1(d). Temperature variation of elastic constants and energy profile for Li-movement

Molecular dynamics (MD) technique is used to calculate the effect of temperature on the elastic properties. It is found that increasing temperature results in significant change in the acoustic phonon frequencies which in turn brings a change in the elastic properties. The calculations are found to be in good comparison (Fig. 2.11) with the reported experimental data. C_{11} shows maximum softening which is one of the characteristic features of a superionic compound. The change in C_{12} is marginal while C_{44} remains almost constant with temperature increase. The gradual change in C_{44} and C_{12} with increasing temperature is brought out better in the molecular dynamics simulation and is in good agreement with experimental findings. With increasing temperature most of the phonon modes shift towards lower energy. The details of dependence of elastic constants on temperature could play a pivotal role in understanding the role and uses of lithium oxide as blanket material for tritium production in fusion reactors.

The movement of atoms in a material depends on the interatomic bonding, temperature, microstructure, size and type of atoms moving. Energy profile for lithium movement has been calculated by creating a vacancy and moving a lithium atom from its initial lattice site towards the vacant lattice site along a given high symmetry direction, namely [001], [110] and [111] directions in a 10×10×10 supercell, and monitoring the change in the total crystal potential. The charge neutrality of the super cell has been maintained in the complete process. This enables us to identify the easy direction for Li motion towards vacancy at different temperatures. The profiles of the energy changes are shown in fig. 2.12. The calculated energies for movement of Li atom along [001], [110] and [111] directions are 0.3(0.0), 9.4(6.3) and 2.0(1.8) eV respectively at unit cell volume corresponding to 4.60 and 4.88 Å. It can be seen that the most favorable direction for lithium movement is along [001] direction. With increase in temperature, the increased availability of defects and vacancies could lead to a simultaneous movement of several lithium ions towards their nearest vacant site. This cooperative phenomenon could lead to a macroscopic effect of diffusion which is observed in Li_2O above superionic temperature. But this does not rule out lithium's motion along a combination of other directions.

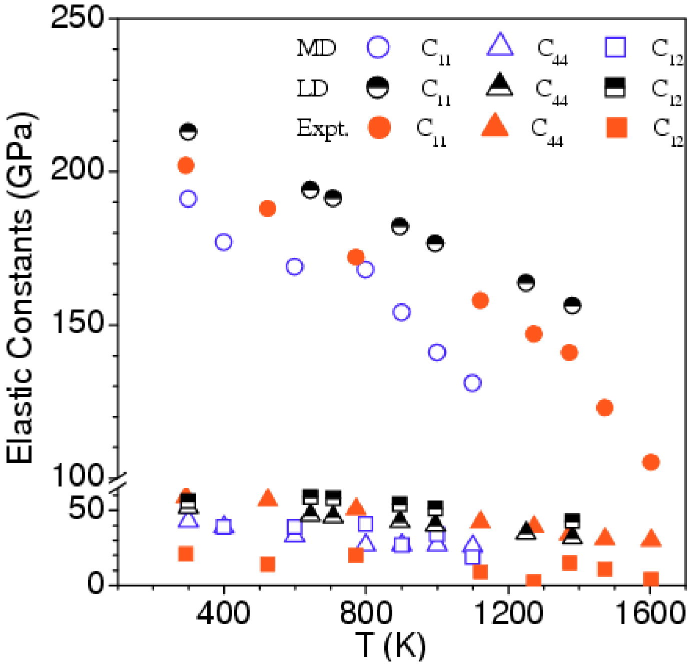

Fig. 2.11: *Softening of elastic constants with increasing temperature compared with reported experimental results [42,2]. The open, half-filled symbols correspond to the calculated values using MD and LD formalism, while solid symbols denote the reported experimental results.*

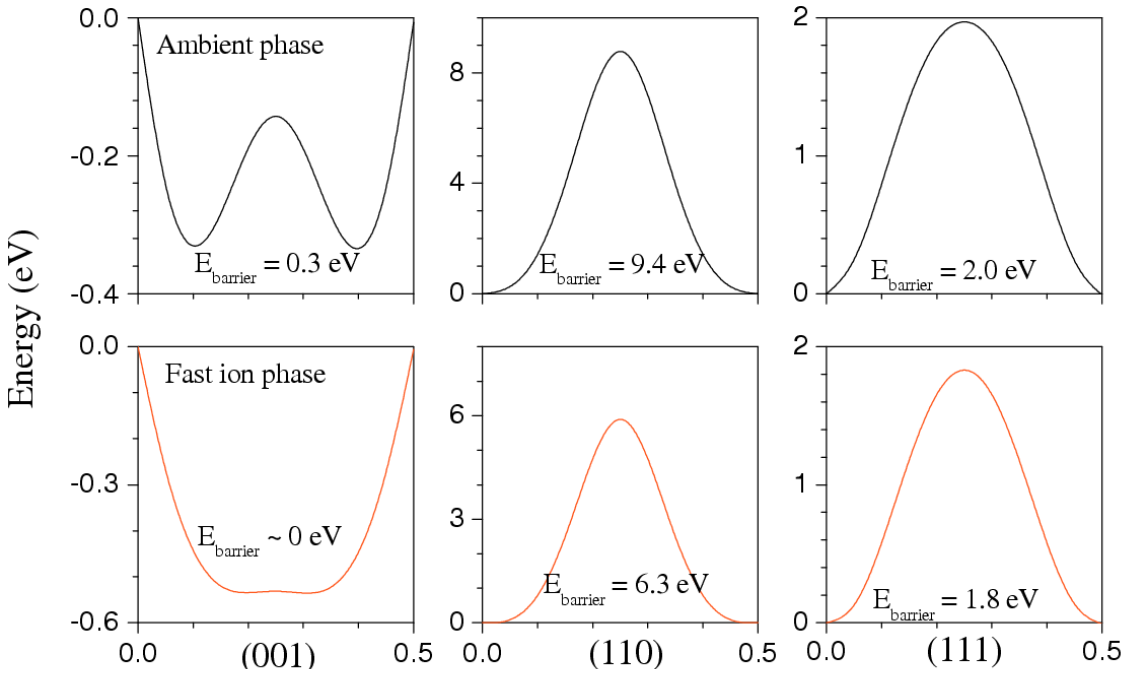

Fig. 2.12: *Energy profile for lithium ion movement along high-symmetry directions. Calculations were carried out using a 10 x 10 x 10 supercell corresponding to lattice parameter values of 4.606 and 4.88 Å.*

2.2.3 UO_2

2.2.3.1 Results and Discussions

2.2.3.1(a) Phonon spectra and thermodynamic properties of UO_2

The calculated values of the lattice parameter, bulk modulus, and elastic constants compare well with the experimentally obtained data [52,53] as given in Table 2. 2. The average Grueneisen contant, Γ_i for all the phonons in uranium oxide is 1.55 and they agree well with available experimental data [68].

The phonon dispersion relation in UO_2 at various pressures, is shown in Fig. 2.13, along the various high symmetry directions. The computed dispersion at P = 0 GPa is in excellent agreement with available inelastic neutron scattering experimental data [69]. The phonon frequencies are found to harden progressively with increasing pressure. With increase in pressure, our calculations do not indicate any softening of the phonon modes. Theoretical studies reveal a free energy crossover at 70 GPa [70].

Table 2.2: Comparison between calculated and experimental lattice [1,59] parameters and elastic constants at ambient conditions.

Physical Quantity	**Experimental**	**Calculated**
Lattice parameter (nm)	0.5470 (1)	0.546
Bulk Modulus (GPa)	207	181
C_{11} (GPa)	389(5)	387
C_{44} (GPa)	60(3)	66
C_{12} (GPa)	119(7)	77
Anisotropy factor ($2C_{44}/(C_{11}-C_{12})$)	0.426	0.444

Our calculations suggest that it is not driven by dynamic instability but arises due to lower volume of the high-pressure cottunite phase. At P = 0 GPa, the highest phonon branch is seen at about 70 meV, which shifts up to 80 meV at P = 50 and further to 80 meV at P = 100 GPa. The energy spread between the acoustic modes is greater at higher pressures. The gap between the lowest optic mode and the highest acoustic mode increases with increasing pressure at the zone boundary. The total and partial densities of UO_2 are given in Fig. 2.14. The observations of phonon dispersion picture are further substantiated by this figure.

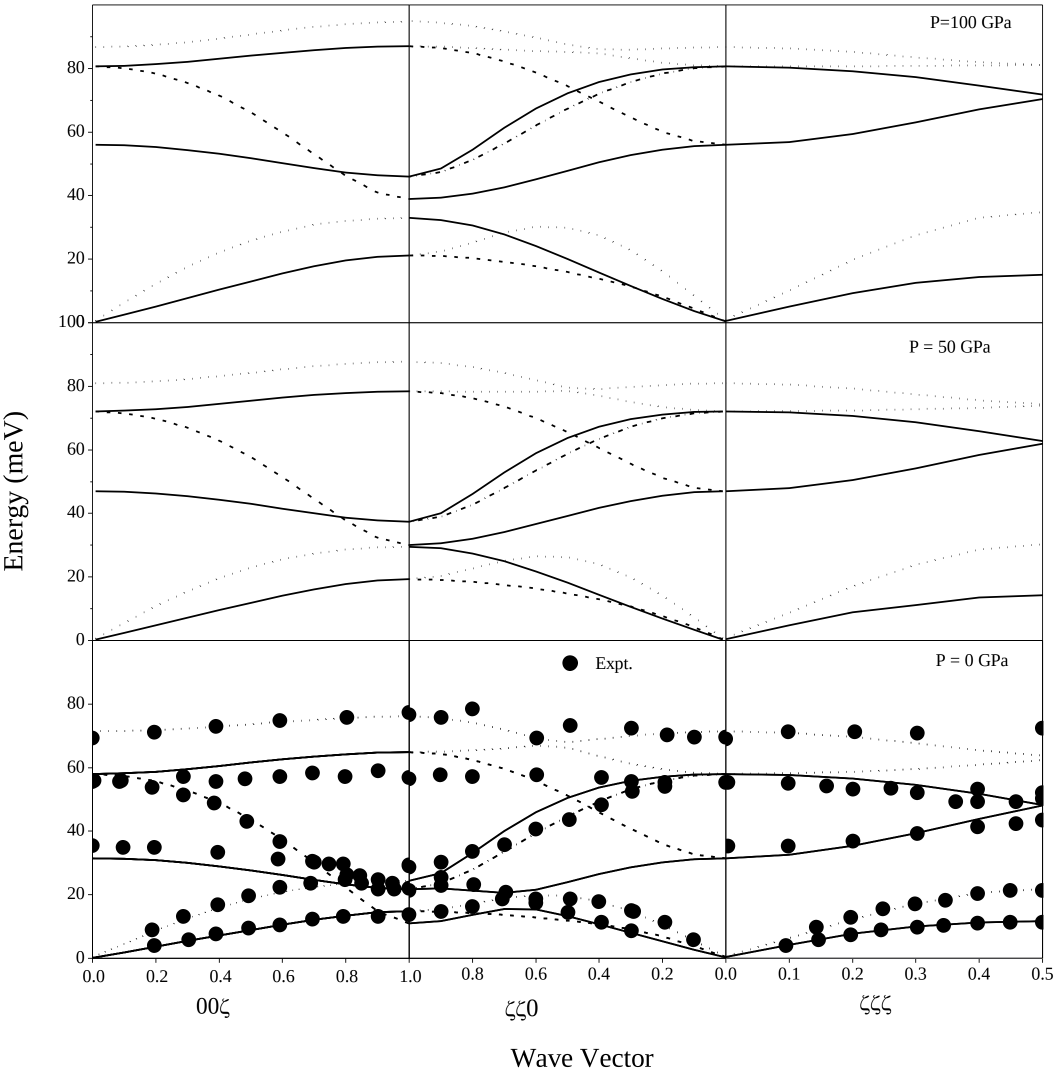

Fig. 2.13: *Calculated (full lines) phonon dispersion relation in UO_2 at P = 0, 50 and 100 GPa. The P = 0 GPa calculated dispersion relations are compared with reported (solid circles) experimental data of Dolling et al [69].*

The energy span at P = 0 GPa is between 0 and 70 meV, at P=50 GPa it is up to 80 meV, while at P=100 GPa it spans up to 90 meV. The peaks in the phonon spectra progressively harden with increase of pressure. The partial densities of states of the oxygen atoms show that they contribute almost throughout the range mainly from 20 to 70 meV at lowest pressure, between 40 to 80 meV at 50 GPa and between 50 to 90 meV at 100 GPa. Uranium atoms's predominant contribution is limited to the lower energy range up to 25 meV and its position remains unchanged with pressure, indicating its much higher stability as compared to the oxygen atoms.

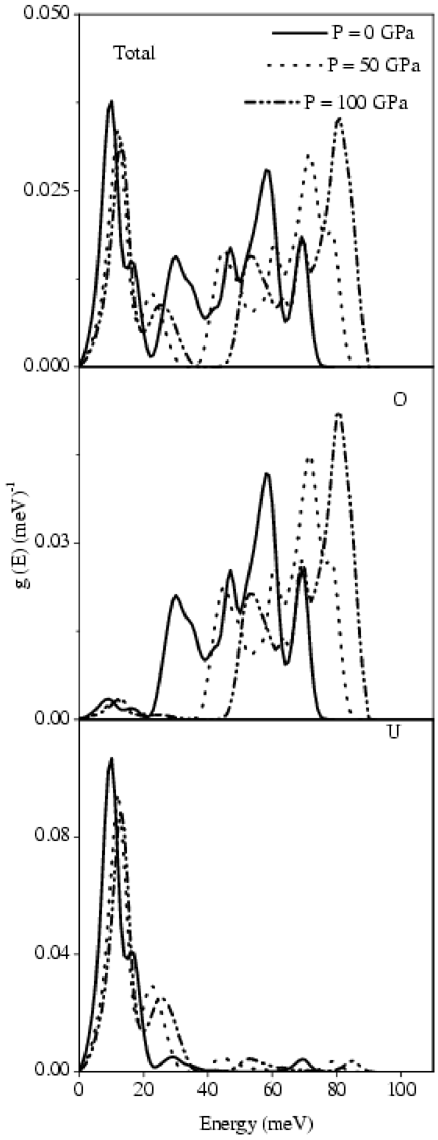

Fig. 2.14 *Phonon density of states at P = 0, 50 and 100 GPa along with the partial density of states for uranium and oxygen.*

Fig. 2.15a gives the computed specific heat $C_P(T)$ compared to reported data [60,71]. Quasiharmonic lattice dynamics calculations significantly underestimate the observed specific heat (full line in Fig. 3a). Taking into account the thermal expansion values obtained from molecular dynamics simulations and temperature variation of bulk modulus, fairly accurate description of the C_P-C_V corrections are obtained. The computed specific heat at high temperature after incorporating these corrections (open circles in Fig. 3a) are in good agreement with experiments [60] and reported molecular dynamics simulations of Yakub *et al* [71].

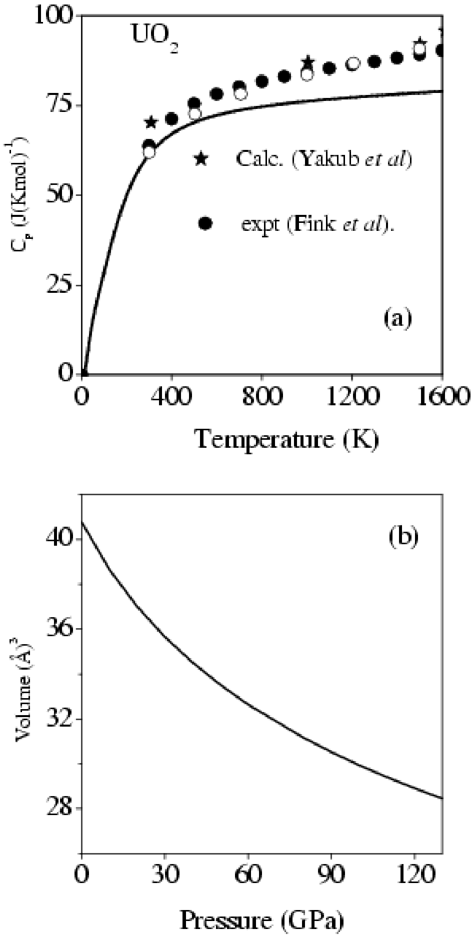

Fig. 2.15(a) *Calculated specific heat at constant pressure. Quasiharmaonic lattice dynamics calculations (full line) significantly underestimate the observed* $C_P(T)$ *(solid circles). Taking into account thermal expansion obtained from MDS and temperature variation of bulk modulus, a fairly accurate description of* $C_P(T)$ *has been obtained (open circles).* ***(b)*** *Equation of state of* UO_2*.*

There are various factors like disordering of the oxygen sub-lattice, electronic excitations, valence- conduction band transitions, *etc.* which play a significant role in the anomalous increase in the specific heat which sets in even before the fast-ion transition.

Defects do not contribute significantly over the 0-1600 K temperature range reported in this study, but divalent Frenkel defects are the predominant form of atomic disorder [72]. The equation-of-state is shown in fig. 2.15(b), however, experimental data for the same is unavailable for comparison. There is a smooth decrease in volume with increase in pressure.

2.2.3.1(b) Diffusion and fast-ion transition

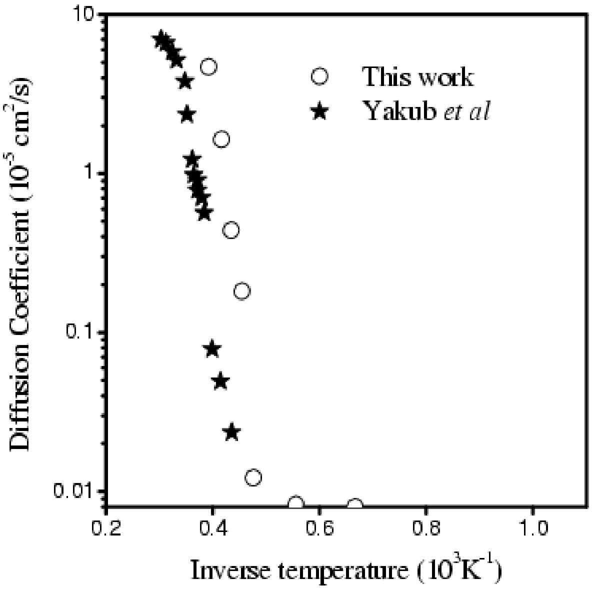

Fig. 2.16 *Oxygen atom's diffusion coefficient, D and its variation with temperature obtained from MD simulations in comparison with those reported by Yakub [71] et al.*

The diffusion coefficient of the oxygen ion has been computed as depicted in Fig. 2.16. High temperature data of the diffusion constant of oxygen in UO_2 is unavailable for comparison. Our molecular dynamics calculations suggest that the superionic phase sets around 2300 K, results have been compared and are found to be in good agreement with those of Yakub *et al* [71]. The signature of a superionic transition is found indirectly in the enthalpy studies on UO_2, since direct measurements are made difficult with high temperatures involved [73-76]. It is found to undergo a *bredig* transition (involving jump in specific heat across the normal to superionic phase transition) at about 2610 K. The diffusion coefficient is comparable to that of a liquid in the superionic phase.

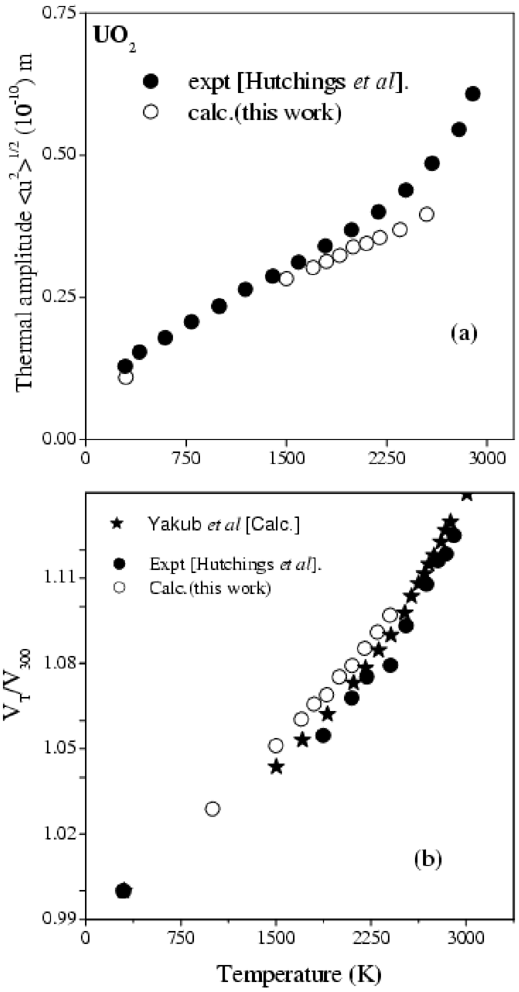

Fig. 2.17 (a) *Calculated (MDS) thermal amplitude of oxygen*$<u2>^{1/2}$ *as a function of temperature (open circles) at ambient pressire amd comparison with experiment [5] (solid circles). (b) Variation of lattice volume with temperature compared with experimental (solid circles) and reported MDS (solid stars, Yakub et al and open circles, this work)*

Calculations of the thermal amplitude using molecular dynamics simulations (open circles) have been compared with experimental results [5] and reported calculations [71] in fig. 2.17a, and are in good agreement. The change in the slope of the plot at the

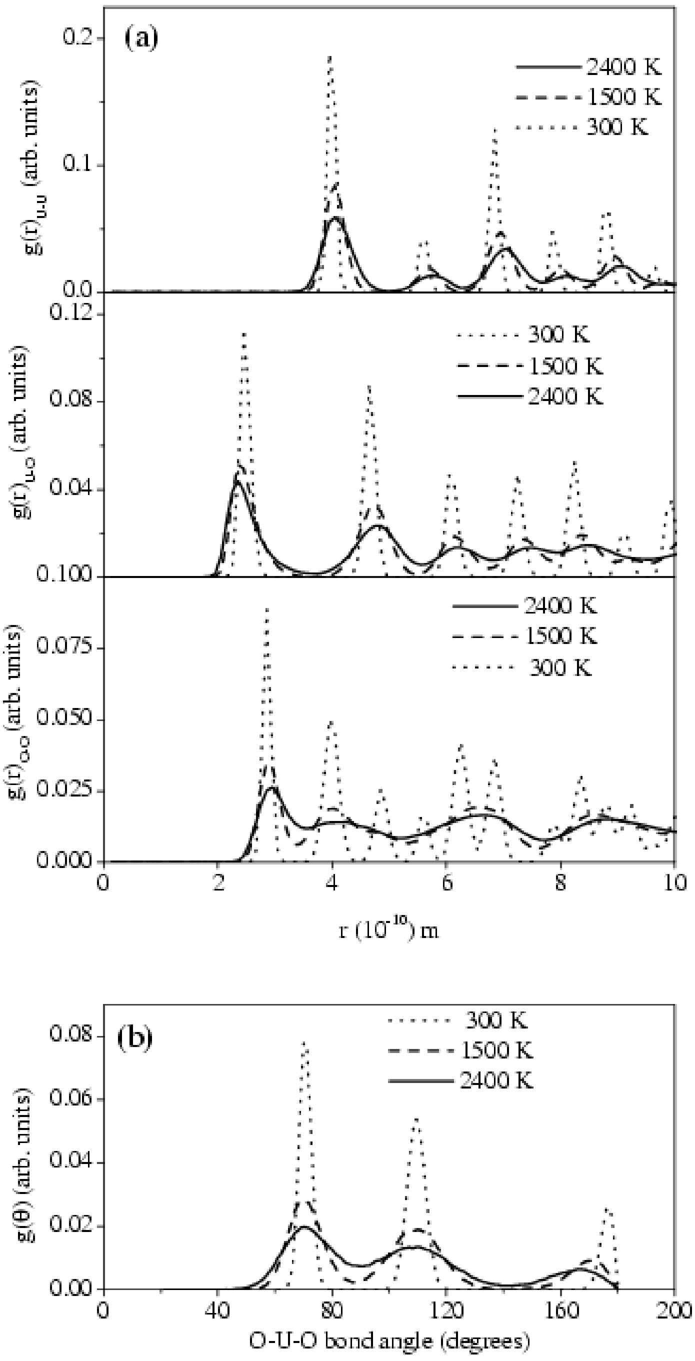

Fig. 2.18(a) *Pair correlation functions of U-U, U-O and O-O and* ***(b)*** *angle-correlation function of O-U-O bond angle in UO2 at different temperatures and at ambient pressure.*

superionic transition (T~2300 K) is seen clearly. The thermal expansion of the unit cell obtained from the MD simulations, which includes anharmomic effects is plotted in fig. 2.17b, agrees well with experiment. In case of the reported experiment [5], the various data points correspond to different crystals and different instruments.The information on the nearest neighbour distances can be obtained from the radial pair correlation functions. The pair correlation of the UO_2 lattice at different temperature from T = 300 K (room temperature) to superionic state at T = 2550 K is plotted in Fig. 2.18(a).

Gradual disordering of the oxygen sub-lattice can be seen with increasing temperature. In the U-U correlation, we can see that there are very little changes in the peak positions. The plots at various temperatures almost overlap completely. We can conclude that the U-U order is almost untouched by the growing thermal disturbances. In case of U-O, little but subtle changes can be seen with increase in temperature. But the maximum changes are seen in the O-O pair correlation, the peaks broaden with temperature increase and at highest temperature investigated, the probability of finding an oxygen atom is nonzero at any point beyond a minimum distance. Similarly, the angle-correlation changes in the O-U-O reveal more fluctuations and a broader character as temperature is raised. From the above discussion we can conclude that the disturbances in the crystal lattice accompanying the superionic transition are limited to the oxygen sub-lattice alone.

2.3 PHONONS, LITHIUM DIFFUSION AND THERMODYNAMICS OF LIMPO$_4$ (M=MN, FE)

2.3.1 INTRODUCTION

Ever increasing energy demands has always promoted research for the elusive perfect battery material, thus paving way for a safer, secure, sustainable energy alternative [13-18]. Lithium transition metal phospho-olivines [19,20,21] have emerged as one of the leading contenders in this race. Since the time they were proposed by Padhi [18,20] et al, they have been actively considered as a potential and viable alternative to the conventional cathode materials like $LiCoO_2$. $LiMPO_4$ have large theoretical capacity [20,21] and a large operating voltage [16,20] . The importance is further accentuated by their stability [22,23], high safety, low cost, low toxicity and cyclability. The electrochemical [24-27] properties of these materials determine Li intercalation and deintercalation [26], vital to their functioning as useful electrode materials. They in turn are determined by their basic structural and thermodynamic properties. Despite enormous works pertaining to battery research [24-30], many aspects of their basic vibrational and other physical properties have not been copiously studied. Studies on delithiated [77-81] $LiMPO_4$, solid solutions have been done to explore methods to increase conductivity in these compounds [77-85] . There have been several first principle studies of their electronic properties [85-100a], Li diffusion [91-96], easy direction of lithium diffusion [97-100], inelastic neutron scattering on unmixed and disordered $Li_{0.6}FePO_4$ [101], magnetic behavior, theoretical studies on their vibrational properties and a few Raman, infrared studies on zone centre phonon modes [102-106].

At ambient conditions, these compounds crystallize in olivine type (Fig. 2.19) orthorhombic Pnma [107] space group analogous to mineral Triphylite structure. $LiMPO_4$ are paramagnets above their Neel temperatures. In case of $LiFePO_4$ [108-110], below T_N= 50 K, Fe^{2+} spins align collinear with b-axis, while in $LiMnPO_4$ [111,112], Mn^{2+} spins align along a-axis below T_N = 34 K. The structure comprises of discrete PO_4 tetrahdera and highly distorted oxygen octahedra about lithium and transition metal ion, M. The PO_4 tetrahdra are irregular, with two significantly different sets of O-O distances.

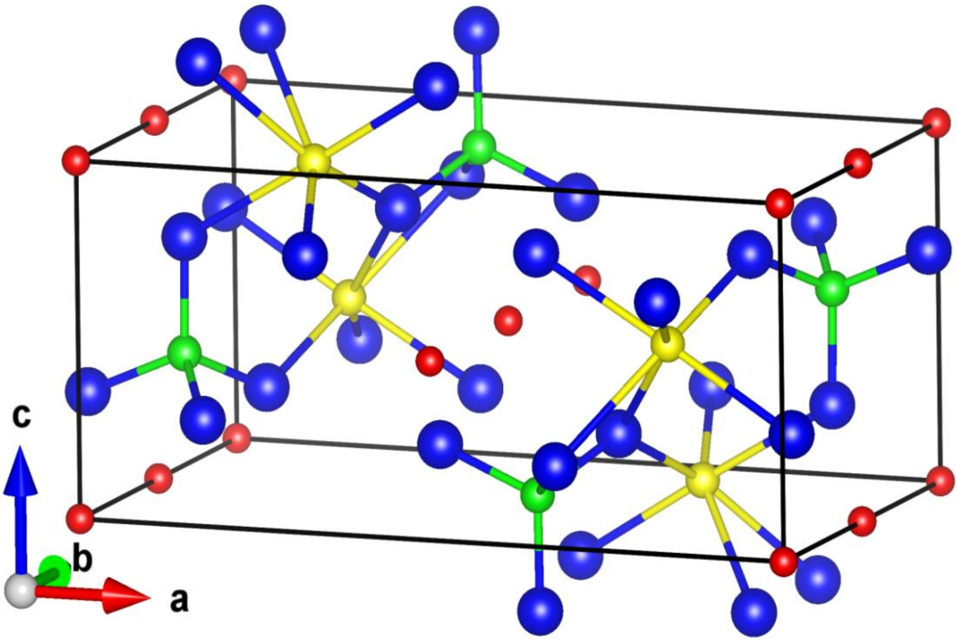

Fig.2.19 Structure of $LiMPO_4$ (M=Mn, Fe) (orthorhombic Pnma space group) derived from *xcrysden* software at T = 0 K. Key; Li: Red spheres, M=Mn or Fe: Yellow spheres, P: Green spheres, O: Blue spheres.

A rich collection of studies on these compounds relating to its technological applications are available in literature. But low electronic conductivity and low lithium diffusivity plague [113], the effective use of these compounds as battery materials. There have been several studies on methods [114-127], to overcome these limitations. There are reports on super-valence ion doping in Li-site, doping in M-site, nanocomposite LiFePO4/carbon powder, thermal treatment and carbon coating to improve upon its poor lithium transport in solid-state. There are studies to determine the preferable directions of Li diffusion, quantitative values of D_{Li} (diffusion coefficient) [81,122], in LiFePO4 using, muon spectroscopy [94,95], as well as first principles method. The chemical diffusion coefficient of Li has been studied using galvanostatic intermittent titration techniquene [122-124]. Atomistic studies on the role of defects in Li transport have been studied [125]. Effect of non-stoichiometry, strain and doping on Li diffusion [126,127] in both LifePO4 and $LiMnPO_4$ [81] has also been extensively studied. Carbon coating of $LiMPO_4$

[115] and vacancies [97] in the lattice are found to increase the conductivity of these compounds.

Our interest in this study has been to understand the dynamics of these compounds and plausible role of phonons in triggering the lithium ion movement. In this work the author has studied phonons in the entire Brillouin zone, diffusion of lithium and microscopic picture of the disturbances occurring in the lattice with increasing temperature. Inelastic neutron scattering measurements of the phonon density of states has been reported for the first time and its calculation using shell model. The model calculations are in good agreement with the inelastic neutron scattering data. This allowed testing of our model, which is used to explore the possibility of Li diffusion using molecular dynamics simulations.

2.3.2 EXPERIMENTAL DETAILS

Polycrystalline samples of $LiMnPO_4$ and $LiFePO_4$ were synthesized by the solid state reaction of appropriate reactants. $LiMnPO_4$ was synthesized from the stoichiometric ratio of $NH_4MnPO_4.H_2O$ and Li_2CO_3 in argon atmosphere at 750 °C. $NH_4MnPO_4.H_2O$ was prepared by precipitation from $MnCl_2$ solutions using aqueous ammonia. $LiFePO_4$ was synthesized by the reaction between Li_2CO_3, Fe_2O_3 and $NH_4H_2PO_4$ and glucose at 700 °C in flowing N_2 atmosphere. Glucose was used as reagent for reducing Fe^{3+} to Fe^{2+}.

The inelastic neutron scattering measurements of the phonon density of states in the polycrystalline samples of $LiMPO_4$ (M=Mn,Fe) has been performed using the IN4C time of flight spectrometer at the Institut Laue-Langevin (ILL), in Grenoble, France. About 10 grams of polycrystalline samples were used in thin aluminum foil. Sample thickness was about 2 mm. The measurements at 300 K were performed in the neutron-energy gain mode with incident neutron energy of 14.2 meV (2.4 Å). The elastic energy resolution is 0.5 meV. The energy resolution of the instrument varies from a minimum of 0.5 meV to 10% of the energy transfer. The detector bank covered scattering angles from 10° to 110°. The signal is corrected for the contributions from the empty cell and suitably averaged over the angular range using the available software package at ILL. A standard vanadium sample was used to calibrate the detectors.

2.3.3 COMPUTATIONAL DETAILS

The lattice dynamics calculations has been performed using empirical potential as described in equation (1.25) and (1.26) in chapter 1 .Our empirical calculations have been carried using interatomic potentials consisting of Coulomb and short-range Born-Mayer type interaction terms. The term C_{ij} =100 eVÅ^6 accounts for the van der Waals interaction between O-O pairs. The effective charge Z(k) and radii R(k) parameters used in our calculations are Z(Li)= 1.0 , Z(Fe/Mn)= 1.869 Z(P)= -3.581.6, Z(O)= -1.6125 , R(Li)= 1. 35 Å, R(Fe)= 1.88 Å, R(Mn)= 1.91 Å , R(P)= 1.20,and R(O)= 1.65 Å. The polarizability of the oxygen atoms is introduced in the framework of the shell model [67]. The shell charge and shell core force constants for oxygen atoms are −2.00 and 60 eV/Å^2 respectively. The parameters of the potentials satisfy the conditions of static and dynamic equilibrium.

Classical molecular dynamics calculations have been carried out to understand the diffusion of lithium ions with increasing temperature. The interatomic potential parameters are the same as those obtained from our lattice dynamics simulations except that the oxygen polarizability was not included. The evolution of the super cell consisting of 7056 ions (4**a** × 7**b** × 9**c**) has been carried out in the NPT ensemble. The mean-square displacements of atoms and pair correlation between pairs of atoms have been calculated using the simulations.

2.3.4 RESULTS AND DISCUSSION

2.3.4.1 Phonon Density of States

The measured neutron inelastic scattering spectra at room temperature with incident neutron energy of 14.2 meV are shown in Fig.2.20. The geometrical constraints of the instruments have allowed collecting the data from about 1 to 7 Å^{-1}. We find that for data summed over 1 to 7 Å^{-1} the phonon spectra of both the $LiMPO_4$ (M=Mn, Fe) consist of a strong peak between 0 and 8 meV. The Raman and infrared measurements do not indicate zone-centre optic modes at such low energies [102-104]. In order to understand the origin of the peak, experimental data were grouped in two different regimes namely, high Q (4 to 7 Å^{-1}) and low Q (1 to 4 Å^{-1}) respectively. We find that for high Q data the intensity of the low energy excitations between 0 and 5 meV have decreased strongly, while low Q data indicate substantial increase in intensity of the same peak. The magnetic signal is expected [67] to be more pronounced at low Q, **and decrease strongly at high Q**, following the magnetic form factor.

Further S(Q,E) plots for $LiMPO_4$ (M=Mn, Fe) are shown in Fig. 2.21. As mentioned above both the compounds have antiferromagnetic ordering below 50 K. The Fe [108-110] and Mn [111,112] compounds show antiferromagnetic ordering below 52 K and 35 K respectively. Strong intensity at 300 K around 5 meV in $LiFePO_4$ is due to paramagnetic scattering of the compounds. In case of $LiMnPO_4$ paramagnetic scattering is below 3 meV. The magnetic scattering is seen (Fig. 2.21) as a broad quasi elastic like signal centered around 0 meV in the S(Q,E).

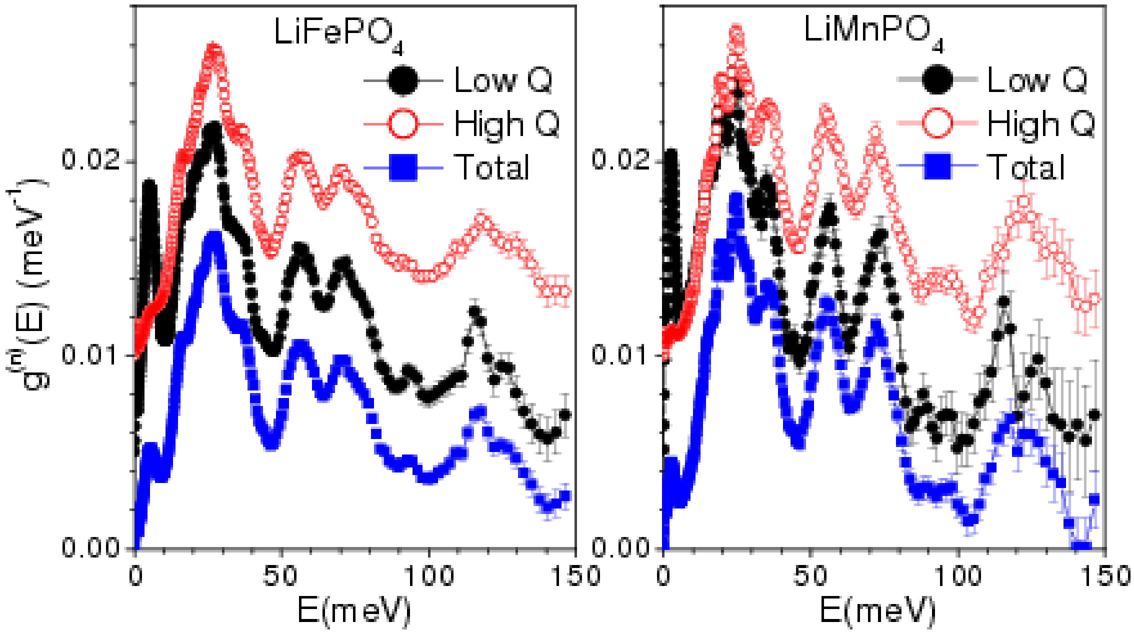

Fig. 2.20 The experimental neutron inelastic scattering spectra of $LiMPO_4$ (M=Mn, Fe) at 300 K. For better visibility the low Q and high Q spectra are shifted along the y-axis by 0.005 meV^{-1} and 0.01 meV^{-1} respectively.

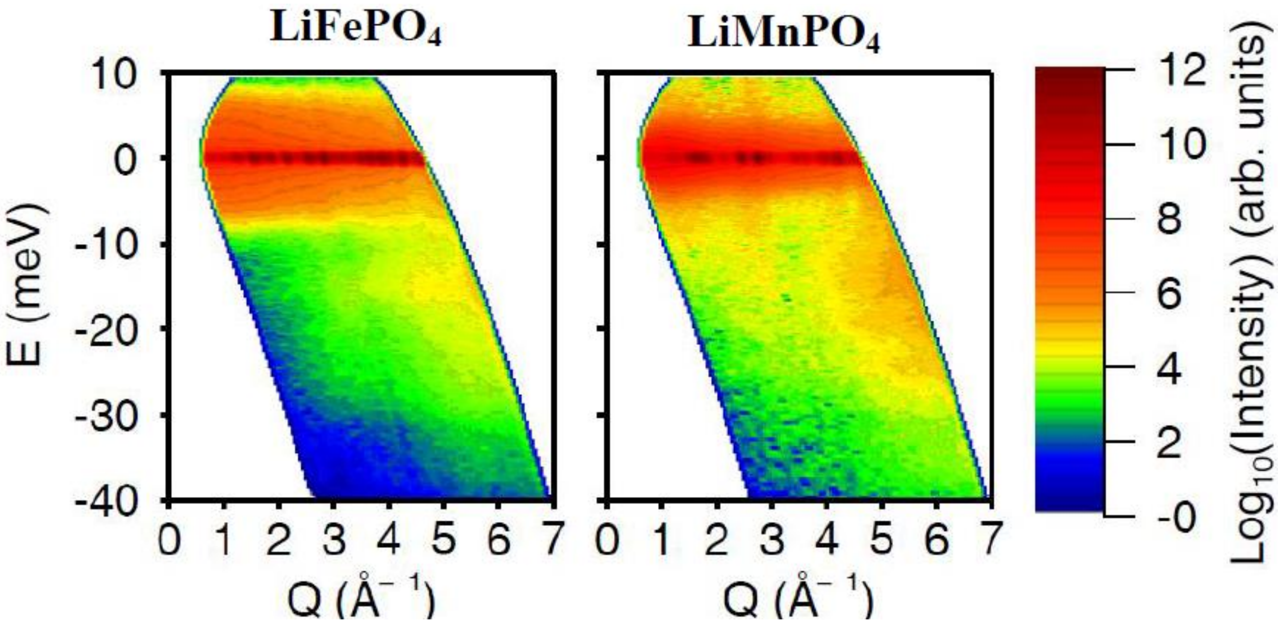

Fig. 2.21 *The experimental S(Q,E) plots for $LiMPO_4$ (M=Mn, Fe) at 300 K.*

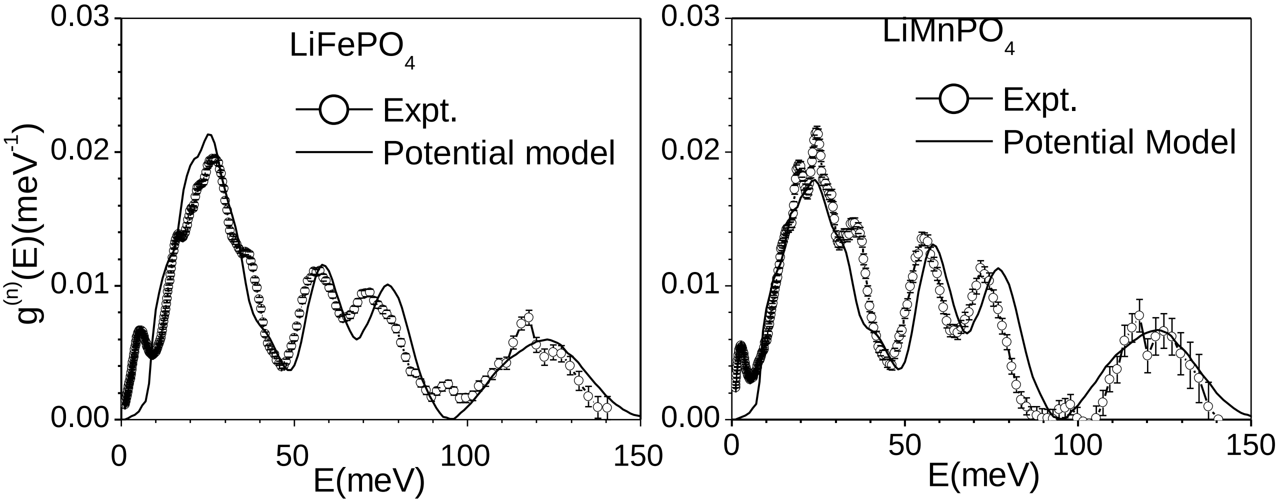

***Fig. 2.22** The comparison of the calculated and experimental neutron inelastic scattering spectra for LiMPO$_4$ (M=Mn, Fe) at ambient pressure at 300 K. The ab-initio as well as potential model calculations are carried out at 0 K. The multi-phonon contribution calculated using the Sjolander formalism [128(b)] has been subtracted from the experimental data. The experimental spectra comprises of magnetic and phonon contribution, while computed results pertain to phonon contribution alone.The calculated spectra have been convoluted with a Gaussian of FWHM of 0.5 meV to 10% of the energy transfer in order to describe the effect of energy resolution in the experiment.*

There are already experimental data [109,111] on the presence of magnetic excitations below the Neel temperatures, where energy of such excitations is around 5 meV in LiFePO$_4$; and below 3 meV in LiMnPO$_4$. Hence we can consider the lowest energy peaks in these compounds at 300 K to be due to paramagnetic scattering.

Fig. 2.22 gives the neutron weighted density of states of the powder samples in LiFePO$_4$ and LiMnPO$_4$ in comparison with the calculated model potential results. The multiphonon spectra have been calculated using the Sjolander 128[b] formalism and subtracted from the experimental data. The phonon spectrum extends up to 150 meV. The experimental spectrum consists of several peaks at 25, 55, 75 and 120 meV. No modes are observed for energies between 85 and 105 meV. The general characteristics of the experimental features are well reproduced by the calculations. The parital contribution of the constituent atoms to the total phonon density of states in the two olivines computed using model calculations is shown in Fig. 2.23. We find that Fe/Mn ions contribute largely below 40 meV, while Li being lighter contributes up to 75 meV. The density found beyond 105 meV is only due to the stretching modes of the PO_4 polyhedra.

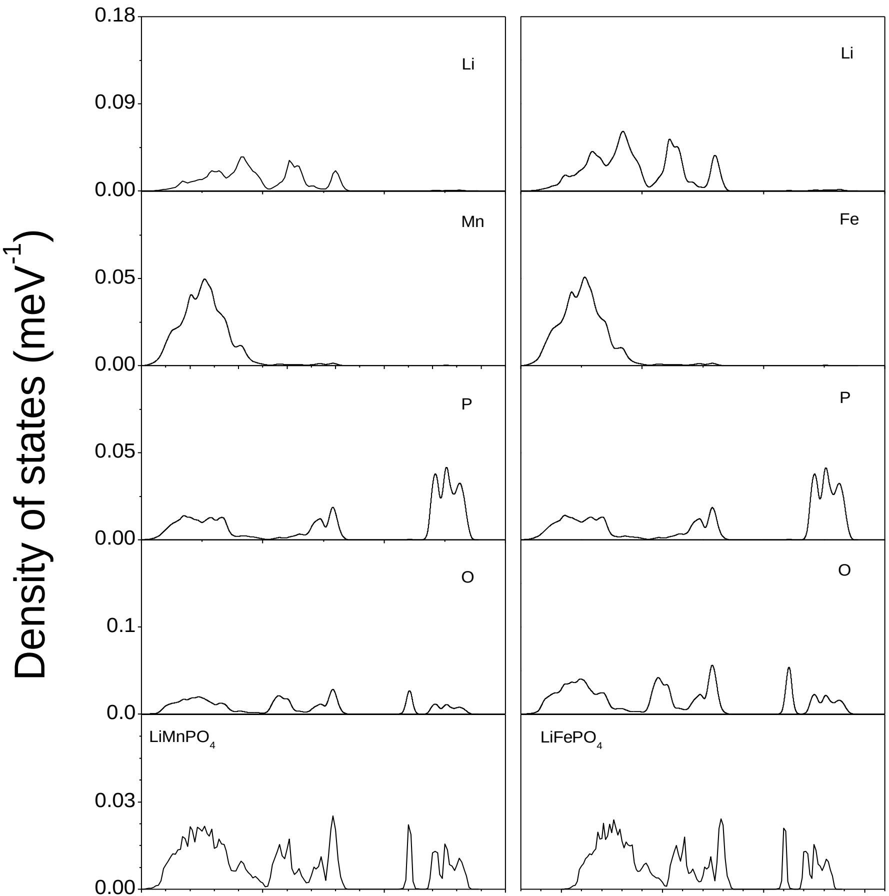

Fig. 2.23 *The calculated partial densities of states in $LiMPO_4$ (M=Mn,Fe) using potential model.*

2.3.4.2 Thermal Expansion, Diffusion Coefficient and Pair Correlation Function

Molecular dynamics simulations have been carried out using a supercell of 7056 atoms to study its evolution with increasing temperature. The system has been allowed to evolve for 80 picoseconds at each temperature. The thermal expansion of $LiMPO_4$ (M=Mn,Fe) has been calculated using model potentials in the quasiharmonic approximation and molecular dynamics simulations. The results have been compared with available experimental data [79,102 (a)] in Fig. 2.24.

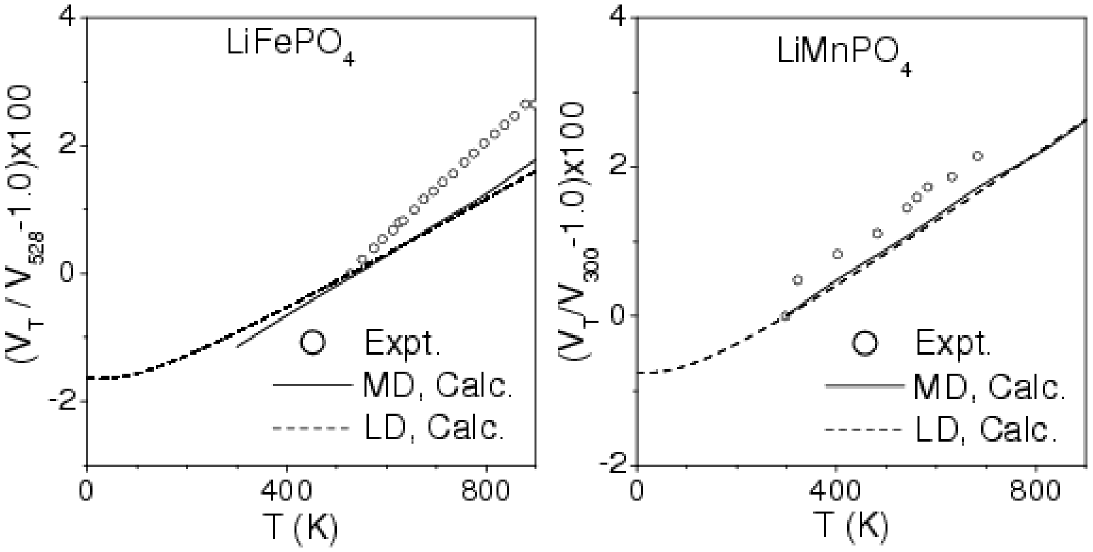

Fig. 2.24 *Comparison between the experimental [79,102(a)] and calculated volume thermal expansion of $LiMPO_4$ (M=Mn, Fe). The dashed and full lines correspond to classical lattice dynamics (LD) and molecular dynamics (MD) calculations respectively.*

There is a slight deviation between the calculated and experimental thermal expansion for $LiFePO_4$. The quasiharmonic calculations agree very well with the molecular dynamics simulations, suggesting that there are not very explicit temperature effects in the lattice with increasing temperature. But we did not notice any perceivable diffusion (comparable to that of liquids, i.e of the order of 10^{-9} m^2/s) of lithium from our results, which indicates that diffusion coefficient is well below 10^{-10} m^2/s, beyond the scope of our molecular dynamics simulations. At 300 K, the galvanostatic and potentiostatic [122-124] intermittent titration of the most diffusing member has yielded values between 10^{-14} and 10^{-18} m^2/s for diffusion of lithium (D_{Li}) ions in solid solution of Li_xFePO_4 and $Li_{1-x}FePO_4$ (X < 0.02), respectively. GITT, electrochemical impedance spectroscopy (EIS) and cyclic voltammetry (CV) have been carried out to obtain D_{Li} [122-124] in thin films of $LiFePO_4$, these values are also in the order of 10^{-14} m^2/s. Self diffusion coefficient of Li^+ at 300 K measured using Mossbauer, muon-spin relaxation [94,95] is 3.6 x 10^{-14} m^2/s in $LiFePO_4$.

Experimental visualization [97,98] of lithium diffusion has been reported in delithiated $Li_{0.6}FePO_4$. The diffusion of the constituent atoms in $LiMPO_4$ (M=Mn,Fe) was monitored in our molecular dynamics simulations. As expected lithium exhibits maximum mean square displacement as seen in Fig. 2.25 in both the compounds, which is very good agreement with Zhang et al [100] and Islam et al [125].

Yang *et al* have carried out ab-initio molecular dynamics study [99] to understand Li diffusion mechanism in $LiFePO_4$. The authors find that there is no macroscopic diffusion till 2000 K, beyond 2000 K Li diffuses in a curvaceous path, thermal vibration of trapped Li ions is quite anisotropic with a preferred direction towards face-shared tetrahedral Li sites. The authors also discuss about another possibility of Li ion migration involving the formation of Li-Fe antisite defect. It has been concluded that Li diffusion in $LiFePO_4$ is far more complex than suggested by previous researchers [91-100]. This concludes that these compounds in the pure form cannot be considered to belong to the family of superionic conductors [1]. The coefficient of diffusion of lithium in these compounds is reported to be around 10^{-12} m^2/s, about three orders lower than that of a liquid (10^{-9} m^2/s), which is the typical value for a superionic conductor. The various experimentally reported values of D_{Li} in the literature are found to be several orders of magnitude lesser than reported calculated values. The experimentally measured D_{Li} falls in the range of 10^{-17} to 10^{-11} m^2/s, which is the range suitable for a cathode material, hence finds extensive use in rechargeable batteries.

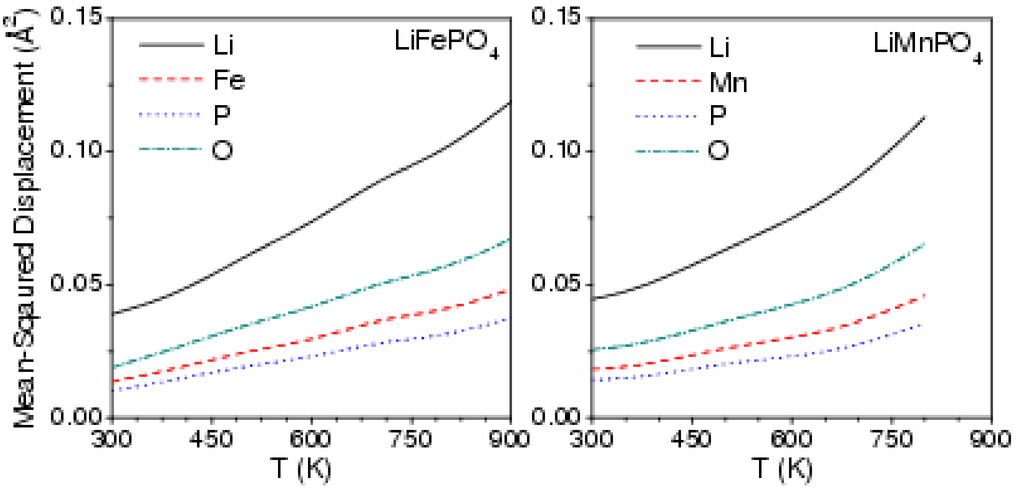

Fig.2.25 *Mean-Squared Displacement of constituent atoms in* $LiFePO_4$ *and* $LiMnPO_4$ *with increasing temperature using molecular dynamics simulations.*

The pair correlations between two atoms indicate the probability of finding a given type of atom with respect to the atom considered. Fig. 2.26 and show the pair correlation between various ion pairs in both the compounds at different temperatures. The correlation between Li ions shows some noticeable changes with increasing temperatures; at 1100 K there are some subtle changes in the atomic arrangement of lithium .This shows that with increase in temperature, there are readjustments occurring continuously in the Li-sub-lattice. In case of correlations between Fe-P, Li-P and Li-Fe there are very small changes indicating that the positions of these atoms have not changed with respect to each other. There are some small changes in the correlations between Fe-O, P-P, Li-O, Fe-Fe and O-O. The P-O correlations are virtually undisturbed with increase in temperature, suggesting that PO_4 unit remains rigid, but there are some discernable changes in the orientations of the PO_4 polyhedra, particularly with respect to Li-sublattice. The correlations between Li-O show discernable changes at 1100 K as against the room temperature results.

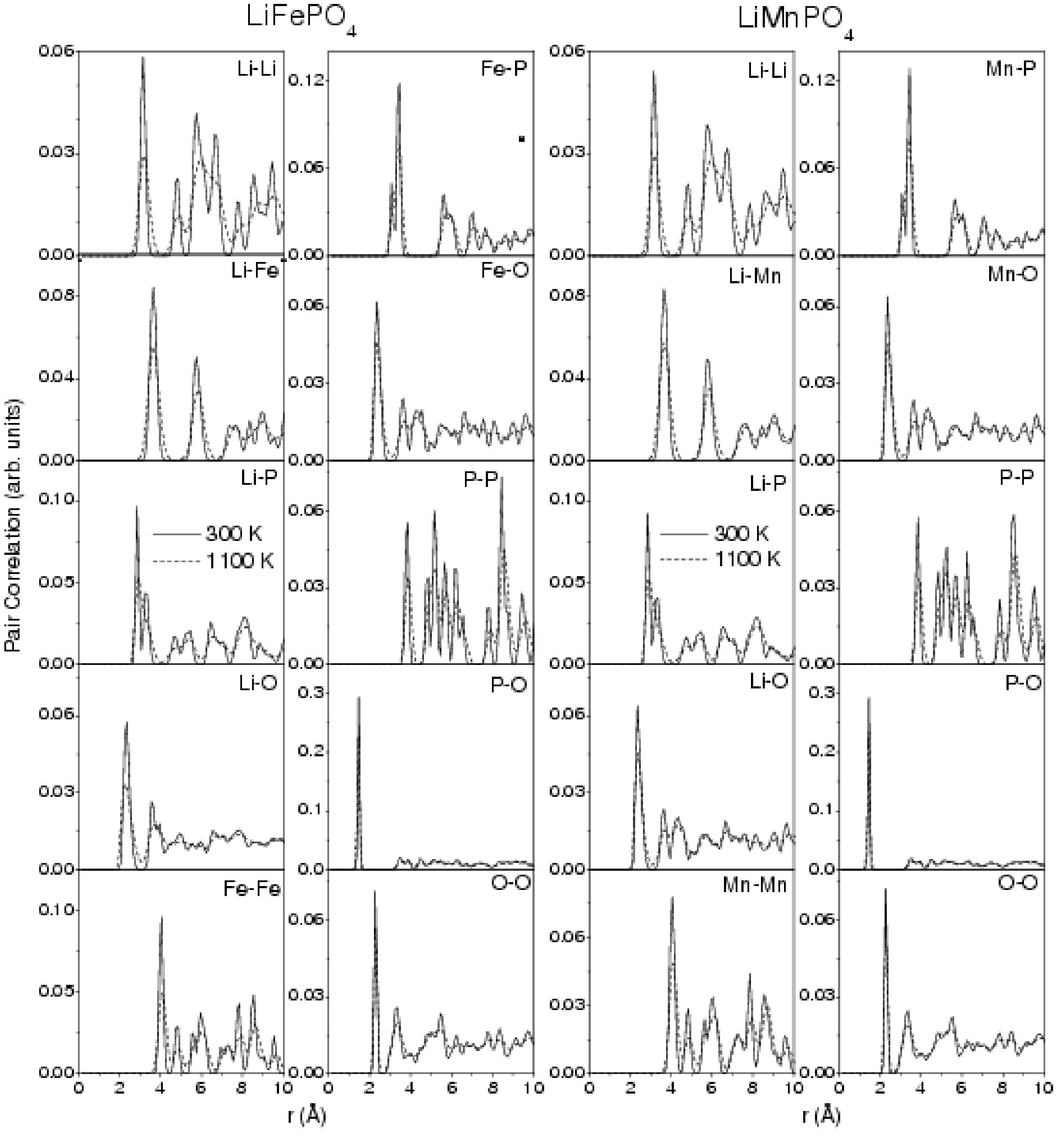

Fig. 2.26 *Pair correlation function of different pairs of atoms in the olivines at various temperatures; 300K - Solid line ; 1100 K- dashed line.*

These results are in agreement with those of Zhang et al [100]. The behavior of the two olivines is similar with increase in temperature. Nevertheless the disturbance in the lattice appears to be very little and does not suggest large scale diffusion in case of both the compounds. The presence of well defined correlation peaks at higher temperature, of the various pair points out to the fact that the compounds are stable and increased disturbances in lithium sub-lattice is a local effect and does not bring about any drastic change to the overall lattice.

2.4 CONCLUSIONS

Shell model potentials have been successfully used to study the phonon properties of lithium oxide, uranium oxide and battery materials. The interatomic potential is able to reproduce the elastic constants, bulk modulus, equilibrium lattice constant, and phonon frequencies, which are in good agreement with the reported data. The potential has been used to understand the novel properties exhibited by each of these oxides. Possible role of phonons in the triggering of fast ion diffusion in these compounds has been investigated. The microscopic picture of the lattice under such extreme conditions as sublattice melting has been studied. In case of battery materials, the formulated interatomic potential has been validated by inelastic neutron scattering measurements of the phonon density of states.

In case of Li_2O, the calculated phonon dispersion relation is in very good agreement with the reported neutron and light scattering data. There appears no phonon softening even up to high pressures of 100 GPa. Partial densities of state of lithium and oxygen atoms show that they contribute almost in the whole energy span up to 100 meV. There is a greater contribution of lithium in the higher energy side as compared to oxygen, which contributes more on the lower end. This may be explained with regards to their size and mass. The calculated specific heat is in good agreement up to about 1100 K but shows a slower rise as compared to the experimental data when the superionic behavior sets in. Small deviations between the calculation and the experiment, begins to occur even at lower temperature which could be due to some defect generation in the lattice prior to the superionic phase. The diffusion coefficient calculated for lithium ion shows a transition to fast ion phase at around 1000 K whereas in experiment, it is seen to occur around 1200 K. At the transition temperature, lithium atom's diffusion coefficient is comparable to that of a liquid and is in the order of 10^{-9} m^2/s. Application of static pressure of 5 GPa only brings about a marginal change in the transition temperature. The pair correlation functions for Li-Li, Li-O and O-O and the angle distribution for Li-O-Li bring out the following inferences. The pair correlations for Li-Li just show a gradual broadening with increase in temperature from 300 K to 1250 K. The distortions in the lattice due to fast ion diffusion are highly localized, and the local environment remains unchanged to a great extent. These results indicate to a jump diffusion model in which the lithium ions move from one tetrahedral site to another tetrahedral site via octahedral interstitial sites. But nonetheless, they do not occupy any of these octahedral sites. The jump time of the lithium atoms at temperatures above the transition is very small, compared to their residence time at any given symmetry position. As a result, the lattice seems more or less undisturbed. Though there is a considerable movement of lithium atoms, author could not discern any rule governing their movements from one tetrahedral region to another.

Using the abovesaid potential, the behavior of lithium oxide at the onset of superionic transition has been investigated. It is found that around the fast ion transition temperature, zone boundary TA phonon mode along [110] become unstable. This softening of the phonon could be a precursor to dynamical instability. This observation is corroborated by the eigenvector of this mode, and could be one of the factors leading to diffusion of lithium ions. The decrease in elastic constants with increasing temperature, which is one of the characteristic features exhibited by these fast ion conductors has also been studied. Finally author is able to relate the phonon softening with the ease of lithium movement at elevated temperature along [001] as against the other two high symmetry directions considered. These studies would throw better light and aid in improving the utilization of the oxide in its numerous technological applications.

In case of UO_2, the calculated phonon dispersion relation is in very good agreement with the reported neutron scattering data. There is no phonon softening in UO_2 even up to high pressures of 100 GPa. Partial densities of state of uranium and oxygen atoms show that they contribute almost in the whole energy span up to 75 meV. There is a greater contribution of oxygen in the higher energy side as compared to uranium, which contributes more on the lower end. This may be explained with regards to their size and mass. The calculated specific heat is in good agreement up to about 1200 K but shows a slower rise as compared to the experimental data beyond which several other factors like crystal field effects, electronic transitions, defect formation etc start to play role. The diffusion coefficient calculated for oxygen ion shows a transition to the fast-ion phase at around 2300 K whereas in experiment, it is seen to occur around 2670 K. At the transition temperature, oxygen atom's diffusion coefficient is comparable to that of a liquid and is in the order of 10^{-9} m^2/s. The pair correlation functions for U-U, U-O and O-O and the angle distribution for O-U-O bring out the following inferences. The pair correlations for O-O just show a gradual broadening with increase in temperature from 300 K to 2550 K. The distortions in the lattice due to fast-ion diffusion are highly localized, and the local environment remains unchanged to a great extent. As a result, the lattice seems more or less undisturbed.

A combination of inelastic neutron scattering, model lattice dynamics and molecular dynamics simulations calculations has been successfully used to understand the phonon dynamics and high temperature behavior in $LiFePO_4$ and $LiMnPO_4$. The measured phonon density of states is in excellent agreement with our theoretical calculations. Our molecular dynamics simulations suggest that diffusion coefficient of lithium is less than 10^{-10} m^2/s in pure compounds, which is in agreement with reported results. Although lithium has maximum mean square displacement, it does not show any macroscopic diffusion, akin to a liquid. The pair correlation also suggest that there are subtle changes and disturbances occurring in the Li sub lattice, while PO_4 remains structurally unaffected even up to the highest temperatures studied. Our calculations find the compounds to be thermally stable beyond 1000 K. Our exhaustive studies on their vibrational and thermodynamical properties will be useful in improving the utilization of $LiMPO_4$ (M=Mn,Fe) in numerous technological applications.

References

[1] Stephen Hull Rep. Prog. Phys. **67** 1233 (2006)

[2] T W D Farley, W Hayes, S Hull, M T Hutchings and M J Vrtis, J Phys.: Condens. Matter **3** 4761 (1991)

[3] R W G Wyckoff *crystal structures 2nd ed.* (Wiley, New York, 1963)

[4] J J Carbayo, G L Yodu, S G Popuv and V K Ivanov J. Phys.: Condens. Matter **299** 181 (2001)

[5] M. T. Hutchings, J. Chem. Soc. Faraday Trans. 2 **83** 1083 (1987)

[6] J G Vandu Laan, H Kawamura, N Roun and D Yamaki, J. Phys.: Condens. Matter **283-287,** 99 (2000)

[7] J Ralph, G J Hyland, J. Phys.: Condens. Matter **132**, 76 (1985)

[8] D A MacInnes and C R A Catlow, J. Nucl. Mater. **89**, 354 (1980)

[9] D Manara, C Ronchi, M Sheindin, R Konings, J. Nucl. Mater. **362**, 14 (2007)

[10] D A Keen, J. Phys.: Condens. Matter **14**, R819 (2002)

[11] G L Kalucinki, J. Nucl. Mater. **141**, 3 (1986)

[12] R Shah, A De Vita, H Heine and M C Payne **53**, 8257 (1996)

[13]. J. M. Tarascon and M. Armand, Nature, , **414**, 359, (2001)

[14] J. W. Fergus, J. Power Sources, ,**195,** 939 (2010);. J. B Goodenough, Sol. Stat. Ionics, **69**, 184 (1994)

[15] B. Scrosati and J. Garche, J. Power Sources, ,**195**, 2419 (2010)

[16] P. G. Bruce, Chem. Commun., , **19**, 1817 (1997).

[17] M. S. Whittingham Chem. Rev., , **104**, 4271 (2004)

[18] A. K.Padhi, K. S.Nanjundaswamy and J. B Goodenough., J. Electrochem. Soc.,, **144**, 1188 (1997)

[19] A. K. Padhi, K. S. Nanjundaswamy, C. Masquelier, S. Okada and J. B. Goodenough, J. Electrochem. Soc., , **144**, 1609 (1997)

[20] Wu Borong, Ren Yonghuan and Li Ning, (2011). $LiFePO_4$ Cathode Material, Electric Vehicles“ The Benefits and Barriers, Dr. Seref Soylu (Ed.), ISBN: 978-953-307-287-6, InTech, Available from: http://www.intechopen.com/books/electric-vehicles-the-benefits-and-barriers/lifepo4-cathode-material

[21] H. Huang, S. Yin and L. F. Nazar, Electrochem. Sol-St. Lett., , **4**, A170 (2001); H. Matsuia, T. Nakamura, Y. Yamada, Y. Kobayashib, 15th international meeting on Lithium Batteries-IMLB (2010), electrochemical Society

[22] S. Anna Andersson,, John O. Thomas, Beata Kalska, and Lennart Häggström, Electrochem. and Solid-State Lett., , **3,** 66 (2000); A. B. Mayza, M. Ramanathan, R. Radhakrishnan, S.Ha, V. Ramani., J. Prakash and K. Zaghib, ECS Trans., , **35**, 177 (2011).

[23] P. S. Herle, B. Ellis, N. Coombs and L. F. Nazar, Nat. Mater., , **3**, 148 (2004).

[24] Y. Xu, S. Chung, J. T Bloking., Y Chiang. and W. Y.Ching, Elect. Sol-St. Lett., , **7**, A131 (2004)

[25] A. Yamada, Y. Kudo and K. Liu, J. Elect. Soc., , **148**, A747 (2001).

[26] R. Malik, F. Zhou, G. Ceder, Nat. Mater., , **10**, 587 (2011); C, Delmas,.; M. Maccario,.; L Croguennec,.; F. L Cras,.; F.Weill, Nat. Mater., , **7**, 665 (2008); W. C. Chueh, F. E. Gabaly, J. D. Sugar, N. C. Barlelt, A. H. McDaniel, K. R. Fenton, K. R. Zavadil, T. Tyliszczak, W. Lai and K. F. Mccarty, Nano Lett., , **13**, 866 (2013).

[27] B. Ellis, L. K. Perry, D. H. Ryan and L. F. Nazar, J. Am. Chem. Soc., , **128**, 11416 (2006)

[28] R. Amin, J. Maier, P. Balaya, D. P. Chen and C. T. Lin, Sol. St. Ion., , **179**, 1683. (2008)

[29] M.S. Whittingham, Y. Song, S. Lutta, P. Y. Zaalij, N. A. Chernova, J. Mat. Chem., **15**, 3362 (2005)

[30] S. Chung, J. T. Bloking and Y. Chiang, Nat. Mater., , **1**, 123 (2002)

[31] J G Rodeja, Modeling Simul. Mater. Sci. Engineering, **9**, 81 (2001).

[32] R M Fracchia, G D Barrera, N Allan, T H K Barron and W C Mackrodt, J. Phys. Chem.. Solids, **59**, 435 (1998).

[33] A. De Vita, I. Manasidis, M. J. Gilan and J. S. Lin, Europhysics Letters **19**, 605 (1992).

[34] J. H. Strange, S. M. Rageb, A. V. Chadwick and K. W. Flack, J. Chem. Soc. Farad. Trans., **86**, 1239 (1990).

[35] S. Albrecht, G. Onida and L. Reining, Phys. Rev. B **55**, 10278 (1997).

[36] P. W. M. Jacobs and M L Vernon, J. Chem. Soc Farad. Trans., **86**, 1233 (1990).

[37] A. Shukla, M. Dolg and P. Fulde, J. Chem. Phys. **108**, 8521 (1998).

[38] R. Dovesi, C. Roetti, C. Freyria-Fava and H. Prencipe, Chem. Phys. **156**, 11 (1991).

[39] J. X. M. Zheng-Johannson and R. L. McGreevy, Solid State Ionics, **83**, 35 (1996).

[40] K Ihata and H Okazaki, J. Phys: Condens. Matt. **9**, 1477 (1997); Martin Wilkening, S Indris and P Heitjans, Phys. Chem. Chem. Phys. **5**, 2225 (2003).

[41] A. De Vita, M. J. Gilan, J. S. Lin, M. C. Payne, I. Stich and L. J. Clarke, Phys. Rev. Lett. **68**, 3319 (1992).

[42] S. Hull, T. W. D. Farley, W. Hayes and M. T. Hutchings, J. Nucl. Mater. **160**, 125 (1988).

[43] [a] T. Kurusawa, T. Takahashi, K. Noda, H. Takeshita, S. Nasu and H. Watanbe, J. Nucl. Mater. **107**, 334 (1982); [b] A. Lazicki, C S Yoo, W. J. Evans, P. E. Pickett, Phys. Rev. B 73, 184120 (2006).

[44] T Tanifugi, K. Shiozawa and S. Nasu, J. Nucl. Mater. **78**, 422 (1978).

[45] Y. Oishi, Y. Kamwei and M. Akuyama, J. Nucl. Mater. **87**, 341 (1979).

[46] T. W. D. Farley, W. Hayes, S. Hull and R. Ward, Sol. St. Ionics, **28-30**, 189 (1988).

[47] T. Osaka and I. Shindo, Sol. St. Comm. **51**, 421 (1984).

[48] S Hull, D A Keen Phys. Rev. B **58**, 14387 (1998)

[49] D A Keen S and Hull J. Phys.: Condens. Matter **7**, 5793 (1995)

[50] M Hofmann, S. Hull, G J McIntyre and C C Wilson, J. Phys. Cond.

Matter 9 845 (1997)

[51] Masatomo Yashima, Qi Xu, Akira Yoshiasa, Satashi Wada J. Mat.

Chem. **16** , 4393 (2006)

[52] W G Kleppmann, J. Phys. C 19 7167 (1986)

[53] M M Elcombe and A W Pryor, J. Phys. C 3 492 (1970)

[54] M H Dickens, W Hayes, P Schnabel, M T Hutchings, R E Lechnu and B Renker, J. Phys. C 16, L1 (1983)

[55] M T Hutchings, K Clausen, M H Dickens, W Hayes, J K Kjems, P G Schnabel, C Smith J. Phys. C **12**, 3941 (1984)

[56] M Wilkening, S Indus, P Hutjans, Phy. Chem. Chem. Phys. **5**, 2225 (2003)

[57] A De vita, M J Gilan , J S Lin, M C Payne, I Srichand and L J Clarke, Phys. Rev. Lett. **68**, 3319 (1992)

[58] P Browning, G Hyland, J Ralph, High Temp.- High Pres. **15** 169 1983

[59] K Clausen, W Hayes, M T Hutchings, J K Kjems, J E Macdonald and R Osborn, High Temp. Sci. **19** 189 (1985)

[60] J K Fink, M G Chasanov, L Leibowitz, J. Nucl. Mater. **102** 17 (1981)

[61] G J Hyland and J Ralph High Temp. –High Pres. **15** 179 (1983)

[62] J Ralph, G J Hyland, J. Nucl. Mater. 132 76 (1985)

[63] S Hull, T W D Farley, W Hayes, M T Hutchings, J. Nucl. Materials **160** 25 (1988)

[64] T Tanifugi, K Shiozawa, S Nasu, J. Nucl. Mats, 78 422 (1978)

[65] G. Venkataraman, L. Feldkamp, V. C. Sahni: *Dynamics of perfect crystals,* MIT press, Cambridge (1975); P. Bruesh: *Phonons: Theory and experiments* (Springer-verlag, Berlin 1986).

[66] O. V. Kovalev, *Irreducible representations of space groups* (Gordan and Breach, N. Y. 1964)

[67] K. R. Rao, S. L. Chaplot, N. Choudhury, S. Ghose, J. M. Hastings, L. M. Corliss and D. L. Price, Phys. Chem. Minerals **16**, 83 (1988); S. L. Chaplot, N. Choudhury, S. Ghose, M. N. Rao and P. Goel, Eur. J. Mineralogy, **14**, 291 (2002).

[68]] J. D. Axe, G. D. Petit, Phys. Rev. 151 676 (1966); T. Livneh, E. Sterer Phys. Rev. B 73 085118 (2006)

[69] C. Dolling, R. Cowley A. D. B. Woods Can. J. Phys. 43 1397 (1965)

[70] M. Idiri, T. Le Bihan. S. Heathman, J. Rebizant, Phys. Rev. B 70, 014113 (2004)

[71] Eugene Yakub, Claudio Ronchi, Dragos Staicu, J. Chemical Physics 127 094508. (2007)

[72] C. R. Catlow, Proc. R. Soc. Lond. A.**353**, 533 (1977)

[73] C. Ronchi, G. J. Hyland, J. of Alloys and Compounds, **213/214**, 159 (1994)

[74] C. Ronchi, M. Sheindlin, M. Musella, G. J. Hyland, J. Applied Phys. **85** 776 (1999)

[75] J. Ralph, G. J. Hyland, J. Phys.: Condens. Matter **132**, 76 (1985)

[76] Hj. Matzke, J. Chem. Soc., Faraday Trans. 2 **83** 1121 (1987)

[77] A. Yamada, H. Koizumi, S. Nishimura, N. Sonoyama, R. Kanno, M Yonemura, T. Nakamura and Y. Kobayahi, Nat. Mater., , **5**, 357 (2006)

[78] A. S. Andersson and J. O Thomas, J. Power Sources, , **97-98,** 498 (2001)

[79] S. Kim, J. Kim, Gwon Hyeokjo and K. Kang, J. Electro. Society, , **156,** A635 (2009)

[80] C. Delacourt , P. Poizot, J. Tarascon and C. Masquelier, Nat. Mat., , **4**, 254 (2005)

[81] D. Morgan, Van der Van and G. Ceder, Electrom. Solid-State Lett., , **7**, A30 (2004)

[82] F. Zhou, C. A. Marianetti, M. Cococcioni, D. Morgan and G. Ceder, Phys. Rev. B, **69**, 201101 (R) (2004)

[83] S Shi, L. Liu, C. Ouyang, D. Wang, Z. Wang, L. Chen and X. Hunag Phys. Rev. B, , **68**, 195108 (2003)

[84] A. Yamada, Y. Kudo and K. Liu, J. Electrochem. Soc., , **148,** A1153 (2001)

[85] F. Zhou, T. Maxisch and G. Ceder, Phys. Rev. Lett., , **97**, 155704 (2006)

[86] M. K. Kinyanjui, P. Axmann, M Wohlfahrt-Mehrens, P. Moreau, F. Boucher and U. Kaiser, J. Phys: Condens. Matter, **22**, 275501 (2010)

[87] L. Wang, F. Zhou, Y. S. Meng and G. Ceder, Phys Rev. B, , **76**, 165435 (2007)

[88] P. Tang and N. A. W. Hozwarth, Phys. Rev. B, , **68**, 165107 (2003)

[89] S. Shi, C. Ouyang, Z. Xiong, L. Liu, Z. Wang, H. Li, D. Wang, L. Chen and Z. Huang, Phys. Rev. B, , **71**, 144404 (2005)

[90] (a) S. P. Ong, V. L. Chevrier and G. Ceder , Phys. Rev. B, , **83**, 075112 (2011); (b)Y. Xu,W. Y. Ching and Y. M. Chiang, J. Appl. Phys., , **95**, 6583 (2004)

[91] C. Ouyang, S. Shi, Z. Wang, X. Huang and L. Chen, Phys. Rev. B, , **69**, 104303 (2004)

[92] T. Maxisch, F. Zhou and G. Ceder, Phys. Rev. B, **73**, 104301 (2006)

[93] Y. Asari, Y. Suwa and T. Hamada, Phys. Rev. B, , **84**, 134113 (2011)

[94] J. Sugiyama, H. Nozaki, M. Harada, K. Kamazawa, Y. Ikedo, Y. Miyake, O. Ofer, M. Mansson, E. J. Ansaldo, K. H. Chow, G. Kobayashi and R. Kanno, Phys. Rev. B, , **85**, 054111 (2012)

[95] J. Sugiyama, H. Nozaki, M. Harada, K. Kamazawa, O. Ofer, M. Mansson, J. H. Brewer, E. J. Ansaldo, K. H. Chow, Y. Ikedo, Y. Miyake, K. Ohishi, I. Watanabe, G. Kobayashi, R. Kanno, Phys. Rev. B, , **84**, 054430 (2011)

[96] P. J. Baker, I. Franke, F. L Pratt., T.Lancaster, D.Prabhakaran, W Hayes and S. J. Blundell, Phys. Rev. B, , **84** 174403 (2011)

[97] S. Nishimura, G.Kobayashi, K.Ohoyama, R.Kanno, M.Yashima and A.Yamada, Nat. Mater., , **7,** 707 (2008)

[98] G.K.P. Dathar, D. Sheppard, K. J. Stevenson and G. Henkelman, Chem. Mater., , **23**, 4032 (2011)

[99] J. Yang and J. S. Tse, J. Phys. Chem. A, , **115**, 13045 (2011)

[100] P. Zhang, Y. Wu, D. Zhang, Q. Xu, J. Liu, X. Ren, Z. Luo, M. Wang and w. Hong, J. Phys. Chem. A, , **112**, 5406 (2008)

[101] R. Stevens,, J. L. Dodd, M. G. Kresch, R. Yazami, and B. Fultz B. Ellis and L. F. Nazar J. Phys. Chem. B**, 110**, 22732 (2006)

[102] (a) S. L. Shang, Y.Wang, Z. G.Mei, X. D.Hui and Z. K.Liu, Journal of Mater. Chem., , **22**, 1142 (2012); (b) S Shi, H.Zhang, X. M. Ke, C.Ouyang, M.Lei and Li. Chen, Phy. Lett. A, , **373,** 4096 (2009)

[103] W.Paraguassu, P. T. C.Freire, V. Lemos, S. M.Lala, L. A.Montoro and J. M.Rosolen, J. Raman Spectrosc., **36,** 213 (2005)

[104] K. P. Korona, J.Paperska, M.Kaminska, A.Witowski, M.Michalska and L.Lipinska, Mat. Chem. and Phys., , **127,** 391 (2011)

[105] T Maxisch and G.Ceder, Phys. Rev. B, **, 73**, 174112 (2006)

[106] A. Hunt, W. Y. Ching, Y. M. Chiang and A. Moewes, Phys. Rev. B, , **73**, 205120 (2006)

[107] S.Geller and J. L.Durand, Acta Cryst., **13,** 325 (1960)

[108] R. P. Santaro and R. E. Newnham, Acta Cryst., **22**, 344 (1967)

[109] J. Li, V. O. Garlea, J. L. Zarestky and D. Vaknin, Phys. Rev. B, , **73**, 024410 (2006)

[110] G. Liang, K. Park, J. Li, R. E. Benson, D. Vaknin, J. T. Markert and M. C. Croft, Phys. Rev. B, , **77**, 064414 (2008)

[111] J. Li, W. Tian, Y. Chen, J. L. Zarestky, J. W. Lynn and D. Vaknin, Phys. Rev. B, , **79**, 144410 (2009)

[112] D. Aron, A. Zorko, R. Dominko and Z. Jaglicic, J. Phys: Condens. Matt., , **16**, 5531 (2004)

[113] C. Wang and J. Hong, Electrochem. Solid-State lett., , **10,** A65 (2007)

[14] B. Wu, Y. Ren, D. Mu, C. Zhang, X. Liu and F. Wu, Int. J. Electrochem. Sci., **8**, 8502 (2013)

[115] M. M. Doeff, Y. Hu, F. McLarnon and R. Kosteckib, electrochemical and Solid-state Lett;, , **10**, A207 (2003)

[116] B. Delacourt, P. Poizot, S. Levasseur and C. Masqueliera, Electrochemical and Solid-State Letters, **9**, A352 (2006)

[117] C. K. Park, S. B. Park, H. C. Shin, W. I. Cho and H. Jang, Bull. Korean Chem. Soc., **32**, 191 (2011)

[118] J. M. Tarascon, C. Delacourt, A. S. Prakash, M. Morcrette, M. S. Hegde, C. Wurm and C. Masquelier, Dalton Trans., , P2988 (2004)

[119]J. Lee, S. J. Pennycook and S. T. Pantelides., Appld. Phys. Lett., , **101**, 033901 (2012)

[120]H. Shao, Solid State Commun., **150**, 81 (2010)

[121] C. R. Sides, F. Croce, V. Y. Young, C. R. Martin and B. Scrosatic, Elec. Solid-St. Lett., , **8**, A484 (2005)

[122] A. V. Churikov, A. V. Ivnishchev, I. A. Ivanishcheva, V. O. Sycheva, N. R. Khasanova, E. V. Antipov, Electrochim. Acta, , **55**, 2939 (2010)

[123] K.Tang, X.Yu, J.Sun, H.Li, X.Huang, Electrochim. Acta, ,**56,** 4869 (2011)

[124] P. P. Posini, M. Lisi, D. Zane, M. Pasquali, Solid-State. Ion., , **148**, 45 (2002)

[125] M. S.Islam, D. J.Driscoll, C. A. J. fisher and P. R.Slater, Chem Mater., , **17**, 5085. (2005)

[126] S.Chung, S.Choi, T.Yamamoto and Y. Ikuhara, Phy. Rev. Lett., , **100**, 125502. (2008)

[127] S.Chung, S. Choi, S. Lee and Y.Ikuhara, Phys. Rev. Lett., ,**108**, 195501 (2012)

[128] (a) J. M. Carpenter and D. L. Price, Phys. Rev. Lett., , **54**, 441 (1985) (b) A. Sjolander, Arkiv fur Fysik, , **14**, 315 (1958)

Chapter 3

Lattice dynamics and Born instability in Yttrium Aluminum Garnet (YAG), $Y_3A1_5O_{12}$ and Rare Eath Doped Aluminum Garnets

3.1 INTRODUCTION

Yttrium Aluminum Garnet ($Y_3Al_5O_{12}$) is an important solid-state laser host [1,2] material. Nd doped YAG has wide spread use in commercial, medical, military and industrial applications. A combination of ideal spectroscopic properties of the rare-earth ions in YAG crystal, low thermal expansion, high-optical transparency, low acoustic loss, high threshold for optical damage, hardness, stability against chemical and mechanical changes make it the most widely used laser material [3-10]. They are hard, stable, isotropic and their large thermal conductivities permit laser operation at high power levels. Being one of the most creep resistant [9] oxides, it finds application in high-temperature ceramic composites [11]. Various doped YAG materials have been proposed as optical pressure sensors upto very high pressures of the order of 180 GPa [12,13]. Garnets find use as geobarometers [14,15], form a part of mantle transition region in the pressure range between 10-25 GPa [16,17]. Rare earth $Yb_3Al_5O_{12}$ garnet is a synthetic insulator, plays an important role as host crystals for near-infrared soli-state lasers [36]. $Lu_3Al_5O_{12}$ doped with Ce^{3+} is a promising scintillator material with high density and a fast response time [36].

Owing to its numerous practical applications, a thorough understanding of the vibrational properties and high-temperature, high-pressure behavior becomes vital. Several studies with the aim of understanding the influence of defects due to doping have already been carried out [18-26]. Better understanding of the parent compound would throw insights into the changes occurring in the solid-state properties of the crystal on doping. This information would further help in improving the usefulness of the doped YAG systems that find varied technological applications. Various workers have reported experimental X-ray and neutron diffraction [27-29], Brillouin scattering and ultrasonic studies [30,31], Raman [32] and infrared spectroscopy [5,30-33], measurements of the specific heat [34] and thermal expansion [35] of YAG. Theoretical studies of the electronic structure of pure garnets [3,8,10], and symmetry based studies on the vibrational properties of several rare-earth garnets [36-41] have also been reported.

The behavior of garnets under pressure has always been a subject of interest. Many garnets like Fe-rich YIG [42], Gallium Garnet (GGG) [28] *etc* are found to undergo pressure induced amorphization. But experimental studies indicate that YAG based materials are stable under fairly high pressures as high as 180 GPa [12]. It is found to be thermally stable up to high temperatures [34,35] as well. Pressure induced amorphization has been studied in a number of model systems like α–quartz, ice *etc* and it has been observed that the onset of pressure induced amorphization coincides with zone boundary phonon softening and elastic instabilities [43,44].

A comprehensive lattice dynamics study of pristine YAG, aimed at understanding its vibrational spectra, elasticity and thermodynamical properties at high pressure and temperature has been scarce. This work reports an extensive study on the structure, vibrational and thermodynamic properties of YAG, in detail and elastic stability of rare-earth garnets. The author has calculated the pressure dependence of phonon frequencies in the whole Brillouin Zone. Such extensive calculations of the phonon dispersion relation in the various symmetry directions, phonon density of states and thermodynamic properties of

YAG has not been reported till now. All reported ab initio works [45-56] on various garnet structured materials, including YAG, have mainly been restricted to structural and electronic properties. There are only a few studies [49,53-56] on phonons and due to the complex structures involved, these workers report calculations of only the long wavelength phonons, *i.e.*, at the zone centre. There is no reported high pressure *ab initio* studies on the dynamics and elastic properties of YAG. This work is an effort to understand the basic phonon related properties in pure YAG.

Microscopic understanding of the thermodynamic, high-pressure properties of these garnets is essential for the quantitative understanding of its variety of properties. Accurate characterization of the structural, vibrational and thermodynamic properties is essential for understanding the physics involving these garnets. These studies are fairly involved as these garnets have complex crystal structures with a large number of atoms in the primitive cell. The crystal structure has been calculated along with the elastic constants, and density of states. Thermodynamic properties including the equation of state, specific heat and thermal expansion have also been computed. The aim in the study has been to model the ambient phase, extrapolate the model calculations to high pressure and temperature, search for dynamical instabilities, and understand the changes occurring in the bonding with increasing pressure and temperature. The response the of the various Raman active frequencies to pressure has been elucidated.

3.2. THEORETICAL CALCULATIONS

The general garnet crystal has a chemical formula $A_3B'_2B''_3O_{12}$, space group *Ia3d* [27] as shown in Fig.3.1. The cubic cell contains eight formula units with the metal ions occupying different symmetry sites. The structure can be viewed as interconnected dodecahedrons (at the A site), octahedrons (at the B' site) and tetrahedrons (at the B" site) with shared O atoms at the corners of the polyhedra. Each oxygen atom is a member of two dodecahedra, one octahedron and one tetrahedron. There are three main classes of synthetic garnets based on the atomic species at the B" sites. They are the aluminum garnets, iron garnet and gallium garnets. In case of YAG, the B' and B" sites are both occupied by the same element (aluminum) in different valence states. These have a complex structure with 80 atoms/primitive cell.

Lattice dynamics calculations of the equation of state and vibrational properties may be undertaken using either a quantum-mechanical *ab initio* approach or an atomistic approach involving semi empirical interatomic potential. Owing to the structural complexity of garnets (80 atoms/primitive cell), the author has used an atomistic approach. The interatomic potential consists of Coulombic and short-ranged Born Mayer type interactions along with a van der Waals interaction term (only between the oxygen atoms) as explained in equation (1.25) in chapter 1. The parameters used in this study have been adjusted to satisfy the conditions of static and dynamical equilibrium. The effective charge and radius parameters used in the calculations are given in Table 3.1.

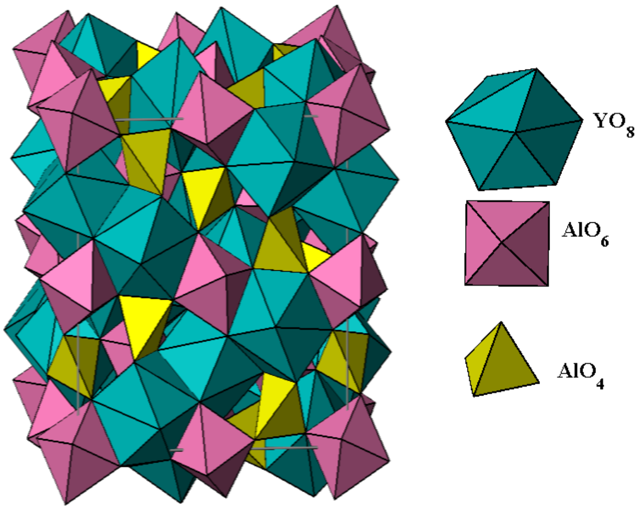

Fig. 3.1. *Polyhedral representations of the crystal structure of YAG.*

The van der Waals interaction terms have been introduced only between the oxygen atoms with C=100 eVÅ^6. The polarizability [60,61] of the oxygen atoms has been introduced in the framework of the shell model with the shell charge $Y(O)$= -2.00 and shell-core force constant $K(O)$=110 eVÅ^{-2}.

The equilibrium crystal structure of YAG has been calculated by minimizing the Gibbs free energy at T=0 K with respect to the lattice parameters and the atomic positions. Since the structural energy minimization was done at T=0 K, the vibrational contribution was not included to derive the structure as a function of pressure. A small contribution expected from the quantum mechanical zero-point vibrations has been ignored. The good agreement between calculated and experimental pressure variation of Raman modes up to 20 GPa and equation of state up to 100 GPa (as discussed later) indicates that our model is valid at high pressures.

Table 3.1: *Model parameters (Al (1) and Al(2) are in the octahedral and tetrahedral positions respectively).*

	Al (1)	Al (2)	O	Y
Z	1.7	2.556	-1.5475	2.5
R(Å)	1.3	1.05	1.89	2.0

3.3 RESULTS AND DISCUSSIONS

3.3.1 Crystal structure and elastic constants of YAG

The computed garnet crystal structure is found to be in unison with experimental findings [27]. The calculated lattice constant and the fractional coordinates are found to be in good agreement with reported data as can be seen from Table 3.2. The elastic constants have been calculated from the slopes of the acoustic phonon branches, and bulk modulus has been calculated analytically using the elastic constant values. The pressure derivative B' has been obtained numerically using the values of bulk modulus at different pressures.

Numerical values of elastic constants for a cubic crystal are determined by the values of acoustic mode frequencies near zone center along <100>, <110> crystallographic directions. Along <100> the longitudinal acoustic mode yields C_{11}, while the transverse mode gives C_{44}. The value $0.5(C_{11}-C_{12})$ is given by the transverse mode along <110> (with polarization along $<\bar{1}10>$ direction). The calculated elastic constants and bulk modulus are found to be comparable with reported values as shown in Table 3.3 [30,31,3,8]. C_{11} is the largest while C_{12} and C_{44} are comparable as is generally found in most cubic crystals. The variation of elastic constants with pressure is plotted in Fig. 3.2. C_{11} and C_{12} vary linearly with pressure while C_{44} remains almost unchanged. Bulk modulus at 100 GPa is 556 GPa, which is about thrice its value at ambient pressure, so it becomes very hard compared to the ambient phase.

Stablity of a lattice is central to understanding its structural response to change in physical conditions. Born criteria deals with systematic study of crystal stability in the unstressed conditions. The criteria are namely, $C_{11}+2C_{12}>0$; $C_{44}>0$ and $C_{11}-C_{12}>0$, where C_{ij} are the conventional elastic constants [62a,b,c,]. There are several definitions for elastic constants at high pressure. For cubic crystals the relevant elastic constants under hydrostatic pressure that define the Born stability criteria are $c_{11} = C_{11}-P$, $c_{12} = C_{12}+P$ and $c_{44}=C_{44}-P$, where C_{11}, C_{12} and C_{44} are the elastic constant values derived from the slopes of the acoustic phonon branches. For cubic crystals, under hydrostatic loading, the mechanical Born stability criteria [62] leads to $c_{11}+2c_{12}>0$, $c_{11}-c_{12}>0$ and $c_{44}>0$. For the system to be mechanically stable, all these three conditions given above must be simultaneously satisfied. The Born stability criteria that is violated in the present case is that the parameter $c_{44} = C_{44} - P$ should be positive. This implies that the crystal loses its resistance to shear deformation. This violation is found in the calculation at P above 108 GPa. Although C_{44} itself remains positive, the value of the pressure derivative of the elastic constant C_{44} is less than 1 as per our calculations; as a result the parameter $c_{44} = C_{44} - P$, is very close to zero at 100 GPa and becomes negative beyond 108 GPa. Fig. 3.2 gives c_{11}, c_{12} and c_{44} for YAG under pressure; it can be see that c_{44} becomes negative around 108 GPa. Reported experimental [12] energy dispersive X-ray diffraction data suggests that long range crystalline order is lost beyond 100 GPa in Sm-doped YAG.

The pressure derivates of the computed elastic constants have been compared in Table 3.4 with those reported by Saunders [29] (calculated using a atomistic model) *et al* and with experimental (ultrasonic wave velocity measurements up to 0.15 GPa) results of Yogurtcu [31] *et al*. Our calculations are in good agreement with experimental values as well as with the previous calculations by Saunders *et al* (those obtained with 90% ionicity).

3.3.2 Long wavelength phonon frequencies of YAG

Corresponding to the 80 atoms in the garnet primitive cell, a total of 240 phonon modes occur at every wave vector. Group theoretical symmetry analysis was undertaken to classify the phonon modes belonging to various representations. Because of the selection rules only phonon modes belonging to certain group theoretical representations are active in typical single crystal Raman, infrared and inelastic neutron scattering measurements. These selection rules are governed by the symmetry of the system and the scattering geometry employed. The theoretical scheme for the derivation of the symmetry vectors is based on Irreducible Multiplier Representations [63-65] involving construction of symmetry adapted vectors, which are used for block diagonalizing the dynamical matrix. This enables the assignment of the phonon modes belonging to various representations, and direct comparison with observed single crystal Raman and infrared data.

Table 3.2: *Comparison of calculated (ambient as well as high pressure) structural parameters and average bond lengths with reported experimental and ab initio data under ambient conditions. For the space group Ia3d, the Y, Al(1), Al(2), and O atoms are located at Wyckoff positions 24(c)(0, 0.25, 0.125), 24(d) (0, 0, 0), 16(a) (0.375, 0, 0.25) and 96(h) (u,v,w) respectively.*

P (GPa)	0 Experimental [27] (ambient)	0 (*ab-initio* [3,8,9])	0	50	110
Lattice parameter, a (Å)	12.0	11.904	11.96	11.24	10.78
u	0.9694		0.96	0.959	0.959
v	0.0512		0.047	0.054	0.056
w	0.15		0.16	0.159	0.157
Y-O (Å)	2.3675	2.37	2.36	2.24	2.15
Al(1)-O , Al(2)-O (Å)	1.937, 1.761	1.94, 1.76	1.94, 1.76	1.94,1.52	1.85, 1.48

Table 3.3: *Comparison of elastic and Gruneisen parameter data. B and B' are the bulk modulus and its pressure derivative respectively.*

	Experimental	Calculated (This work)	Calculated (*ab initio* [3,8])
C_{11}(GPa)	328 [a], 339 [b]	329	
C_{12}(GPa)	106 [a], 114 [b]	103	
C_{44}(GPa)	114 [a], 116 [b]	90	
B (GPa)	185 [b], 189 [c], 220 [d]	178	220.7
$B^{'}$	-	4.1	4.12
γ^{th}	1.43 [a]	1.45	

[a] : Reference 31; [b]: Reference 30; [c]: Reference 33; [d]: Reference 5.

Table 3.4: *Comparison of our results with those of Saunders [29] et al and with reported experiment [31]*. (a: 90% ionicity; b: 100% iconicity)

	Lattice Parameter (Å)	C_{11} (GPa)	C_{12} (GPa)	C_{44} (GPa)	B (GPa)	γth	γ^{el}	$\partial C_{11}/\partial P$	$\partial C_{12}/\partial P$	$\partial C_{44}/\partial P$	$\partial B/\partial P$
Saunders [a] *et al*	11.93	325	102.7	103	177	0.9	0.73	6.3	2.5	0.19	3.76
Saunders [b] *et al*	11.93	401	127	127	218	0.9	0.73	6.3	2.5	0.19	3.75
Yogurtcu [31] *et al*	12.0	328	106	114	180	1.43	0.727	6.31	3.51	0.62	4.42
This work	11.96	329	103	90	178	1.45	1.1	4.6	3.4	0.16	3.8

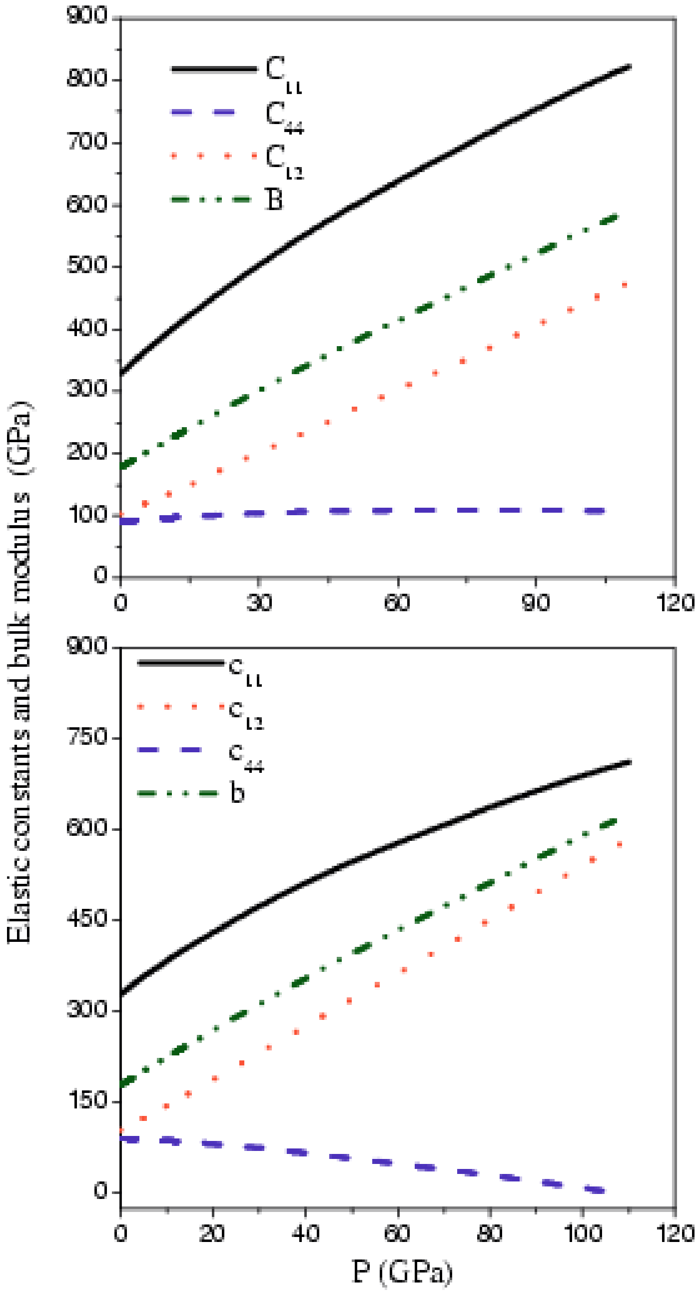

Fig. 3.2. *Pressure dependence of elastic constants and bulk modulus of YAG. For cubic crystals the relevant elastic constants under hydrostatic pressure that define the Born stability criteria are* $c_{11} = C_{11} - P$, $c_{12} = C_{12} + P$ *and* $c_{44} = C_{44} - P$, *where* C_{11}, C_{12} *and* C_{44} *are the elastic constant values derived from the slopes of the acoustic phonon branches.*

At the zone center, the phonon modes are classified into the following irreducible representations:

$$\Gamma : 3A_{1g} + 5A_{2g} + 5A_{2u} + 5A_{1u} + 8E_g + 14T_{2g} + 14T_{1g} + 10E_u + 18T_{1u} + 16T_{2u}$$

The $3A_{1g}$, $8E_g$ and $14T_{2g}$ are Raman active while $18T_{1u}$ modes are infrared active. The E modes are doubly degenerate while the T modes are triply degenerate. These modes have been experimentally [5,32] measured and they compare (Table 3.5) very well with our calculated values. However, there are no *ab initio* calculations of the long-wavelength phonons for comparison. The calculated phonon frequencies with mode assignments are compared with the available Raman and infrared data [5,32] in Fig. 3.3. Hurrell [32] *et al* have measured 15 of the IR modes using near-normal reflection method. Hofmeister [5] *et al* have measured all the modes through a combination of reflection and absorption spectroscopy. The static ε_o, and high-frequency ε_∞, dielectric constants are related to the infrared frequencies through the Lyddane Sachs-Teller (LST) relation:

$$\prod_i \left(\frac{\nu_i(LO)}{\nu_i(TO)}\right)^2 = \frac{\varepsilon_o}{\varepsilon_\infty} \qquad (1)$$

The experimental value for YAG is 3.2 (Ref [5] and references therein); value calculated by Hurrell [32] *et al* using their measured frequencies is 3.96, while the one calculated by Hofmeister is 3.27. Our calculated value is 3.46. There appears to be no band gaps in the frequency spectrum. Both the experimental studies as well as the calculations support this observation. This is against the general trend found in aluminosilicate garnets [14,15], which show a band gap in the 650-800 cm^{-1} frequency range. The low energy modes are in very good agreement with experimental data. However, at the higher frequency region, the calculated values seem to be slightly different from experimental data. Our results are closer to Hofmeister [5] with a deviation of about 5%. As discussed above the Born instability criteria are related to the acoustic phonons at low frequencies only and so would not be affected. This would marginally affect the calculation of various

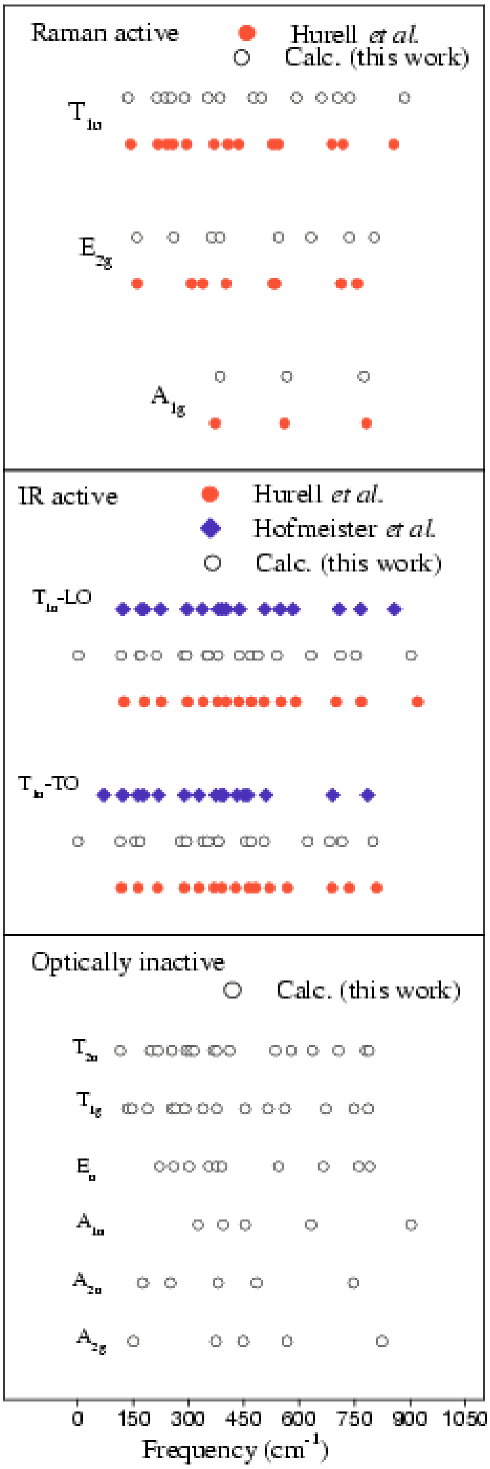

Fig.3.3. *Phonon frequencies at zone centre compared with available experimental optical data [5,32].*

thermodynamic properties (given below) like specific heat at high temperatures only. The group theoretical classification in the three symmetry directions is as given below:

[010]: $29\Sigma_1 + 29\Sigma_2 + 29\Sigma_3 + 29\Sigma_4 + 124\Sigma_5$

[111]: $40\Lambda_1 + 40\,\Lambda_2 + 160\,\Lambda_3$

[110]: $59\Delta_1 + 59\Delta_2 + 61\Delta_3 + 61\Delta_4$

Table 3.5: *Comparison between experimental [41] and calculated Raman active frequencies.*

	$\omega_{i\ (exp)}$	$\omega_{i\ (cal)}$	$(\gamma_i)_{exp}$	$(\gamma_i)_{cal}$
T_{2g}	145	137	2.4	2.1
	220	214	1.6	2.0
	243	239	1.8	1.1
	261	254	1.1	1.4
	295	289	1.5	1.0
	372	353	1.6	0.8
	406	386	1.0	1.1
	-	477		0.4
	438	499	0.8	0.5
	545	594	0.8	0.6
	-	661		0.4
	691	705	1.4	0.8
	718	738	1.3	0.8
	857	886	1.0	0.5
E_{2g}	163	161	0.7	0.6
	310	261	1.6	1.3
	340	360	1.5	0.9
	402	386	1.1	1.0
	536	545	0.7	0.4
	-	633		0.3
	712	736	1.1	0.6
	754	803	1.3	0.7
A_{1g}	370	387	0.8	1.1
	559	569	0.8	0.5
	783	776	0.9	0.5

The calculated phonon dispersion relations in the high symmetry directions in the low energy range up to 20 meV, at P = 0 and 100 GPa, are shown in Fig. 3.4. It can be seen that many branches have hardened with pressure. There are no significant changes in any of the branches which might indicate a definite softening in any of the low energy branches. There is also no optic mode softening.

The calculated pressure dependence of phonon spectra, at ambient pressure, is used for the calculation of the Grüneisen parameter Γ(E), averaged for all phonons of energy E. The variation in the values of the Gruneisen values for all the modes is shown in Fig. 3.5. .

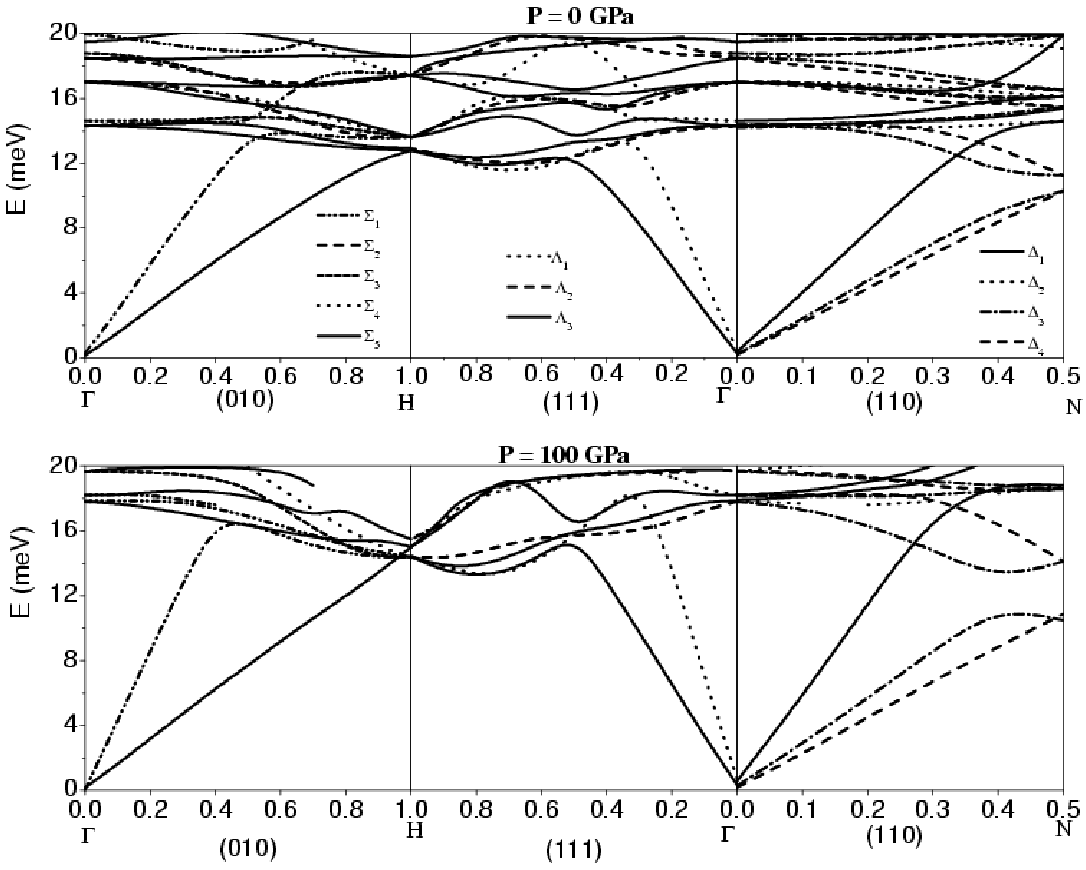
P = 0 GPa

P = 100 GPa

Fig.3.4. Phonon dispersion relation along the three high symmetry directions in the low energy range up to 20 meV at P = 0 and 100 GPa.

The energy of the modes can be divided into three groups, group I between 0 and 30 meV, group II corresponding to modes between 30 and 60 meV and group III for the modes > 60 the modes below 30 meV exhibit high values of Γ, with an average around 1.5; the average Γ of group II is around 1 and that of group III is 0.5.

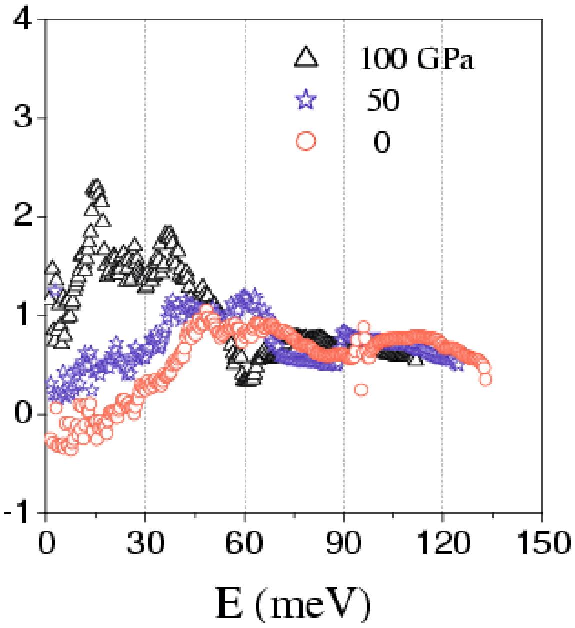

Fig.3.5. *Variation in the calculated mode Gruneisen parameters at various pressures. meV.*

3.3.3 Phonon density of states, partial density of states and thermodynamic properties of YAG

The calculated total and partial phonon density of states are shown in Fig. 3.6. Solid line gives the density of states at ambient conditions. The dynamical contributions from the various species reveal seperations in their spectral range. Yttrium atom contributes solely in the low energy region between 0 to 40 meV, with a miniscule contribution around 50 meV. Aluminum atoms with different co-ordinations contribute differently. Aluminum in the octahedral coordination contributes mainly between 30 to 70 meV, while the one in tetrahedral coordination contributes almost in the entire energy range, with a greater contribution on the higher energy end between 80 and 120 meV. Oxygen atoms contribute in the whole region from 0 to 120 meV. While the Al-O tetrahedral bond length is 1.76 Å, the Al-O octahedral bond length is 1.9 Å. These give rise to differences in their bonding characteristics and vibrational spectra. Modes in the intermediate region are owing to a complex combination of vibrations involving all the polyhedra of Al and Y.

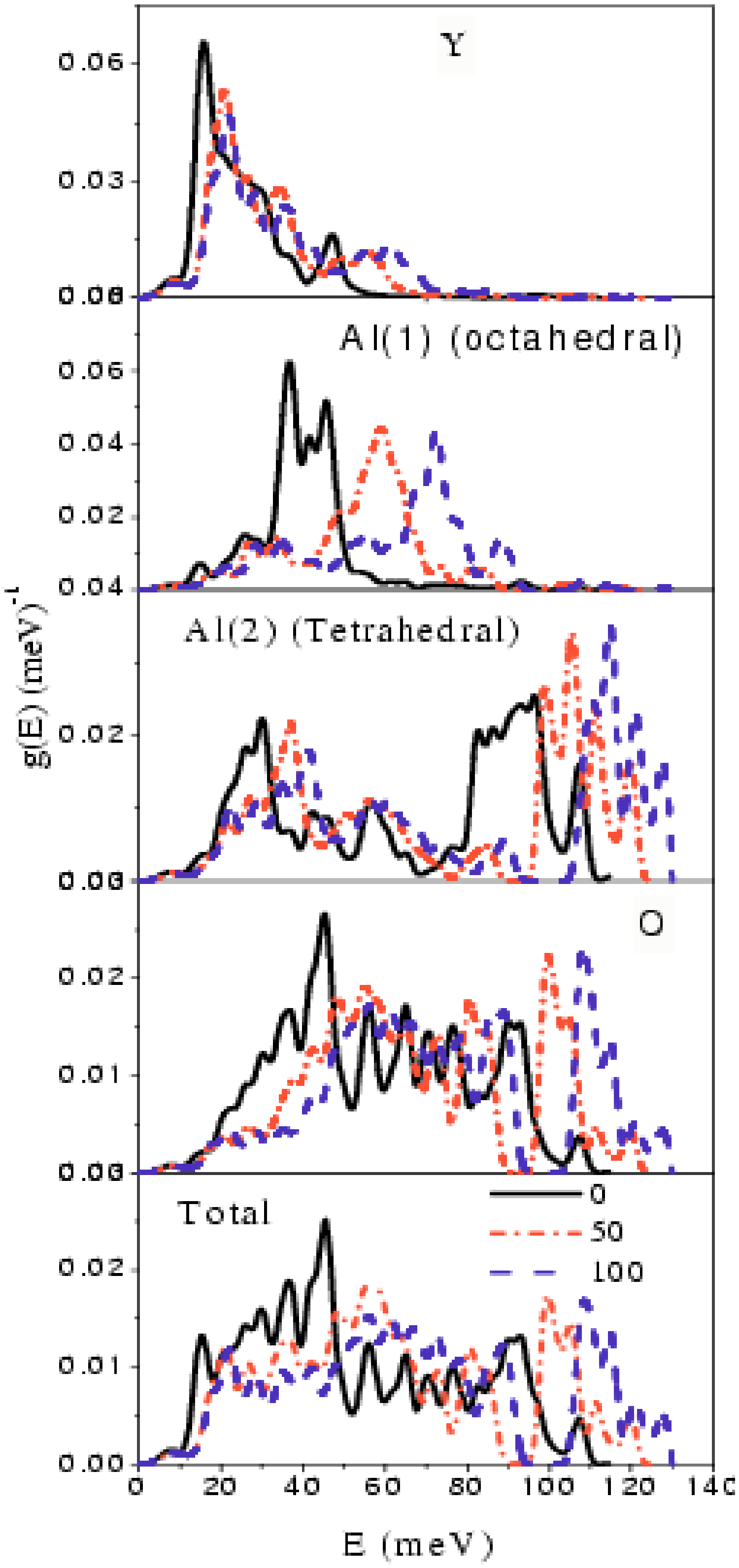

Fig. 3.6. *Total and partial phonon densities of state in YAG at P=0, 50 and 100 GPa*

The computed one-phonon density of states, have been used for the calculation of volume-dependent thermal expansion coefficient, specific heat and other thermodynamic properties. The calculated thermal expansion coefficient and specific heat has been shown in Fig. 3.7(a) and (b) respectively. Calculated specific is in excellent agreement reported with experimental data [34] as given in Fig 3.7(b). The difference $C_p(T) - C_v(T)\,(=[\alpha_v(T)]^2 BVT)$ becomes significant at high temperatures and is about 5% in YAG.

Thermal expansion of a crystal arises from the anharmonicity of interatomic binding forces. A measure of anharmonicity [31] is given by a parameter called $\gamma^{thermal}$ which is given as:

$$\gamma^{thermal} = \beta V B^s / C_P \qquad (2)$$

where, V is the atomic volume, B^s is the adiabatic bulk modulus, β and C_P are the volume thermal expansion coefficient and specific heat at room temperature. Our calculations yield a value of 1.45 for $\gamma^{thermal}$, which is in excellent agreement with reported [31] value of 1.43. The response of the crystal volume to temperature has been compared with experimental data [35] in Fig. 3.8.

The calculations have been done in the quasiharmonic approximation. The agreement is very good up to high temperatures of 1500 K (melting point for YAG is 2213 K). Thus, the percentage relative volume expansion is in excellent agreement with the reported experimental findings.

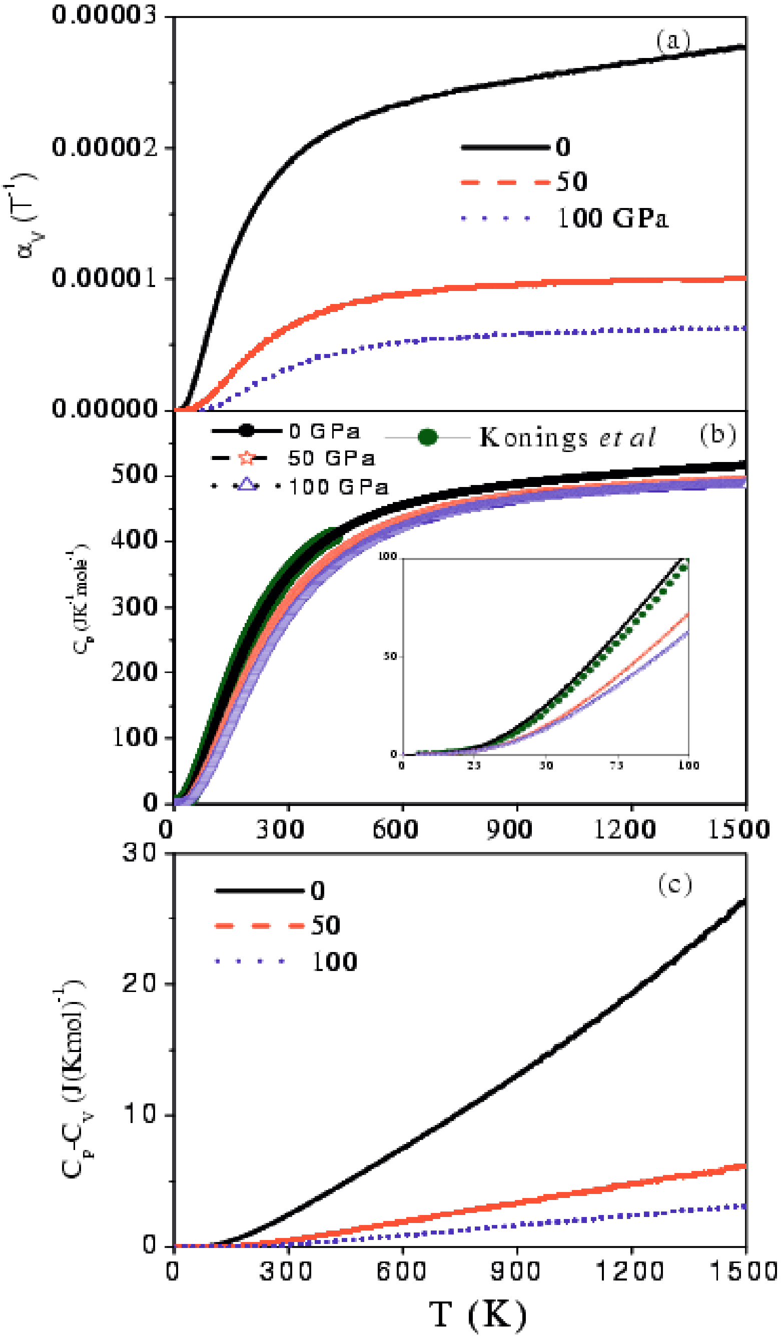

Fig. 3.7. *(a) Calculated volume thermal expansion coefficient (α_V) at different pressures. (b) Calculated specific heat at ambient condition in comparison with reported experimental (Konings et al) data [34]. Calculated specific heat at different high pressure has also been plotted for comparison. The inset gives the low temperature specific heat at various pressures. (c). Correction, C_P-C_V due to implicit effects at various pressures.*

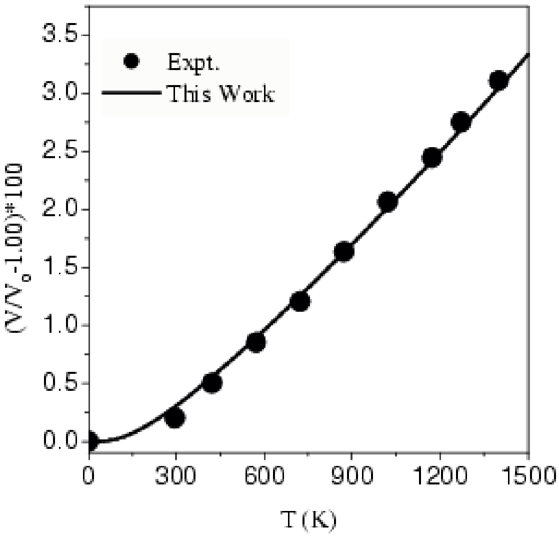

Fig. 3.8. *Thermal expansion of YAG in comparison with reported experimental (Geller et al) data [35]*

3.3.4. High pressure studies on YAG

The behavior of the 25 Raman modes ($3A_{1g} + 8\ E_g + 14\ T_{2g}$) under pressure have been studied and compared with reported data in Fig. 3.9. Majority of the experimental Gruneisen parameters vary between 0.6-1.7 while the calculated values lie between 0.5-1.7. Only the lowest T_{2g} mode at 145 cm^{-1} has an experimental Gruneisen value of 2.4 whose corresponding calculated value is 2.1. The narrow range of these values show that the vibrational anharmonicity is similar for most optical phonons in the system.

Structural response of the garnet to increase in pressure has been derived as in Fig 3.10. YAG is reported to be a stable system [28] and is supposed to retain its cubic phase even beyond 100 GPa [28,12]. The equation of state in YAG has been compared in Fig.3. 9 with reported [28] data from synchrotron XRD experiments on Nd doped YAG. Doping in rare earth garnets is generally of the order of 1%. Elastic constants are observed to have negligible dependence on such small doping levels [28b]. Hence C_{44} of doped YAG [27] would be very close to that of pure YAG. The values of B_o and B'

obtained from reported data using Birch-Murughan equation are 383 GPa and 1.77 GPa. These values are very different from the ones obtained by other experimental reported data and our calculations. Experimental [28] equation of state suggests that a compression of ~23% is obtained at 100 GPa, while at the same pressure the compression is 25% as per our calculations.

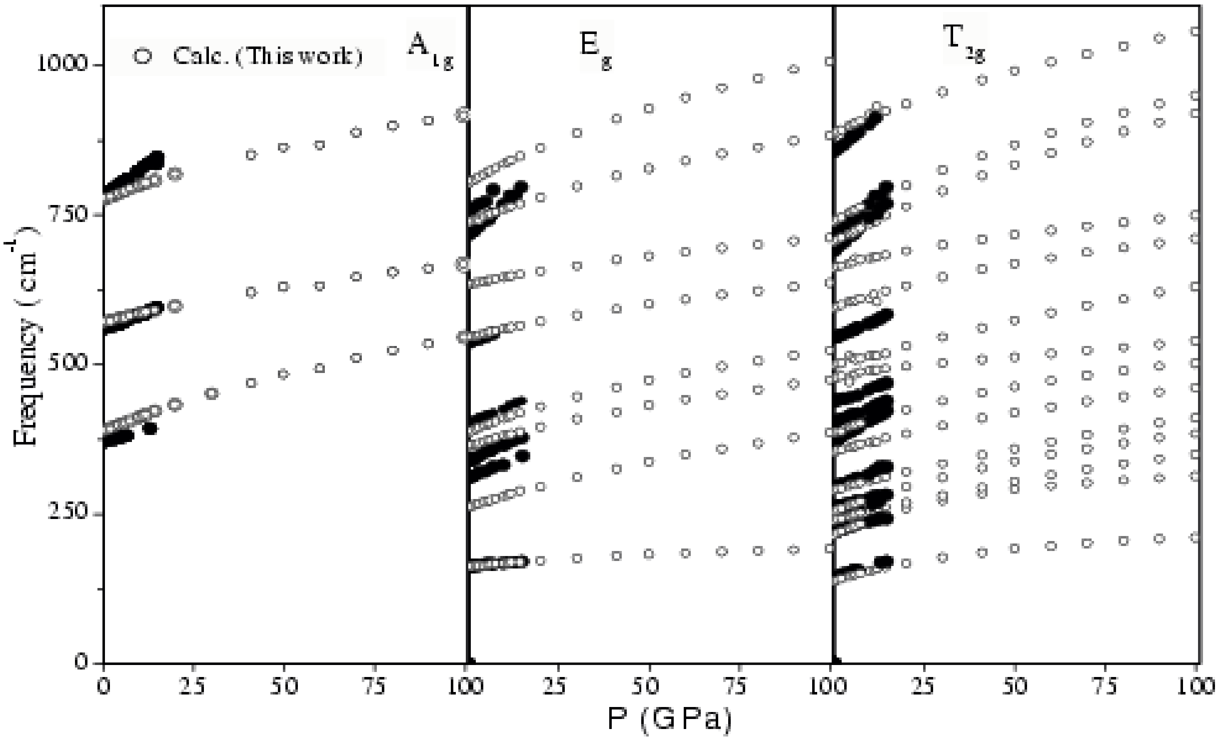

Fig. 3.9. *Pressure dependence of Raman modes in comparison with reported data. Open symbols are calculated values, while solid symbols [41] are reported experimental (Aravantidis et al) values.*

At ambient conditions, there is no band gap in the phonon density of states of YAG as seen in Fig. 3.6. The density of states of various atoms at P = 50 and 100 GPa have been plotted in Fig.3.6. With increasing pressure, the low frequency density of states of the Y atom is significantly reduced and the peaks are shifted to higher energies. There is a shift of about 15-20 meV at P = 50 GPa as compared with P=0

GPa. The YO_8 polyhedra experiences maximum compression between 0 and 50 GPa, thereafter it seems that the polyhedra are not as much compressible. Therefore the Y-PDOS does not change much between 50 and 100 GPa. The partial density of states of Al, in both octahedral and tetrahedral sites is also significantly altered at high pressure, and they seem to change continuously between 0 and 100 GPa. The O-PDOS also changes considerably with pressure, the peak around 40 meV reduces and the peak beyond 80 meV gains intensity with increasing pressure. The total density of states show a band gap between 90-100 meV at P=50 GPa while the gap widens further upto 110 meV at 100 GPa.

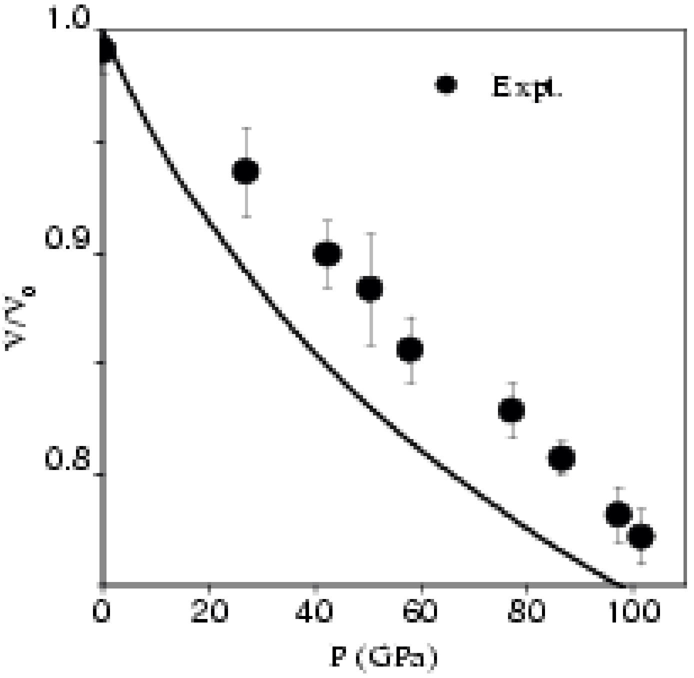

***Fig.3.10**. Equation of state of YAG (calculated results (full line) compared to reported experimental (Hua et al) data [28] (solid circles)).*

The pressure dependence of mode Gruneisen parameters under different pressure has been plotted along with those at 0 GPa in Fig. 3.5. At 50 GPa, the average value between 0-30 meV is 0.5, between 30-60 meV it is 1 and beyond 60 most of the modes have a value around 0.5. At 100 GPa, the average value for modes between 0-30 meV is -0.25, between 30-60 meV, the average value is around 0, while for modes > 60 meV the average value is around 0.75.

We can deduce that the maximum change seems to have occurred in the lowest values energy modes below 30 meV, with some perceptible changes occurring in the highest energy modes. These modes mainly correspond to the YO_8 modes, and to the AlO_4 polyhedra. Thus this figure helps us to understand the microscopic scenario at these pressures. These changes in the vibrational spectra have an important bearing on its high pressure and high temperature properties. Our studies indicate significant atomic rearrangements in the AlO_6 and AlO_4 polyhedra, as well as the YO_8 dodecahedra. The opening of the phonon band gap between 90-110 meV at 100 GPa is due to the Al(2)-O stretching vibrations shifting to higher energies.

Table 3.2 gives the structural parameters and the bond lengths at various pressures. The average bond lengths of the Y-O, Al(1)-O and Al(2)-O bonds have changed with increasing pressure. There are subtle readjustments and reorientations of the various polyhedral units.

The volume dependent thermal expansion coefficient, specific heat and the correction, C_P-C_V of YAG at high pressures have also been computed and compared with ambient phase values in Fig. 3.7. The ambient phase has the maximum thermal expansion coefficient. The correction, C_P-C_V (due to volume dependent anharmonic effects) is maximum for the ambient phase, and it decreases with increasing pressures. Thus, the specific heat decreases with increasing pressure. At lower temperatures below 100 K, the ambient phase has a higher specific heat, almost 1.5 times compared to that at 100 GPa.

These results are consistent with the variations observed in the values of the mode Gruneisen constants.

In this work, we have provided an atomic level understanding of the macroscopic vibrational and thermodynamic properties of high pressure YAG, which have not been studied in detail earlier. Our studies indicate that YAG structure is mechanically unstable at high pressures, due to violations of the Born stability criteria. Aluminosilicate garnets which are principal components of earth's mantle, are known to transform into an oxide phase along with chemical decomposition typically around 25-30 GPa [16]. Due to large kinetic hindrances, such a transformation has not been observed in YAG. Various previous works indicate that YAG may persist metastably up to high pressures of 180 GPa [12], while some of its diffraction peak [12] vanish between 100 -150 GPa [12]. The exact transition has not been observed experimentally so far, although high pressure diffraction experiments [12] indicate a disordered phase above P=100 GPa.

Our theoretical calculations indicate that various polyhedral units contribute differently in different pressure regimes in YAG. There are significant changes in the phonon density of states with increasing pressure. Significant atomic rearrangements take place in the different polyhedral units as can be seen from their bond lengths and bond angles. While at ambient pressure, the YO_8 dodecahedra strongly influences the elastic and thermodynamic properties, at higher pressures, the YO_8, AlO_6 and AlO_4 polyhedra continuously deform with pressure giving rise to important manifestations in their elastic, vibrational and thermodynamic properties. We do not observe optical phonon softening upto fairly high pressures like 100 GPa. YAG however becomes mechanically unstable around 108 GPa (section 3.3.1) due to violation of the Born stability criteria. The c_{44} elastic constant involving a transverse acoustic phonon becomes soft under hydrostatic loading of 108 GPa and the structure becomes elastically unstable. This pressure is an upper bound for YAG retaining even a metastable garnet phase and a certain structural phase transition is indicated above this pressure although free energy crossover to a thermodynamically favorable phase at a lower pressure is not ruled out.

Under high pressures and temperatures, it is expected that cubic YAG would decompose into $3YAlO_3 + Al_2O_3$. Due to the large volume collapse of the perovskite structure, which is typically around 20% lower than the garnet volume, the PdV term would lower the free energy of the perovskite phase. The perovskite phase could thus remain the favored high pressure phase due to its dense atomic packing. However, due to the intrinsic complexity in dealing with chemical decomposition involved in this transition, theoretical studies of the exact pressure for such a garnet to perovskite crossover have not been undertaken for YAG.

High pressure YAG is significantly harder than the ambient phase (the bulk modulus at 100 GPa is thrice its value at P= 0 GPa), garnet to perovskite transition would involve further substantial increase of the bulk moldulus. The garnet GGG under dynamic compression has yielded a novel incompressible oxide phase with hardness greater than diamond [17]; perhaps similar phases with unusual hardness may be realized in YAG.

Our studies further indicate that the mechanical instability of YAG at high pressure is accompanied by large vibrational anharmonicity and changes in the mode Gruneisen parameters. The ambient phase mode Gruneisen values are all positive, while with increasing pressure many of the low energy modes (< 30 meV) show negative values and some of the high energy modes (> 60 meV) show sharp increase. The middle range remains more or less unchanged. The calculated partial density of states (Fig. 3.6) shows that Y and Al(2) atoms mainly contribution below 30 meV and above 60 meV respectively. The negative Γ values of low energy modes results in a lower value of overall positive thermal expansion coefficient, which in turn gives rise to a lower specific heat with increasing pressure.

3.3.5 Phonons and Born instability in Rare-earth Garnets

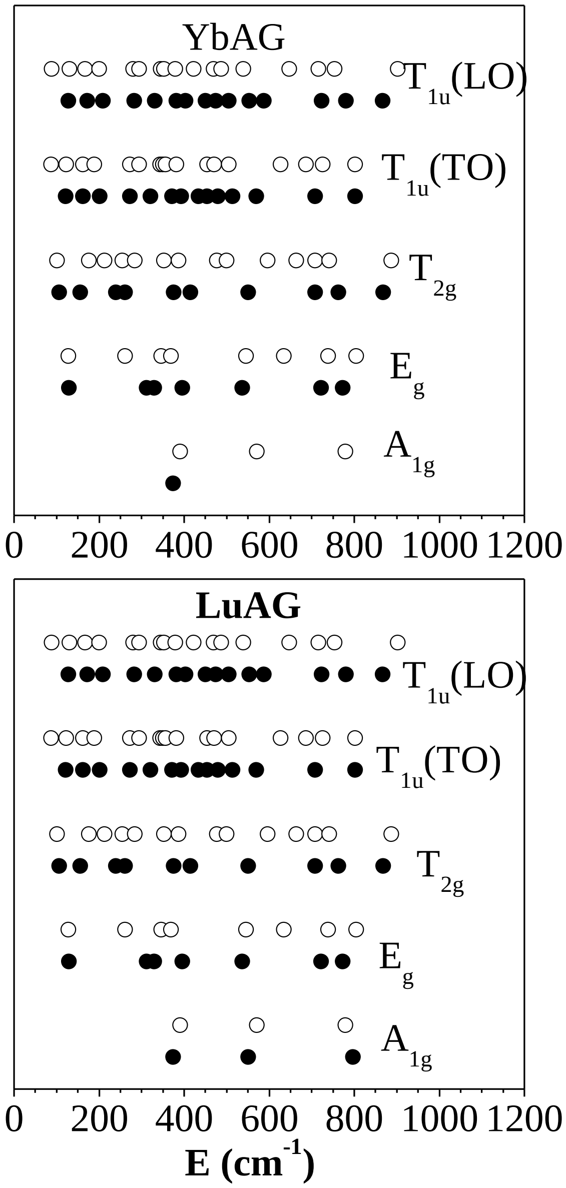

Fig. 3.11. *Zone-centre phonon frequencies, open circles are this calculation and solid circles are experimental [36] data.*

Rare-earth $Yb_3Al_5O_{12}$ and $Lu_3Al_5O_{12}$ behave similarly to YAG. They have the same crystal structure and have 80 atoms in the unit cell. Fig. 3.11 gives the phonon frequencies at the zone center in comparison with available data.

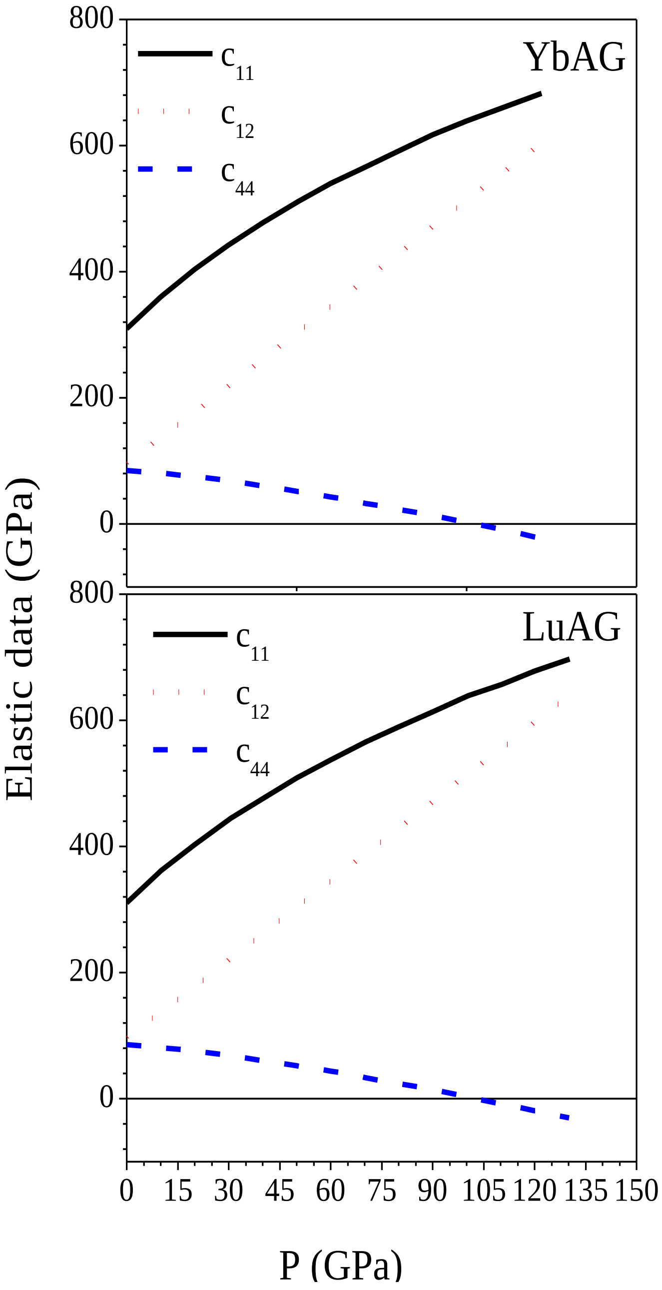

Fig. 3.12. *Born instability in $Yb_3Al_5O_{12}$ and $Lu_3Al_5O_{12}$. Here, $c_{11} = C_{11}-P$, $c_{12} = C_{12} + P$ and $c_{44} = C_{44}-P$, where C_{11}, C_{12} and C_{44} are the elastic constant values derived from slopes of the acoustic phonon branches.*

The calculated phonon frequencies are in very good agreement with available experimental data. Similar to YAG, these compounds also exhibit Born instability as can be seen from Fig. 3.12. Both the compounds violate the stability criteria above 100 GPa.

3.4 CONCLUSIONS

The author has reported detailed lattice dynamical calculations for the garnet YAG using a shell model. The calculated structure, elastic constants, phonon frequencies, specific heat, thermal expansion and equation of state of the ambient phase are in good agreement with available experimental data. At 100 GPa, YAG develops a large phonon band gap (90-110 meV) and its microscopic and macroscopic physical properties are found to be profoundly different from that at ambient pressure phase. The detailed high pressure studies conclude that YAG is mechanically unstable beyond 108 GPa, due to the violation of the Born stability criteria. Yb aluminium garnet and Lu aluminum garnet exhibit similar behavior. High pressure x-ray diffraction measurements report occurrence of a disordered phase between 100-150 GPa, and our studies suggest that these may perhaps be due to elastic instabilities.

Pressure induced amorphization has been observed in GGG and YIG. However, the cubic garnet structure is found to be stable in YAG upto significantly higher pressures and these studies reveal that upto 100 GPa there are no dynamical instabilities in YAG. Our results are in agreement with experimental studies which have suggested that YAG undergoes a phase change to a disordered metastable phase between 100-150 GPa. The observed high pressure phase beyond 100 GPa has not been clearly understood. The disordered phase perhaps occurs due to the large kinetic barriers for decomposition into the expected perovskite structure at high pressure.

Yttrium aluminum garnet, YAG and rare earth $Yb_3Al_5O_{12}$, $Lu_3Al_5O_{12}$ under ambient conditions, shows differences with the previous calculations on aluminosilicates garnets, namely there is no gap in the vibrational spectrum as seen in them. The Al atoms in tetrahedral and octahedral coordinations are dynamically distinct with aluminum in the tetrahedral coordination contributing between 90 and 120 meV. Yttrium atoms contribute mainly in the low energy range, while intermediate energy states are due to a combination of movements of all the atoms. YAG is found to be thermally stable in the temperature range (up to 1500 K) studied. Gruneisen constants of the low energy modes (< 30 meV) show great variation with increasing pressure, going from positive at 0 GPa to negative at 100 GPa. These modes become softer with pressure increase. The modes beyond 30 meV do not change much with changing pressure, excepting some modes which change drastically with ascending values of pressure. Thus, our results may have important implications for the proposed technological applications of YAG based materials as pressure sensors over a wide range of pressure.

Although author has employed an atomistic approach, the model is in good agreement with experiments and reported *ab initio* works. Furthermore the present work helps to understand the dynamical characteristics associated with the high pressure disordering and pressure induced amorphization. These aspects have not been clearly understood earlier. These results have important implications for use of YAG as pressure sensors in the high pressure regime. The shell model successfully gives a fair and comprehensive description of the dynamics and various thermodynamic properties at high temperatures and pressures which are otherwise difficult to access experimentally. Our studies are able to interpret complex high pressure data of YAG. This model has been successfully used to study rare-earth garnets and their elastic stability. It can be further used to study other similar garnets.

REFERENCES

[1] Walter Koechner, *Solid state laser engineering*, (Springer, 2006).

[2] B. Henderson and Ralph H. Bartram, *Crystal field engineering of solid state laser materials* (Cambridge University Press,2000).

[3] Yong-Nian Xu, W. Y. Ching Phys. Rev. B **59**, 10530 (1999).

[4] P. Djemia, F. Tetard, K. Bouamama, Eric Charron, D. Tetard, Y. Rabinovitch J. Eur. Cer. Soc. **27**, 4719 (2007).

[5] A. M. Hofmeister and K. R. Campbell J. Appl. Phys. **72**, 638 (1992).

[6] B. P. McAloon. and A. M. Hofmeister American Mineralogist **78**, 957 (1993).

[7] P.A Giesting and A.M Hofmeister, Phys. Rev. **B 65**, 144305 (2002).

[8] Yong-Nian Xu, W. Y. Ching, B. K. Brickeen Phys. Rev. *B* **61**, 1817 (2000).

[9] Jun Dong and Kunquan Lu Phys. Rev. *B* **43**, 8808 (1991).

[10] W. Y. Ching and Yong-Nian Xu Phys. Rev. **59**, 12815 (1999).

[11] Triplicane A. Parthasarthy, Tai-Il Mah and Kristen Keller J. Am. Cer. Soc. **75**, 1756 (1992).

[12] J.Liu and Y. K. Vohra, App. Phys. Lett. **64** 3366 (1994); J. Appl. Phy. **79**, 7978 (1996); Sol. St. Comm., **88**, 417 (1996).

[13] S. Kobyakov, A. Kaminska, A. Suchocki, D. Galanciak, M. Malinowski, App. Phys. Lett **88**, 234102 (2006).

[14] R Mittal, S L Chaplot, N Choudhury and C K Loong Phys. Rev. B **61**, 3983 (2000).

[15] R Mittal, S L Chaplot and N Choudhury Phy. Rev. B **64**, 094302 (2001).

[16] T. Irifune, Y. Higo, T. Inwe, Y. Kono, H. Ohfuji and K. Funakoshi, Nature **451**, 814 (2008).

[17] T. Mashimo, R. Chau, Y. Zang, T. Kobayoshi, T. Sekine, K. Fukuoka, Y. Syono, M. Kodama, W. J. Nellis, Phys. Rev. Lett. **96**, 105504 (2006).

[18] J. Chen, T C Lu, Y Xu, A. G. Xu and D. a. Chen, J. Phys.: Condens. Matter **20**, 325212 (2008).

[19] C. L. Wang, d. Solodovnikov and K. g. Lynn, Phys. Rev. B **73**, 233204 (2005).

[20] A. Anedda, C. M. Carbonaro, d. Chiriu, R. Corpino, M. Marceddu, R. c. Ricci, Phys. Rev. B **74**, 241508 (2006).

[21] B. John Gruber, B. Zandi, U.V. Valiev and Sh. A. Rakhimov, Phys. Rev. B **69**, 115103 (2004).

[22] Yongrong Shen, Toni Riedener and Kevin L. Bray, Phy. Rev. B **61**, 11460 (2000).

[23] Chen Jun, Chen dong-Quan and Zhang Jing-Lin, Chinese Phy. **16**, 2779 (2007).

[24] L. Schuh, R. Metselaar and C. R. A. Catlow J. Eur. Cer. Soc. **7**, 67 (1991).

[25] M. M. Kuklja J. Phys: Cond. Mater. **12**, 2953 (2000).

[26] Xian-jun Wang, W. M. Dennis, W. M. Yen J. Luminescence **53**, 44 (1992).

[27] Ferdinand Euler and Jane A Bruce, Acta Cryst. **19**, 971 (1965).

[28a] Hong Hua, Sergey Mirov, Yogesh K. Vohra Phys. Rev. B **54** 6200 (1996).

[28b] M. G. Beghi, C. E. Bottani and V. Russo, J. Appl. Phys. **87**, 1769 (2000).

[29] G. A. Saunders, S. C. Parker, N. Benbattouche, H. I. Alberts Phys. Rev. B **46**, 8756 (1992).

[30] P. R. Stoddart, P. E. Ngoepe, P. M. Mjwara, J. D. Comins and G A Saunders J. Appl. Phys. **73**, 7298 (1993).

[31] Y. K. Yogurtcu, A. J. Miller, G. A. Saunders J. Phys. C: Sol St. Phys. **13**, 6585 (1980).

[32] J. P. Hurell, S. P. S. Porto, I. F. Chang, S. S. Mitra, R. R. Bauman Phys. Rev. **173**, 851 (1968).

[33] W. J. Alton J. Appl. Phys. **38**, 3023 (1967).

[34] R. J. M. Konings, R. R. van der Laan, A. C. G. van Genderen and van Miltenburg Thermochimica acta **313** 201 (1998).

[35] S. Geller, G. P. Espinosa and P. B. Crandall J. Appl. Cryst. **2**, 86 (1969).

[36] K. Papagelis J. Phys: Cond. Mater. **14**, 915 (2002); **14**, 3875 (2002).

[37] K. Papagelis J. Phys. Chem. Solids **64**, 599 (2003).

[38] K. Papagelis, S. Ves J. Appl. Phys. **94**, 6491 (2003).

[39] K. Papagelis, J. Aravanitidis, G. Kanellis, S. Ves, G. A. Kourouklis J. Phys.: Con. Mat. **14**, 3875 (2002).

[40] K. Papagelis, G. Kanellis, J. Arvanitidis, G. A. Kourouklis and S. Ves Phys. Stat. sol. **215**, 193 (1999).

[41] J. Arvanitidis, K Papagelis, D Christofilos, H Kimura, G A Kournouklis, Ves S Phys. Stat. Sol, **b241**, 3149 (2004).

[42] A. G. Gavriliuk, V.V. Struzhkin, I. S. Lyubutin and I. A. Trojan, JETP lett. **82**, 603 (2005).

[43] S. L. Chaplot and S. K. Sikka, Phy. Rev. Lett., **71**, 2674 (1993).

[44] N. Choudhury and S. L. Chaplot, Phys. Rev. B **73**, 094304 (2006).

[45] L. Valenzano, A. Meyer, R. Demichelis, B. Civalleri and R. Dovesi Phy. Chem. Minerals, **36,** 415 (2009).

[46] A Meyer, Ph.’ D. Arco, R Orlando and R Dovesi Th. J. Phy. Chem. C **113**, 14507 (2009).

[47] J Chen, T C Lu, Y Xu, A G Xu and D Q Chen *J. Phys. Cond. Matt.* **20**, 325212 (2008).

[48] Amelie Juhin, George Calas, Delphine Cabaret, L Galoisy and Jean-Louis Hazemann *Amer. Min.*, **93**, 800 (2008).

[49] C M Zicovich-Wilson, F J Torres, F Pascale, L Valenzano, R Orlando and R Dovesi *J. Comp. Chem.* **9**, 2268 (2008).

[50] R Dovesi, L Valenzano, F Pascale, C M Ziovich-Wilson and R Orlando, *J. Ram. Spec.* **40** 416 (2008).

[51] V Cristiglio, Hennet L, G J Cuello, M R Johnson and A Fernandez-Martinez, H E Fischer, I Pozdnyakova, D Zhanghi, S Brasaamin, J F Brun and. D L Price, *J. Non. Cryst. Solids* **353** 1789 (2007).

[52] R Orlando, J Torres, F Pascale, P Ugliengo, C M Ziovich-Wilson and R Dovesi *J. Phys. Chem.* B **110(2)**, 692 (2006).

[53] Y Noel, M Catti, Ph. D' Arco and R Dovesi, *Phy. Chem. Min.* **33**, 383 (2006).

[54] L Vitos, B Magyari-Kope, R Ahuja, J Kollar, G Grimvall and B Johansson, *Phys. Earth & Planetary interiors*, **156**, 108 (2006).

[55] F Pascale, C M Zicovich-Wilson, R Orlando, C Roetti, P Ugliengo and R Dovesi, *J. Phys. Chem. B*, **109(13)**, 6146 (2005).

[56] F Pascale, M Catti, A Damin, R Orlando, V R Saunders, and R Dovesi, *J. Phys. Chem. B*, **109 (39)**, 18522 (2005).

[57] R Mittal, S L Chaplot Chaplot and N Choudhury, Progress of Materials Science **51**, 211 (2006).

[58] S L Chaplot, Narayani Choudhury, S Ghose, M N Rao, R Mittal and Prabhatasree Goel Eur. J Mineralogy **14**, 291 (2002).

[59] S L Chaplot report BARC-972 (1972)*;* Chaplot S L unpublished (1992).

[60] G. Venkataraman, L. Feldkamp, V. C. Sahni, *Dynamics of perfect crystals* (The MIT Press, Cambridge 1975).

[61] P Bruesh: *Phonons: theory and experiments* (springer Verlag, Berlin, 1986).

[62](a) Z. Zhou and B. Joos, Phys. Rev. B 54, 3841 (1996); (b) J. Wang and Sidney Yip, Phys. Rev. Lett., 71, 4182 (1993); (c) J. Wang, S. Yip, S. R. Phillpot and D. Wolf, Phys. Rev. B 52, 12627 (1995)

[63] A. A. Maradudin and S. H. Vosko, Rev. Mod. Phys. **40**, 1 (1968).

[64] O.V. Kovalev, *Irreducible representations of space groups* (New York: Gordon and Breach1964).

[65] C. J. Bradely and A. P. Cracknell, *The mathematical theory of symmetry in solids* (Oxford university press, Oxford 1972).

Chapter 4

Inelastic Neutron Scattering Studies of Phonon Spectra and Simulations in Tungstates, AWO_4 (A = Ba, Sr, Ca and Pb) and $LuVO_4$

4.1 INTRODUCTION

Compounds of the form MWO_4 (M = Mn, Cu, Ba, Sr *etc*) are studied [1-11] extensively for their interesting properties and usefulness. This thesis reports lattice vibrational studies on AWO_4 type tungstates with A = Ba, Sr, Ca and Pb, which are important for their scientific and technological applications [12-18]. These compounds in nano or bulk state find applications in solid- state scintillators [16-19], optoelectronic devices, solid state laser applications etc as well as in understanding of geological aspects. They also form a part of oxide ceramic composites useful for cryogenic detectors. These possible applications have motivated extensive interest in understanding the fundamental physical properties [20-31] of the AWO_4 tungstates. Rare-earth vanadates RVO_4, phosphates and arsenates whose crystal structure is the tetragonal zircon-type [29] with space group $I4_1/amd$ have received much attention in modern laser physics and non-linear optics. When doped with suitable ions, these vanadates serve as excellent host material for laser application. These materials have been employed as model systems for the investigation of polymorphism among ABO_4 type compounds. Sections 4.2 and 4.3 report studies done on tungstates and vanadates respectively.

4.2 Inelastic Neutron Scattering Studies of Phonon Spectra and Simulations in Tungstates

The compounds under normal conditions crystallize in the tetragonal scheelite [28] structure ($CaWO_4$ mineral structure). The scheelite structure (space group 88, Z = 4) adopted by AWO_4 has a body centered unit cell, with A atoms occupying S_4 symmetry while the sixteen oxygen atoms occupy C_1 sites. Each W is surrounded by four equivalent oxygen atoms in a tetrahedral symmetry and A is surrounded by eight oxygen atoms. Along a-axis the WO_4 units are directly aligned whereas along the c-axis, AO_8 dodecahedra are interspersed between two WO_4 tetrahedra. Hence, different arrangement of hard WO_4 tetrahedra along the **c** and **a**-axis accounts for the difference in compressibility of the two unit-cell axes. These compounds exhibit a rich phase diagram with respect to change in pressure and temperature [23]. Several experimental and theoretical efforts have been undertaken to obtain understanding of the phase diagram of the compounds [20-27], which still remains elusive. Extensive Raman [27,28,29] and infrared [30] scattering techniques have been used to study the zone centre phonon modes in several of these tungstates. Experimental studies using angle dispersive X-ray diffraction (ADXRD), x-ray absorption near edge structure measurements (XANES) have observed that upon compression at high pressures AWO_4 undergoes a scheelite to fergusonite phase transition at room temperature. This transformation is a displacive in nature [23]. The β angle of the high pressure monoclinic cell of the fergusonite phase is only a little different from 90º. Upon further compression the compounds change into denser monoclinic and orthorhombic phases, before amorphizing. In the meanwhile, experiments like Raman scattering suggest [27-29] that there is a possibility of a reconstructive, first order transition to $P2_1/n$ phase which coexists with the fergusonite phase. But this competing phase is kinetically hindered.

The author reports a complete and comparative details of the inelastic scattering experiments and theoretical studies on a series of tungstates as AWO_4 (A = Ba, Sr, Ca and Pb). The measurement of phonons density of states is carried out by using neutron inelastic scattering. The transferable interatomic potential has been developed and further used in molecular dynamics studies to understand the mechanism of pressure driven phase changes of AWO_4 (M = Ba, Ca, Sr and Pb). The author has looked at the changes occurring in the lattice under increasing pressure. The simulations have enabled us to understand the behavior of various polyhedra under compression.

4.2.1 Experimental details

Polycrystalline samples of the AWO_4 (A= Ba, Sr and Ca) were prepared by solid state reaction of appropriate amounts of alkaline earth carbonate (ACO_3) and WO_3. $PbWO_4$ was prepared by heating the precipitates obtained from $Pb(NO_3)_2$ and $(NH_4)_2WO_4$ solutions. The phonon density of states measurements of all AWO_4 (A= Ba, Sra, Ca, Pb) were performed in the neutron-energy gain mode with incident neutron energy of 14.2 meV. The data were taken over the scattering angle 10^o to 113^o. The signal is corrected for the contributions from the empty cell and suitably averaged over the angular range using the available software package at ILL. The incoherent approximation [32,33] was used in the data analysis. The data were suitably averaged over the angular range of scattering using the available software package at ILL to obtain the neutron-cross-section weighted phonon density of states. The multiphonon contribution has been calculated using the Sjolander [34] formalism and subtracted from the experimental data.

4.2.2 Theoretical Formalism

We have used a transferable interatomic potential to study the vibrational properties of the tungstates using lattice dynamics calculations. An interatomic potential as described in equation (1.25) consisting of short range and Coulombic terms is used. The radii parameters for M atoms are r_{Ca} = 2.06 Å, r_{Ba} = 2.4 Å, r_{Pb} = 2.25 Å and r_{Sr} = 2 Å respectively. The van der Waals interaction between O-O pairs is 80 eVÅ^6. The parameters of the WO_4 stretching potential described in equation (1.26), are D = 3.2 eV, r_o = 1.75 Å and n = 26.2 Å^{-1}. The polarizibility of the oxygen and alkali earth atoms has been considered in the framework of shell model with shell charge and shell core force constants for oxygen atoms as −2.0 and 50 eV/Å^2 and for alkaline atoms as 3.0 and 50 eV/Å^2 respectively.

Molecular dynamics (MD) simulations have been carried out using the model parameters obtained from the lattice dynamics calculations. A super cell consisting of 8×8×4 unit cells (6144 atoms) has been used to study the response of the compounds on compression. Rigid ion model has been used in the MD simulations. Calculations have been carried out from ambient pressure to around 50 GPa at room temperature. Equation of state has been integrated for about 1400 picoseconds using a timestep of 0.002 picoseconds.

4.2.3 Results and Discussion

The neutron inelastic scattering experiments have been performed using powder samples of the AWO_4 (M = Ba, Sr, Ca and Pb) at ambient conditions. The measurements have been carried out on the time of flight (TOF) instrument IN4C, ILL, Grenoble.

The measured phonon density of states of the four tungstates in comparison with potential model calculations is given in Fig. 4.1. The potential model calculations results are in good agreement with the inelastic neutron data. This has allowed validation of our model, which is further used to explore the phase stability of the compounds using molecular dynamics simulations as discussed below. The measured spectra show that phonons occur in two distinct regions in these compounds. The first region extends from 0 to 60 meV, while there is another region between 90-120 meV. The higher energy component corresponds to the internal vibrations of the WO_4 tetrahedra.

The calculated partial phonon densities of each atom of AWO_4 compounds are given in Fig. 4.2. It can be seen that the contribution from the A atoms extends up to 20 meV. The contribution of Pb atom is at the lowest energy while that of Ca at the highest energy. This is in commensurate with their relative atomic mass. The contribution from W atoms is confined within 20 meV, with a very small contribution up to 60 mev. There is another contribution above 90 meV in the band between 90-110 meV from W atoms. In case of oxygen, contribution is in the complete range 0-60 meV and in the band between 90 to 110 meV. The partial phonon densities ascertain that the contribution above 90 meV in the measured spectra is from the internal stretching modes of the W-O tetrahedra.

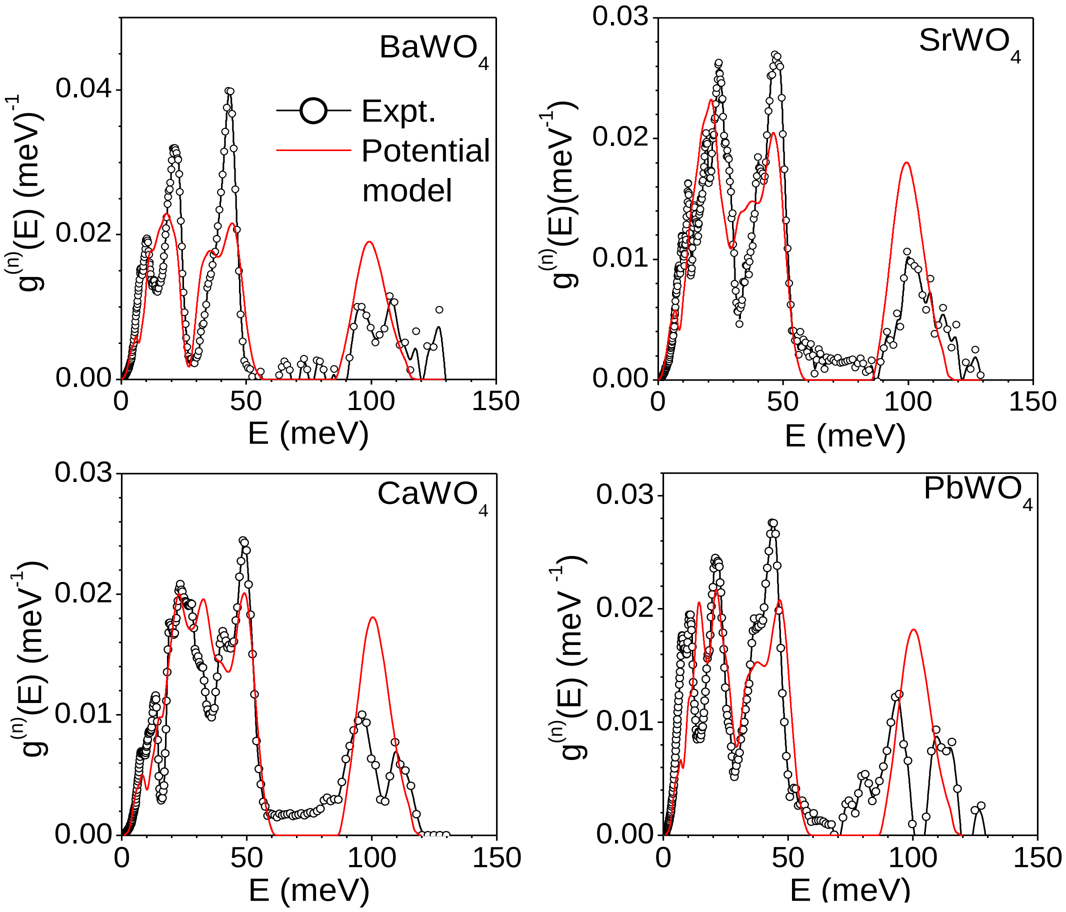

Fig. 4.1 *Neutron inelastic scattering data of the phonon density of states in AWO_4 (A = Ba, Ca, Sr and Pb) compared with shell model calculations.*

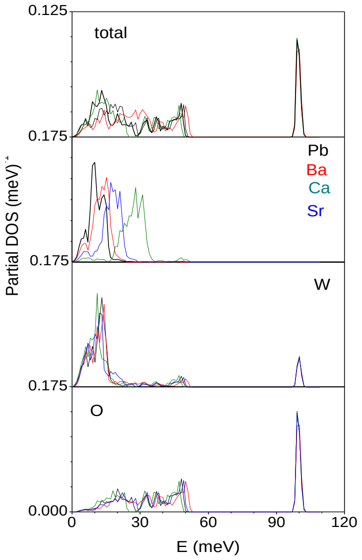

Fig. 4.2. *Calculated partial phonon density of states in all the three compounds*

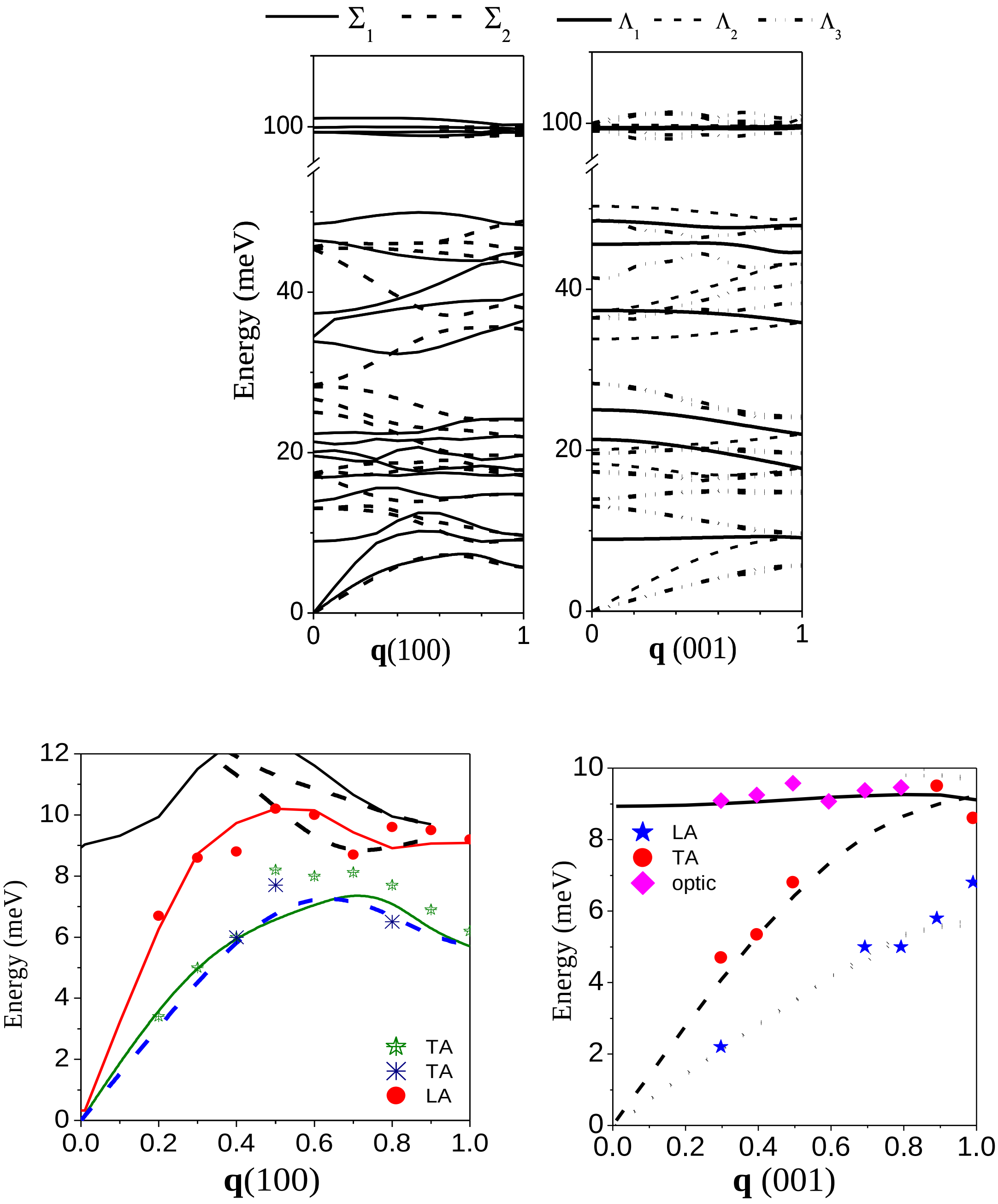

Fig. 4.3. *Calculated phonon dispersion in SrWO$_4$ along with measured phonon branches along [100] and [001] directions in single crystal of SrWO$_4$ using TAS, Dhruva, India. Solid symbols are the measured phonons. The full, dashed and dotted lines are the calculated phonon branches belonging to different representations as carried out by the author.*

Phonon dispersion relation in single crystal of $SrWO_4$ has been measured along [100] and [001] directions. Only the low energy acoustic modes have been measured. The calculated phonon dispersion along with measured phonon branches in the [100] and [001] directions is given in Fig. 4.3. The measurements have been carried out using TAS, Dhruva. The agreement between the measured and calculated phonon dispersion is good.

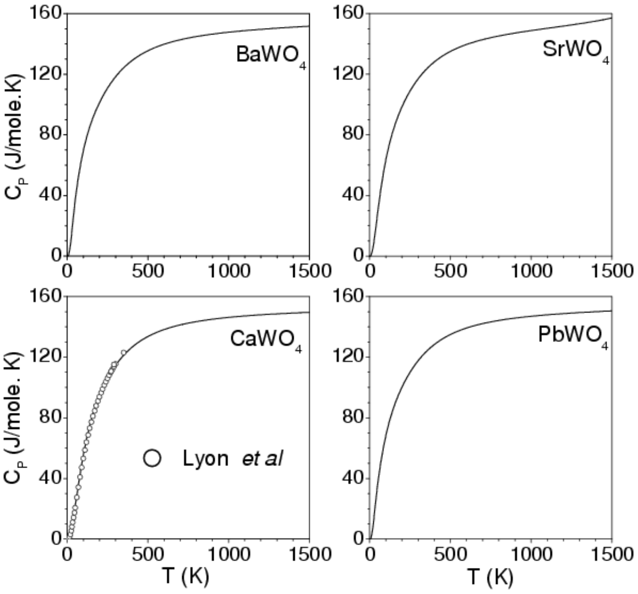

Fig.4. 4 *Experimental and computed (using potential model) specific heat in* AWO_4 *(A = Ba, Sr, Ca and Pb). The experimental data for* $CaWO_4$ *is from Ref. [35].*

The group theoretical distribution of phonons along high symmetry [001] and [100] directions is as follows:

Λ (001): 8 Λ_1 + 8 Λ_2 + 10 Λ_3 (Λ_3 is doubly degenerate)

Σ (100): 18 Σ_1 + 18 Σ_2

The symmetry vectors obtained through detailed group theoretical analysis along the two high symmetry directions and the zone centre point were employed to classify the phonon frequencies obtained into their irreducible representations.

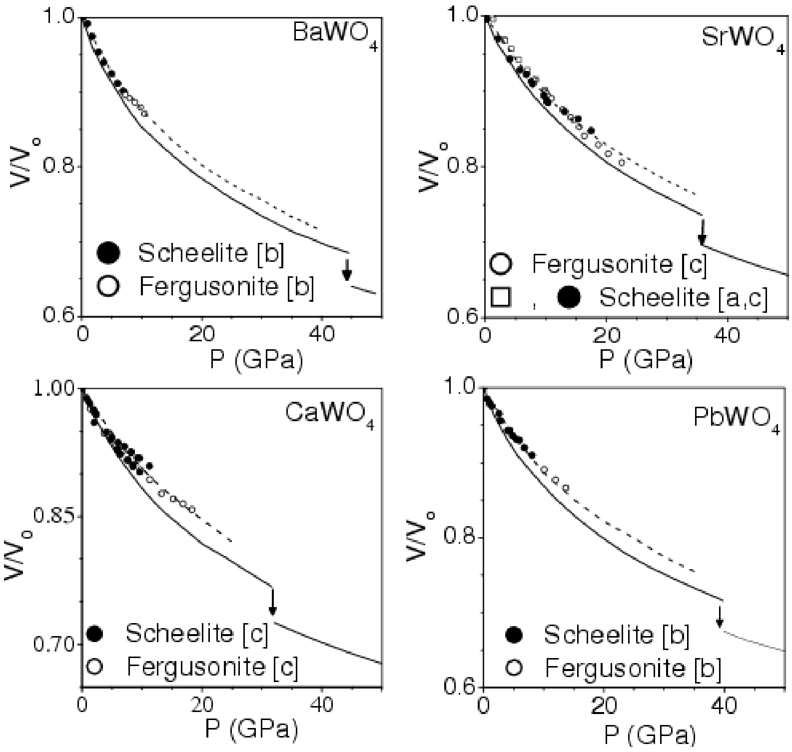

Fig. 4.5. *Calculated (using potential model) and experimental equation of state of AWO$_4$ (A = Ba, Ca, Sr and Pb). V and V$_o$ are the unit cell volume at high and ambient pressure respectively. 'a', 'b' and 'c' correspond to the experimental data from references [13], [24] and [27] . The full and dash lines correspond to calculations at T=300 K and 0 K respectively.*

The computed density of states has been used to determine the specific heat capacity of the four oxides as shown in Fig. 4.4. The available data on CaWO$_4$ [35] has been compared and is found to be in very good agreement with our calculated data. Using the interatomic potential developed, we have studied the pressure evolution of the tungstates. Fig. 4.5 gives the equation of state of the four compounds. These compounds are found to undergo initial transformation from scheelite (I4$_1$/a) to fergusonite (I2/a). According to experimental XANES [23,24] and ADXRD [23,24] studies, it is now well known that BaWO$_4$ transforms from scheelite to fergusonite phase at 7.5 GPa, PbWO$_4$

transforms at 9 GPa, $CaWO_4$ undergoes the above said transition at 11 GPa, and $SrWO_4$ at 10 GPa.

The pressure driven transition to fergusonite phase is of displacive in nature, it is known to be a second order phase transition with almost no discernable volume discontinuity. The change in the β angle is only feeble; change in the ‘b’ lattice parameters is also negligible. This change is not evident from our MD calculations.

In our molecular dynamics calculations we can see that there is a discontinuity in the pressure-volume curve (Fig. 4.4), which suggests a change in phase. In case of $CaWO_4$, this change is seen around 30 GPa, around 34 GPa in $SrWO_4$, in case of $PbWO_4$ it is around 38 GPa while in case of $BaWO_4$ it is around 45 GPa. Detailed studies were done to understand this sudden change in the equation of state. Fig. 4.5 gives the structural arrangement of the different polygons at different pressures (in $BaWO_4$) as obtained from our computations. At P = 0 GPa, the atoms are arranged in the scheelite structure, A atom is in AO_8 coordination while W is in tetrahedral WO_4 coordination. Regions B and C are identified to depict the coordination of A and W atoms. As pressure is increased, at 43 GPa, there is no visible change in the structural arrangement of the various polygons. There is no change in the coordination around A and W atoms. Beyond 45 GPa, there is a volume drop in $BaWO_4$. This observation coincides with the volume discontinuity observed around 45 GPa in $BaWO_4$ in Fig.4.5. The structure at 47 GPa shows several obvious changes as compared to earlier structures. In region C, it can be seen that A atoms are no longer in perfect bisdisphenoids, instead it is now seen in a highly distorted polygon. In region B, W atoms show significant changes, the co-ordination number has increased. Most of the WO_4 tetrahedra have changed in to distorted WO_6.

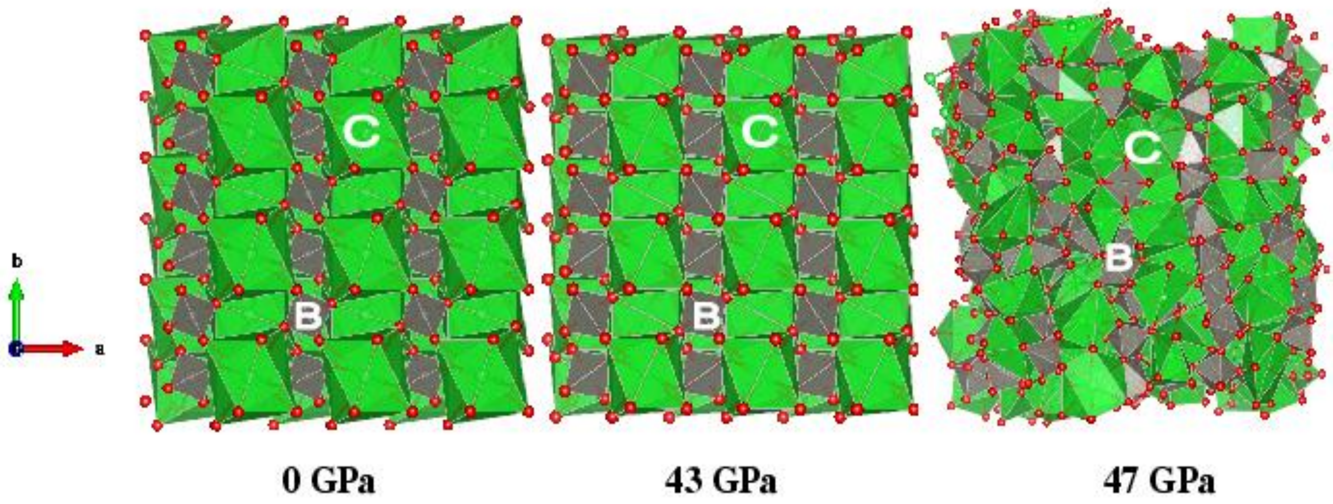

***Fig. 4.6**. The structure of $BaWO_4$ super cell evolving under pressure. Regions B and C are marked to depict and understand the change in coordination around A and W atoms. (**c**-axis is perpendicular to the plane of the paper)*

Further credence to this observation is obtained from the O-W-O bond angle distribution given in Fig.4.7. At ambient pressure, all WO_4 tetrahedra are regular with O-W-O angle equal to 109°. At 43 GPa, WO_4 tetrahedra are still regular. But on amorphization, the increase in coordination has resulted in the change in the bond angle.

Majority of the O-W-O angle is around 90º which corresponds to an octahedral arrangement. Not all the W's have attained a coordination of 6; hence, distortment of the tetrahedra has given rise to a range of angles for the O-W-O bond as seen in Fig. 4.7 Similar behavior is seen in all the remaining tungstates. In order to obtain a deeper understanding into this volume discontinuity, we have studied the local order in the lattice between various atomic pairs. The pair correlations have been computed in these compounds with increasing pressure. Fig. 4.8 shows the pair-correlation function between A-W, A-O, A-A, W-W, W-O and O-O at various pressures. We find that with increasing pressure, there are subtle and small changes in the correlations between the different atomic pairs. In case of $BaWO_4$, the correlations broaden beyond 47 GPa, as seen from the plots in Fig. 4.8. This is in very good agreement with the reported value [24] of 45 GPa for amorphization in $BaWO_4$. In case of $CaWO_4$, the broadening of peaks appear around 32 GPa, while the experiments show [28] amorphization around 40 GPa. Our molecular dynamics calculations predict that in case of $SrWO_4$, at 36 GPa the peaks in the calculated pair correlations broaden, implying that the discrete ordering is lost. In $PbWO_4$, similar trend is observed at 40 GPa. These observations are in tandem with the equation of states (Fig. 4.5) computed in each of the compounds.

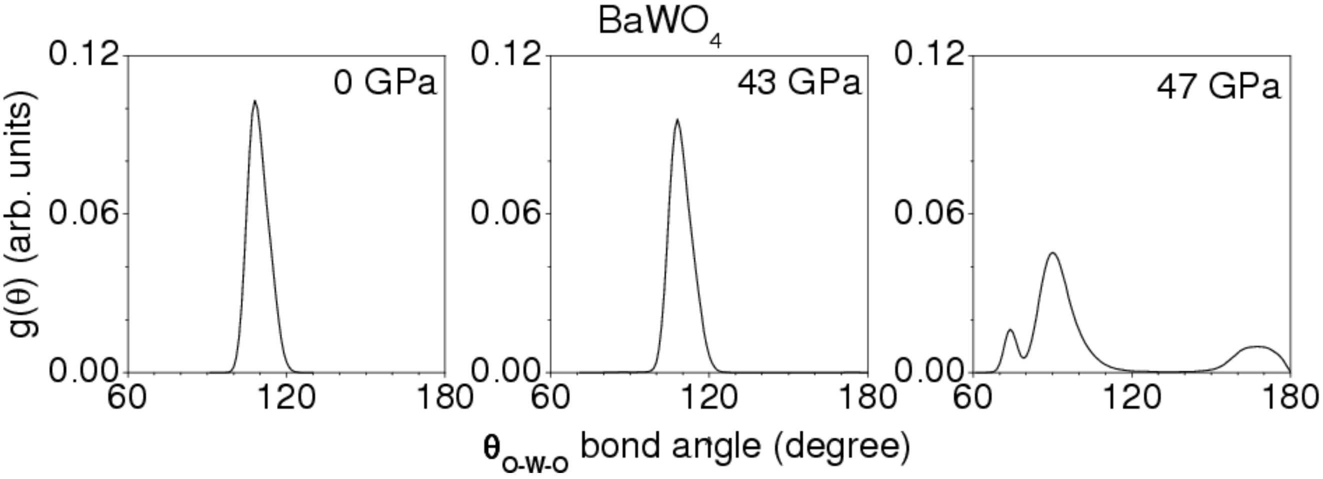

Fig. 4.7: *Intratetrahedral bond angle O-W-O with changing pressure in* $BaWO_4$.

Careful investigations of the various atomic pairs reveal some interesting observations. In case of A-O pair distribution, we find that changes due to increase in pressure is seen to occur gradually, as can be seen in the inset of the Ba-O pair distribution. There is gradual decrease in the bond length on going from 0 GPa to 43 GPa. The BaO_8 units are able to withstand the increased pressure with gradual rearrangements of the Ba-O bonds, but beyond 43 GPa, the polyhedra distorts considerably. This leads to the broadening of peaks, suggesting the loss of long range order. In case of WO_4 tetrahedra, there is almost no change in the bond-length (changes by about 0.015 Å) as pressure is increased from 0 to 43 GPa (Inset Fig. 4.8).

However further increase in pressure beyond a threshold of 45 GPa leads to an abrupt increase in the W-O bond by about 0.1 Å. Hence it can be inferred that WO_4 tetrahedra is almost immune to changes in pressure up to an upper threshold of pressure, whose value is different for each of the tungstate. Beyond this threshold, WO_4 tetrahedra distort and W atom's coordination increases.

Our above said observations are in tandem with experimentally [24] observed amorphization around 45 GPa in $BaWO_4$ and at around 40 GPa in $CaWO_4$ [28]. The equation of state for various compounds has also been obtained (Fig. 4.5) from minimization of the enthalpy at 0 K. Table 4.1 gives the bulk modulus and its pressure derivative for the four compounds in comparison with the available reported experimental data [24]. The values are obtained from fitting of the Birch equation of state [36] to the calculated equation of states.

TABLE 4.1 : Comparison between the experimental and calculated bulk modulus (B) (in GPa units) and its pressure derivate (B'). The experimental values at 300 K are from Ref. [24]. The B values at 300 K has been obtained using the B' values estimated at 0 K.

	$BaWO_4$		**$CaWO_4$**		**$SrWO_4$**		**$PbWO_4$**	
	B	**B'**	**B**	**B'**	**B**	**B'**	**B**	**B'**
Expt. (300 K)	52(5)	5(1)	74(7)	5.6(9)	63(7)	5.2(9)	66(5)	5.6(9)
Calc. (0 K)	55.8(8)	4.4(1)	80.1(5)	4.5(1)	69.9(2)	4.5(3)	61.7(7)	5.1(1)
Calc. (300 K)	46.8(4)	4.4	62.1(4)	4.5	56.3(6)	4.5	49.8(3)	5.1

Earlier studies [23] surmise that large ratio of ionic radii (WO_4/A) accommodates increased stresses through larger and more varied displacement from their average positions. This results in the loss of translational periodicity at high-pressure. Larger the WO_4/A ratio, lower the pressure threshold for pressure induced amorphization. This ratio decreases as per the following order: WO_4/Ca>WO_4/Sr>WO_4/Pb>WO_4/Ba. As per this notion, $CaWO_4$ should have the lowest value of pressure for amorphization to occur, followed by $SrWO_4$, $PbWO_4$ and $BaWO_4$ respectively. Our computed results are in full agreement with this expected trend.

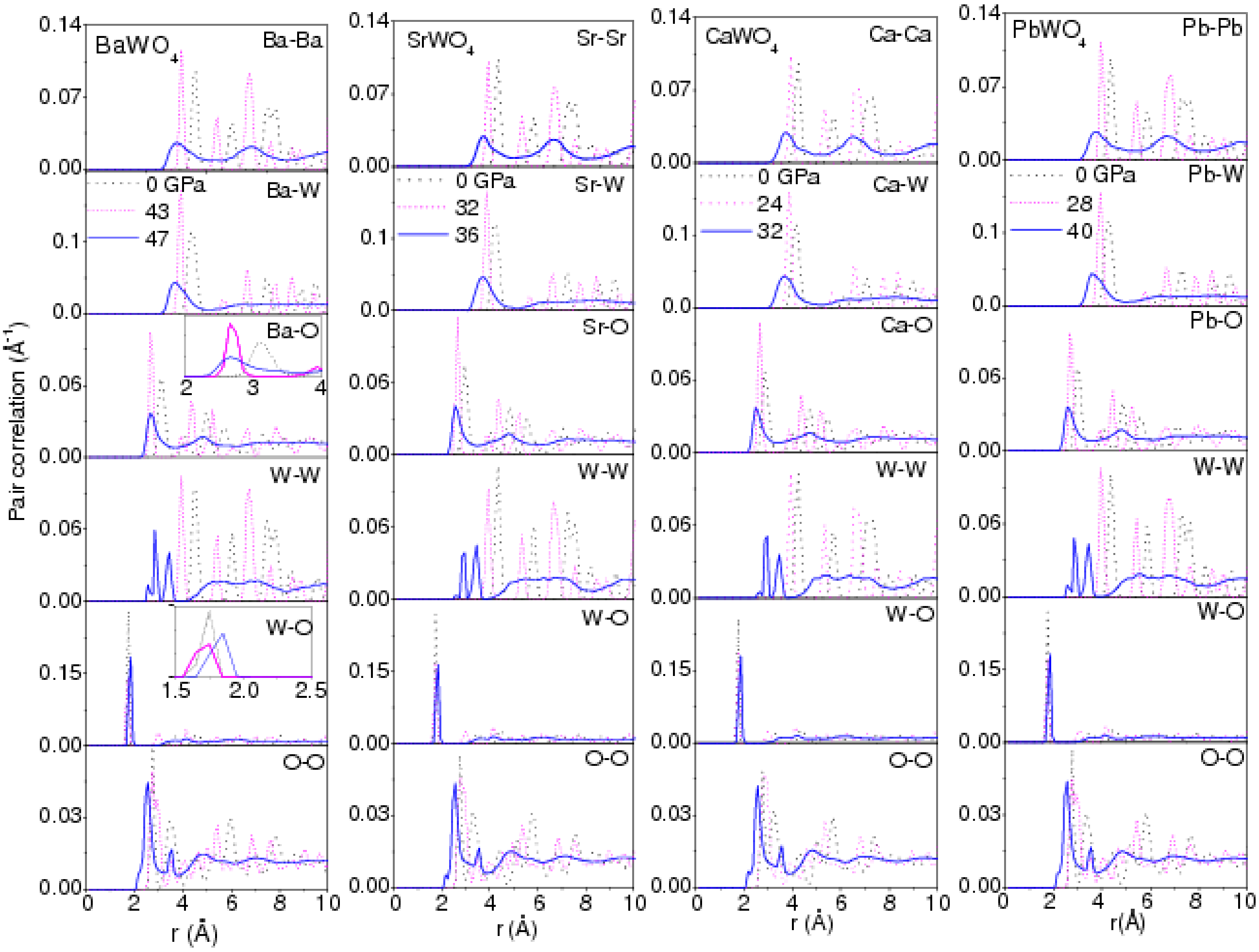

Fig. 4.8 *Pair correlations between various atomic pairs as obtained from molecular dynamics simulations.*

4.3 Inelastic Neutron Scattering, Lattice Dynamics and High Pressure Stability of $LuVO_4$

4.3.1 Introduction

Rare-earth vanadates RVO_4, phosphates and arsenates whose crystal structure is the tetragonal zircon-type [29] with space group $I4_1/amd$ have received much attention in modern laser physics and non-linear optics. When doped with suitable ions, these vanadates serve as excellent host material for laser application. In this each R ion is coordinated by 8 oxygen atoms, forming dodecahedral cages and the V ion is coordinated by 4 oxygen atoms, forming VO_4 tetrahedra. The unit cell consists of four formula units. These materials have been employed as model systems for the investigation of polymorphism among ABO_4 type compounds.

$LuVO_4$ has been found to transform to a pressure quenchable scheelite phase ($I4_1/a$) with approximately 10% reduction in volume at around 8 GPa [37]. This reduction is due to a more efficient polyhedral packing when the ambient phase is pressurized well above the equilibrium transition pressure. This section deals with studies on the lattice dynamics of this vanadate in the quasiharmonic approximation. The presence of several atoms in the unit cell (in this case the primitive cell contains two formula units *ie*, 12 atoms) justifies the use of an atomistic approach to study the vibrational and thermodynamic properties. The inelastic neutron scattering studies have been carried out on a polycrystalline sample to obtain the phonon density of states in the entire Brillouin zone.

4.3.2 Experiment and theoretical calculations

The inelastic neutron scattering studies on a polycrystalline sample of $LuVO_4$ was carried out using the High Resolution Medium Energy Chopper Spectrometer (HRMECS) at the intense pulsed neutron source of Argonne National laboratory (ANL), USA. It is a time of flight spectrometer equipped with a large detector bank covering a wide-range (-10^0 to 140^0) of scattering angles. The measurements were performed in collaboration with Dr. C. -K. Loong, ANL, USA.

A shell model potential (as described in equation (1.25) chapter 1) consisting of Coulombic terms and short range terms has been used for the calculations of the lattice dynamics of these vanadates. A covalent term (equation (1.26)) is used to explain the stretching frequencies of the VO_4 molecular unit. The radii and charge parameters for Lu, V and O atoms are r_{Lu} = 2.161 Å, r_V = 0.953 Å, r_O = 1.855 Å and Z_{Lu} = 2.971e, Z_V = 3.013e respectively. The van der Waals interaction between O-O pairs is 22 eVÅ^6. The parameters of the WO_4 stretching potential described in equation (1.26), are D = 1.96 eV, r_o = 1.7 Å and n = 26.2 Å^{-1}. The parameters of the potentials satisfy the conditions of static and dynamic equilibrium. The polarizibility of the oxygen atoms has been introduced in the framework of shell model.

4.3.3 RESULTS AND DISCUSSION

4.3.3.1 Phonon density of states

The zircon structure adopted by the compound at ambient condition with two formula units per primitive cell, supports 36 zone-center phonon modes. Group theoretical considerations lead to the following vibrational representation at the Γ point (zone-centre, $\Gamma = 2A_{1g} + 2B_{1u} + 4B_{1g} + 4A_{1u} + A_{2g} + B_{2u} + B_{2g} + A_{2u} + 5E_g + 5E_u$), A and B modes are nondegenerate, whereas the E modes are doubly degenerate. The modes A_{1g}, B_{1g}, B_{2g} and E_g are Raman active, while A_u and E_u are infrared active.

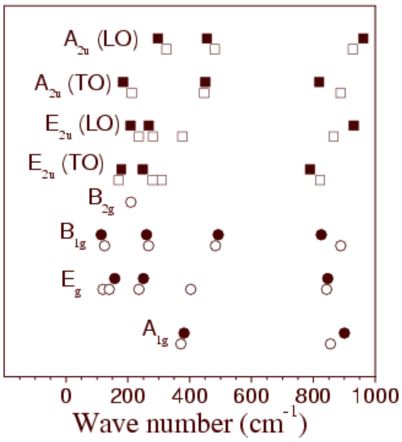

Fig. 4.9 *Comparison of experimentally reported data of optically active modes with calculated values. Open and closed symbols correspond to the calculated and experimental [38,39] results.*

The calculated phonon frequencies with mode assignments are compared with the available Raman and infrared data [48,49] in Fig. 4.9. The comparison between the experimental and calculated density of states is shown in Fig. 4.10. The peak around 40 meV in the experimental data has been shifted to higher energies in our calculations while all other phonon peaks agree well.

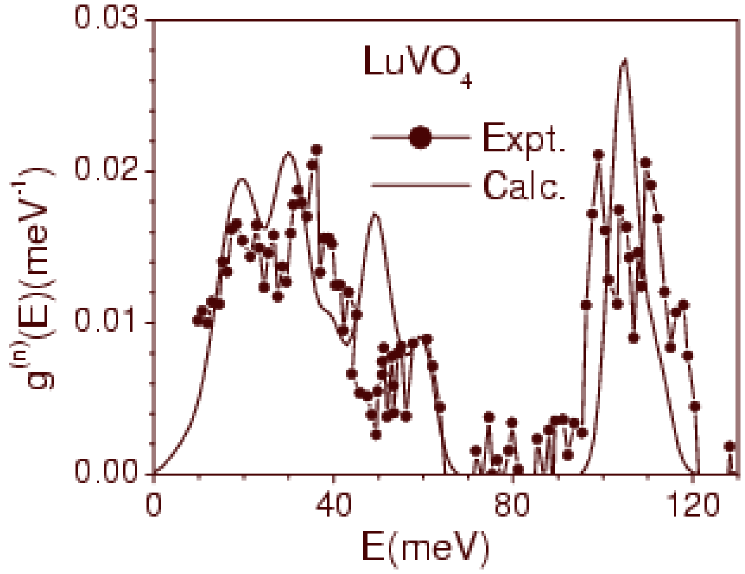

Fig 4.10 *Inelastic neutron scattering data in comparison with the calculated density of states.*

4.3.3.2 High Pressure Phase Transition in LuVO4

Gibb's free energy of a given crystalline phase includes contributions from enthalpy and vibrational entropy at a given temperature and pressure. In our calculations, along with enthalpy changes, we have also taken into consideration vibrational entropy contribution by calculating the phonon density of states in the entire Brillouin zone. During phase transitions, the stability of a crystalline phase is determined by the minimum free energy of the competing phases.

The Gibbs free energy of the two phases has been compared (Fig. 4.11) at different pressures at 300 K. The results indicate that transition to scheelite phase occurs around 8 GPa, which is in excellent agreement with the reported transition pressure of 7.9 GPa.

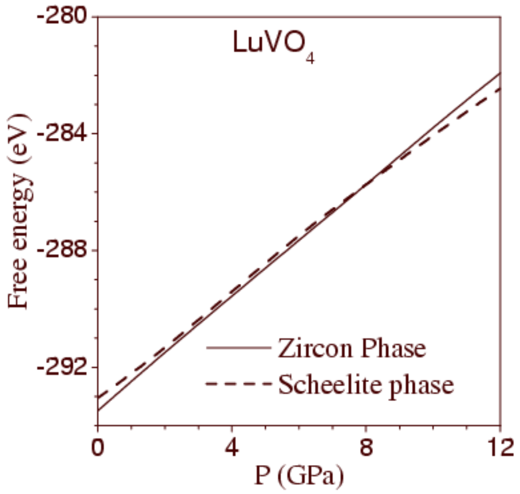

Fig. 4.11. *Free energies of competing phases in LuVO$_4$ at 300 K.*

The computed drop in volume is around 8% while experimental studies [37] indicate a drop of about 11%. In this displacive phase transition, author finds that the change in free energy due to volume is dominant in comparison to changes due to vibrational entropy.

4.4 CONCLUSIONS

A combination of potential model and neutron inelastic scattering has been used to study the vibrational properties in the four tungstates. Molecular dynamics simulations have been employed to understand their evolution with increasing pressure. Inelastic neutron scattering experiments have been carried out to phonon dispersion in single crystal of SrWO$_4$, and to measure the phonon density of states in all the four compounds. The calculations are in good agreement with experimentally measured data. With increasing pressure, tungstates undergo transition from scheelite to fergusonite phase, it is a second order displacive transition with no apparent volume discontinuity. This transition is not evident in our calculations. But with further increase in pressure, these tungstates show pressure induced loss of translational ordering, which is seen by the sudden drop in volume in all the four tungstates studied, using molecular dynamics simulations. On amorphization WO_4 tetrahedra deform, the coordination of W atoms increases from 4. The AO_8 polyhedra show considerable distortion. The calculated amorphization pressures for $BaWO_4$ and $CaWO_4$ are in agreement with the available experimental data. The molecular dynamics simulations facilitates in predicting the amorphization in $SrWO_4$ and $PbWO_4$ at high pressures.

Further we have also studied lattice dynamics and high pressure studies on $LuVO_4$. Our model calculations are able to explain the obtained density of states very well. Our calculations reproduce the pressure-driven phase transition from zircon to scheelite in $LuVO_4$ with excellent accuracy. This study indicates that similar investigations on rare earth vanadates and arsenates would be rewarding, particularly in establishing the systematics of crystal-chemical aspects of the pressure-induced transition in zircon-type structured compounds.

References

[1] D. Niermann, C. P. Grams, M. Schalenbach, P. Becker, L. Bohaty, J. Stein, M. Braden and J. Hemberger, Phys. Rev. B **89**, 134412 (2014).

[2] M. Baum, J. Leist, Th. Finger, K. Schmalzl, A. Hiess, L. P. Regnault, P. Becker, L. Bohaty, G. Eckold and M. Braden, Phys. Rev. B **89**, 144406 (2014).

[3] N. Poudel, K. C. Liang, Y. Q. Wang, Y. Y. Sun, B. Lorenz, F. Ye, J. A. Fernandez Baca and C. W. Chu, Phys. Rev. B **89**, 054414 (2014).

[4] I. V. Solovyev, Phys. Rev. B **87**, 144403 (2013).

[5] J. Ruiz Fuertes, S. Lopez Moreno, J. Lopez Solano, D. Errandonea, A. Segura, R. Lacomba Perales, A. Munoz, S. Radescu, P. Rodriguez-Hernandez, M. Gospodinov, L. L. Nagomaya and C. Y. Tu, Phys. Rev. B **86,** 125202 (2012).

[6] J. Ruiz-Fuertes, A. Segura, F. Rodriguez, D. Errandonea and M. N. Sanz Ortiz, Phys. Rev. Lett. **108**, 166402 (2012).

[7] S. Lopez-Moreno, P. Rodriguez-Hernandez, A. Munoz, A. H. Romero and D. Errandonea, Phys. Rev. B **84**, 064108 (2011).

[8] J. Ruiz Fuertes, D. Errnadonea, S. Lopez-Moreno, J. Gonzalez, O. Gomis, R. Vilaplana, F. J. Manjon, A. Munoz, P. Rodriguez Hernandez, A. Friedrich, I. A. Tupitsyna and L. L. Nagornaya, Phys. Rev. B **83**, 214112 (2011).

[9] F. J. Manjon, J. Lopez-Solano, S. Ray, O. Gomis, D. Santamaría-Pérez, M. Mollar, V. Panchal, D. Errandonea, P. Rodríguez-Hernandez, and A. Munoz, Phys. Rev. B **82**, 035212 (2010).

[10] J. Ruiz-Fuertes, D. Errandonea, R. Lacomba-Perales, A. Segura, J. González, F. Rodríguez, F. J. Manjon, S. Ray, P. Rodríguez-Hernández, A. Muñoz, Zh. Zhu, and C. Y. Tu, Phys. Rev. B **81**, 224115 (2010).

[11] R. Lacomba Perales, D. Errandonea, D. Martinez Garcia, P. Rodriguez Hernandez, S. Radescu, A. Mujica, A. Munoz, J. C. Chervin, and A. Polian, Phys. Rev. B **79**, 094105 (2009).

[12] R. Lacomba Perales, D. Martinez García, D. Errandonea, Y. Le Godec, J. Philippe, G. Le Marchand, J. C. Chervin, A. Polian, A. Munoz, and J. Lopez Solano, Phys. Rev. B **81**, 144117 (2010); V. Panchal, N. Garg, A. K. Chauhan, Sangeeta, and S. M. Sharma, Solid State Commun. **130**, 203 (2004).

[13] D. Errandonea, J. Pellicer Porres, F. J. Manjon, A. Segura, Ch. Ferrer Roca, R. S. Kumar, O. Tschauner, P. Rodríguez Hernández, J. Lopez Solano, S. Radescu, A. Mujica, A. Munoz, and G. Aquilanti, Phys. Rev. B **72**, 174106 (2005).

[14] Y. Zhang, N. A. W. Holzwarth, and R. T. Williams, Phys. Rev. B **57**, 12738 (1998).

[15] R. Lacomba-Perales, D. Errandonea, A. Segura, J. Ruiz-Fuertes, P. Rdriguez-Hernandez, S. Radescu, J. Lopez-Solano, A. Mujica and A. Munoz, J. Appl. Phys. **110**, 043703 (2011)

[16] A. A. Annenkov, M. V. Korzhik, and P. Lecoq, Nucl. Instrum. Methods, Phys. Res. A **490**, 30 (2002)

[17] M. Nikl, P. Bohacek, E. Mihokova, N. Solovieva, A. Vedda, M. Martini G. P. Pazzi, P. Fabeni, M. Kobayashi, and M. Ishii, J. Appl. Phys. **91**, 5041 (2002).

[18] A. Brenier, G. Jia, and C. Y. Tu, J. Phys.: Condens. Matter **16**, 9103 (2004).

[19] H. E. Chao, Y. Kuisheng, L. Lei and S. I. Zhenjun, J. Rare Earths **31,** 790 (2013).

[20] A Grzechnik, W. A Crichton, M. Hanfled, Phys. Stat. Solidi **242** 2795 (2005).

[21] J. Lopez Solano, P. Rodriguez Hernandez, S. Radescu, A. Mujica, A. Munoz, D. Errandonea, F. J. Manjon, Pellicer Porres J, Garro N, Segura A, Ch. Ferrer Roca, R. S. Kumar, O. Tschauner and G. Aquilanti, Phys. Stat. Sol. B **244,** 325 (2007).

[22] F. J. Manjon, , D. Errandonea, J. Lopez Solano, P. Rodríguez Hernandez, S. Radescu, A. Mujica, A. Munoz, N. Garro, J. Pellicer Porres, A. Segura, Ch. Ferrer Roca, R. S. Kumar, O. Tschauner, and G. Aquilanti. Phys. Stat. Sol. (b**) 244**, 295 (2007).

[23] (a) F. J. Manjon and D. Errandonea, Prog. Mat. Sci. **53**, 711 (2008) and references therein. (b) P. Blanchfield and G. A. Saunders, J. Phys. C: Sol. Stat. Phys. **12**, 4673 (1979).

[24] D. Errandonea, J. Pellicer Porres, F. J. Manjon, A. Segura, Ch. Ferrer-Roca, R. S. Kumar, O. Tschauner, J. Lopez -Solano, P. Rodríguez-Hernandez, S. Radescu, A. Mujica, A. Munoz, and G. Aquilanti Phys. Rev. B **73,** 224103 (2006) and references therein.

[25] F. J. Manjon, D. Errandonea, N. Garro, J. Pellicer Porres, J. Lopez -Solano, P. Rodríguez-Hernandez, S. Radescu, A. Mujica and A. Munoz Phys. Rev. B **74,** 144111 (2006).

[26] F. J. Manjon, D. Errandonea, N. Garro, J. Pellicer-Porres, J. López-Solano, P. Rodríguez Hernandez, S. Radescu, A. Mujica, and A. Muñoz, Phys. Rev. B **74**, 144112 (2006).

[27] P. Rodriguez Hernandez, J. Lopez-Solano S. Radescu, A. Mujica, A. Munoz, D. Errandonea, F. J. Manjon, J. Pellicer Porres, A. Segura, Ch. Ferrer Roca, R. S. Kumar, O. Tschauner and G. Aquilanti, J. Phys. Chem. of solids **67**, 2164 (2006).

[28] D. Errandonea, M. Somayazulu and D. Hausermann, Phys. Stat. Sol. (b) **235**, 162 (2003)

[29] W. Sleight, Acta Crystallogr. B **28**, 2899 (1972); R. W. G. Wyckoff, Crystal structure (2nd edn) Vol **3** Interscience, New York (1965).

[30] A. Jayaraman, B. Batlogg and L. G. VanVitert, Phys. Rev. B **31**, 5423 (1985); **28**, 4774 (1983).

[31] P. J. Miller, R. K. Khanna and E. R. Lippincott J. Phys. Chem. Solids **34,** 533 (1973)

[32] J. M. Carpenter and D. L. Price, Phys. Rev. Lett. **54**, 441 (1985).

[33] D. L. Price and K. Skold, in *Methods of experimental physics: Neutron scattering Part A*, edited by K. Skold and D. L. Price (Academic Press, Orlando, 1986), Vol. **23.**

[34] A. Sjolander, Arkiv fur Fysik **14**, 315 (1958).

[35] W.G. Lyon and W.F. Edgar, J. Chem. Phys., **49** 3374 (1968).

[36] F. Birch, J. Geophys. Res. **57**, 227 (1952).

[37] R. Mittal, A. B. Garg, V. Vijayakumar, S. N. Achary, A. K. Tyagi, B. K. Godwal, E. Busetto, A. Lausi and S. L. Chaplot, J.Phys. (Condens. Mattter) **20**, 075223 (2008).

[38] C. C. Santos, E. N. Silva, A. P. Ayala, I. Guedes, P. S. Pizani, C. K. Loong and L. A. Boatner, J. App. Phys. **101**, 053511 (2007).

[39] A. Armbruster, J. Phy. Chem. Solids, **37**, 321-327 (1976).

Chapter 5

Neutron Instrumentation

Focussing monochromator for Triple Axis Spectrometer, Dhruva Reactor

5.1 Motivation

Single crystals consist of large number of mosaic blocks. The distribution of orientations of these blocks may be assumed to be Gaussian. The Full width at Half Maximum (FWHM) of this distribution is a measure of the mosaic spread of the crystal[1,2]. In general, as-grown single crystals have very small mosaic spread and, as a consequence, reflectivity of neutron beam from such perfect crystals is low. Neutron sources have low flux (10^{14} neutrons/cm^2/sec) in comparison with x-ray sources. Hence, a perfect crystal is not suitable for use as a monochromator.

Monochromator form an integral part of a neutron spectrometer. To circumvent the above mentioned problem, a focusing monochromator is the preferred option for obtaining an increased flux on the sample. A double focusing monochromator is being installed on the Triple Axis Spectrometer at Dhruva. Fifteen perfect single crystals of copper are to be mounted on the focusing monochromator assembly. The monochromator assembly consists of a 3 × 5 matrix of crystal holders, where Cu single crystals need to be fixed. Perfect Cu single crystals (15 in numbers of size 35 mm × 25 mm × 10 mm) of mosaic spread ~0.1° were procured. Mosaic spread of monochromator crystals need to be around 0.5°to attain perfect balance between resolution and reflectivity, in order to be used as focusing crystals. As acquired perfect copper single crystals (with a measured mosaic spread of about 0.15°) were pressed using a hydraulic press along [111] axis in steps with varying load and time. The mosaic spreads of the crystals were monitored step wise and all crystals were pressed such that their mosaic spread is increased to or beyond 0.5°. These crystals were subsequently placed on the focusing monochromator assembly forming a matrix of 3 × 5. Each of the 15 copper crystals were aligned individually as well as on the assembly, which is ready to be installed at the Triple Axis Spectrometer, Dhruva. I was involved in the collaborative instrumentation activities related to increase in mosaic spread of perfect copper crystals, alignment and focusing of the monochromator assembly.

5.2 Mechanical treatment of the perfect single crystals

It has been shown previously that thermo-mechanical treatment on perfect single crystals of copper and germanium is fruitful in increasing their mosaic spread up to 0.3^o [1]. Here we present our results of mechanical treatment on nearly perfect copper crystals. We were able to increase the mosaic spread of perfect copper crystals by applying load along the [111] axis. The mosaic spread can be increased up to 0.5^o without affecting the peak reflectivity of the crystal. The mosaic spread of the crystals was measured using triple axis spectrometer installed inside DHRUVA reactor hall. The ray diagram of the experimental set up is shown in Fig. 5.1.

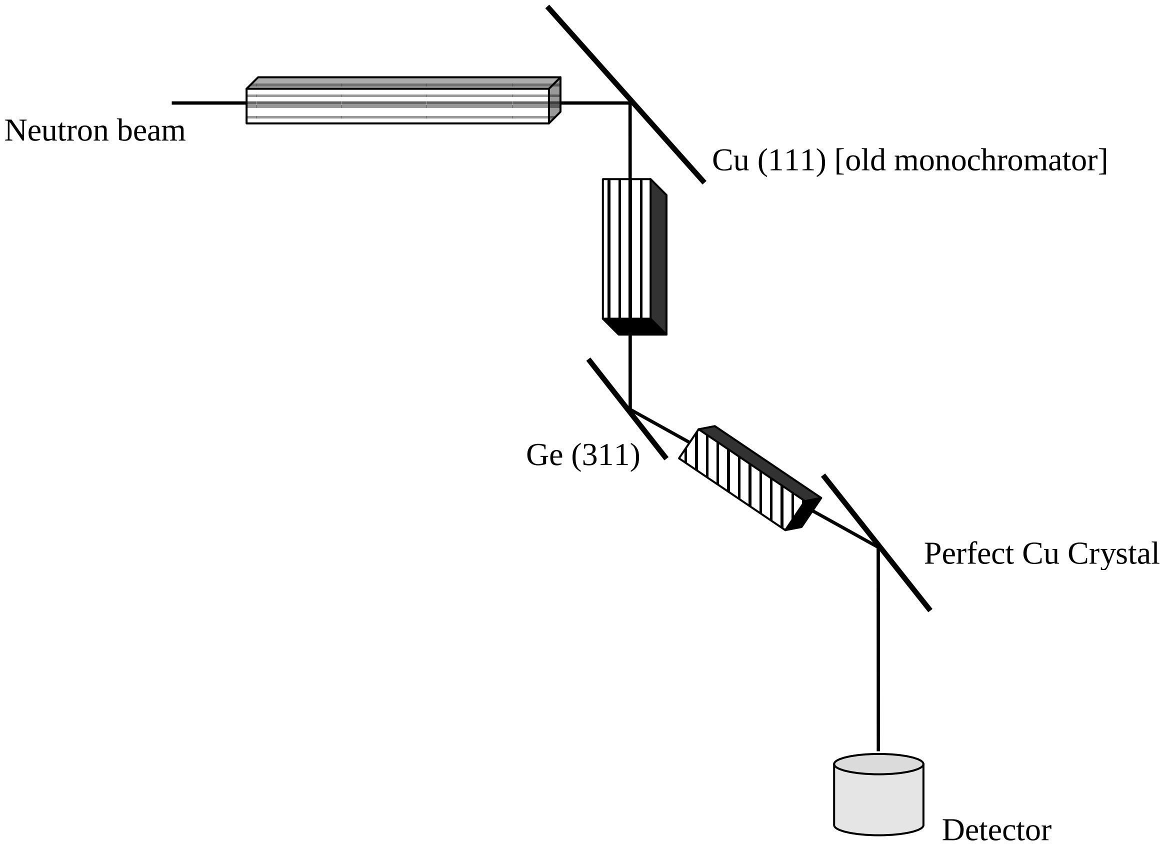

Fig:5.1 *Schematic of the set up used for measuring rocking curves of the crystals*

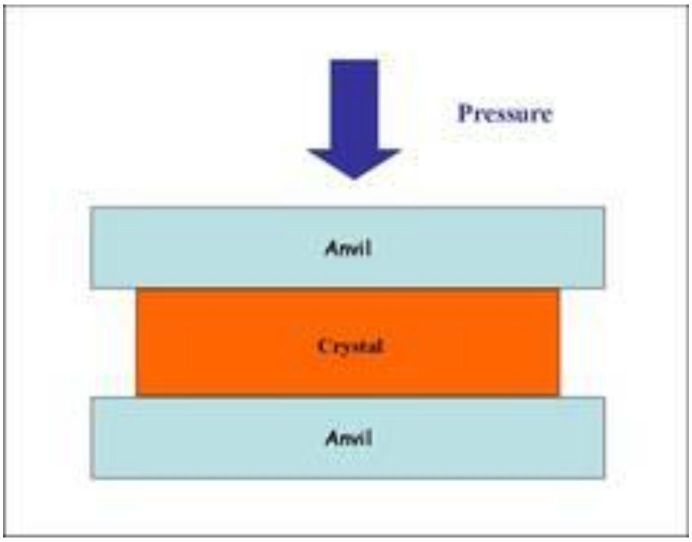

Fig.5.2 *Schematic for mechanical pressing of copper single crystals*

The neutron beam from reactor core is monochromatized using a Cu (111) crystal. Neutron beam of wavelength 1.65Å was used for the measurements. The incident beam has a divergence of about 1^o. In order to see the changes in the FWHM of the rocking curves of perfect copper crystals during compression it is essential to reduce the divergence of neutron beam. The divergent beam from the monochromator crystal is again reflected by a perfect Ge (311) crystal. The reflected beam from the Ge (311) crystal has divergence of 0.15^o. This beam is finally used for the measurements of rocking curves of perfect copper crystals.

Mechanical pressure was applied on the perfect Cu single crystals (35 mm × 25 mm × 10 mm) using hydraulic press as depicted pictorially in Fig. 5.2 [courtesy: www.ill.fr]. Load was applied along [111] axis that is perpendicular to the largest face, in steps with varying time. The size of the crystals is slightly large than the ram of the press so the copper crystals were placed between two machined stainless steel plates. This ensures that the load is distributed uniformly over the whole area of the crystal. Crystals were pressed under varying conditions of load and time.

As mentioned earlier, usual single crystals do not have a perfect regular sequence of atomic planes and unit cells throughout the whole volume of the crystal. They are permeated by dislocations which have the effect of dividing the crystal into smaller regions. These individual small regions (the mosaic blocks) are perfect themselves but are disoriented with each other. The extent of disorientation in a perfect crystal is of only few minutes. Application of load along [111] axis increases the misorientation among various mosaic blocks of perfect copper crystal. Since the components of neutron beam reflected from various mosaic blocks are not coherent, individual mosaic blocks reflect at slightly different angles when the crystal is rotated around the Bragg angle (of (111) planes, in our case). Hence the width of the rocking curve, which is a plot of intensity of the reflected beam as a function of angle of orientation of the crystal around the Bragg angle, increases. This increases overall reflectivity from the crystal. FWHM of the rocking curve is used to determine the mosaic spread.

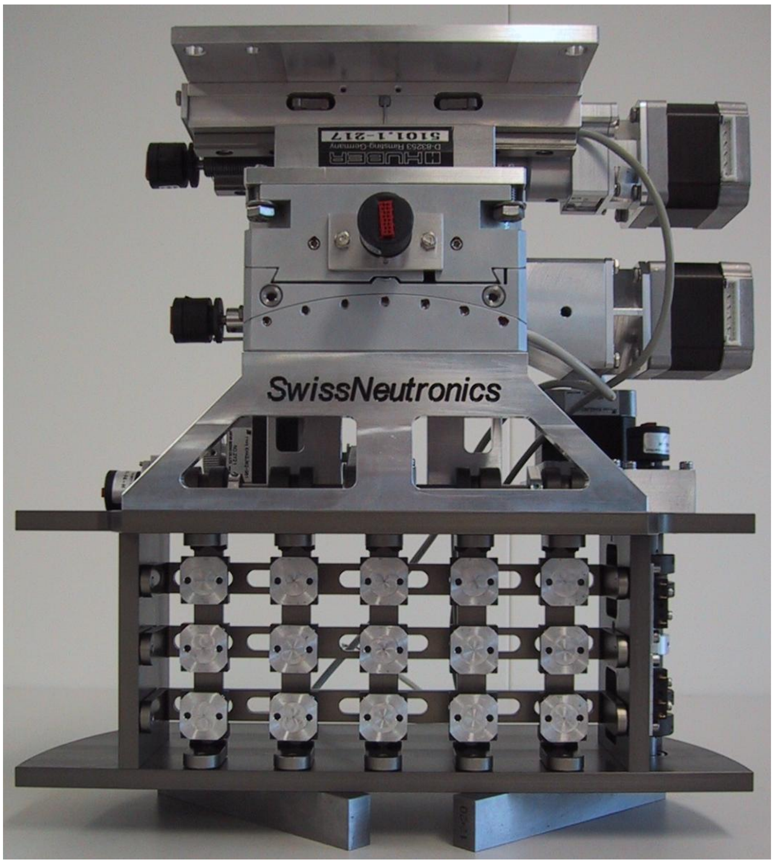

Fig. 5.3 Double focusing monochromator to be used on TAS, Dhruva.

5.3 Alignment of the copper crystals

The copper crystals that were mechanically treated to increase their mosaic spread were fixed on the 15 single crystal holders of the focusing monochromator assembly (Fig. 5.3) purchased from M/S Swiss Neutronics.

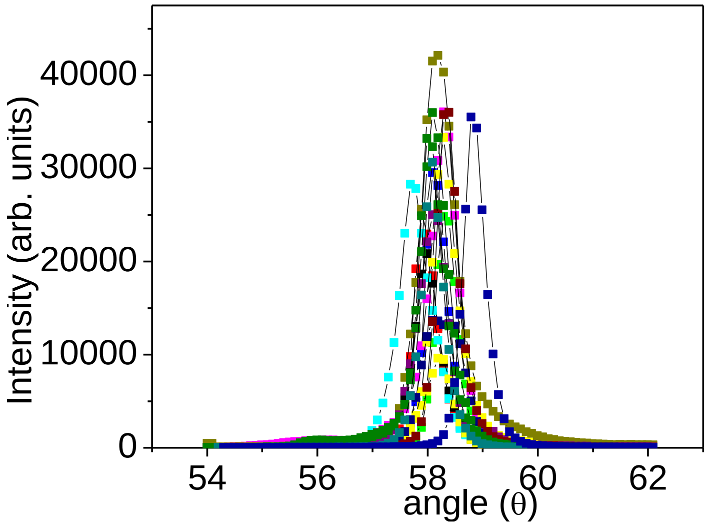

Fig.5.4 *Rocking curves of all the 15 crystals after mechanical treatment and alignment.*

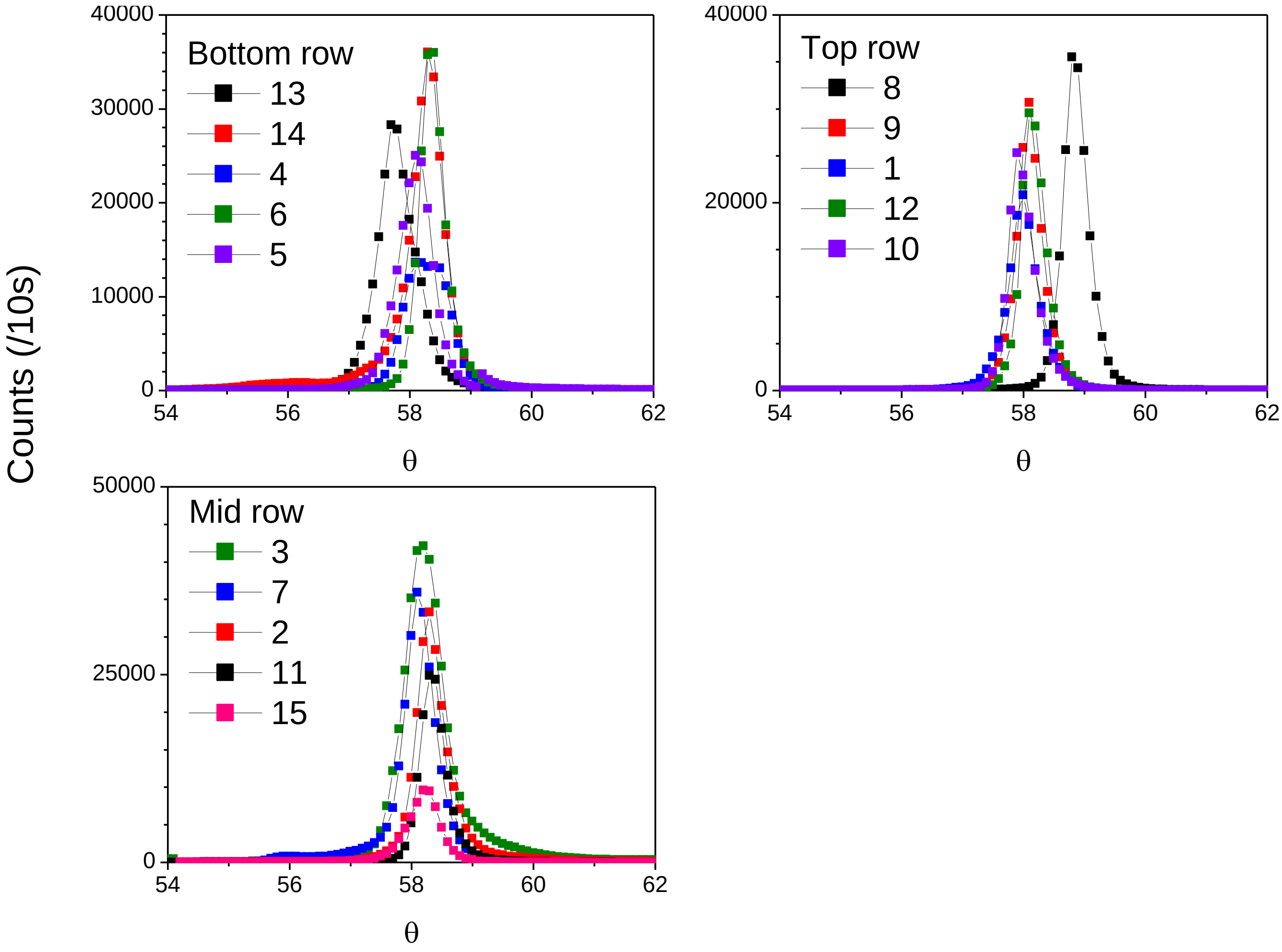

Fig.5.5 *Rocking curves of crystals placed in the different rows.*

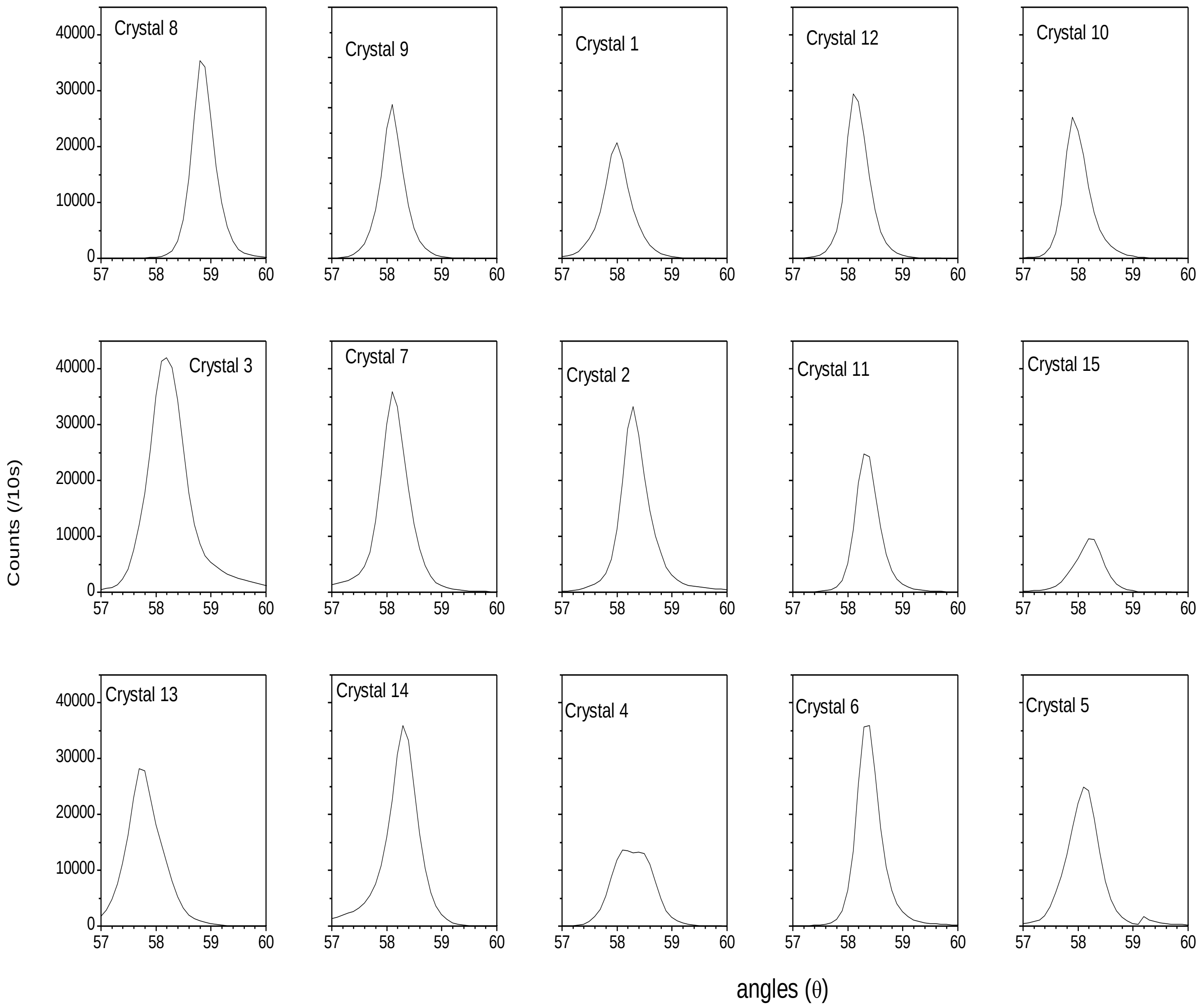

Fig. 5.6 *Rocking curves of the crystals after final alignment*

These crystals have a range of mosaic spread from 0.4° to 0.7°, as can be seen from in Fig.5.4 .The crystals with high reflectivity were placed at the centre of the assembly. Each of the fifteen crystal of the monochromator assembly was aligned using the neutron beam. The position of the neutron beam at the sample position is fixed. A mechanical jig was used to bring individual crystal at the centre of the neutron beam. The incident neutron beam size was reduced such that beam fall only on one of the crystals at a time. The vertical tilts of each of crystal were adjusted so as to maximize the neutron intensity reflected from the crystal. All the fifteen crystals were brought to the centre of the neutron beam and aligned individually. The rocking curve of each of the crystal in the three different rows is given in Fig. 5.5. The final schematic of the postions of the different crystals and their rocking curves are given in Fig.5.6. This set up is ready to be installed inside the monochromator shielding drum of the Triple Axis Spectrometer, TAS in Dhruva reactor.

References

[1] G. E. Bacon, *Neutron diffraction* (Oxford University Press, Oxford, 1975).

[2] L. D. Cussen, J. Appl. Cryst. 35, 702 (2002)

Chapter 6

Summary and future direction

6.1 Summary

The gist of this thesis is that a combination of lattice dynamics calculations, molecular dynamics simulations and inelastic neutron scattering measurements can be successful to study phonons in solids and their manifestations in macroscopic properties like specific heat, thermal expansion, diffusion and equation of state. The calculations have greatly aided the planning and execution of the various experimental measurements. The interatomic potentials have been used to understand the behavior of phonons at extreme conditions and the role of phonons in anamolous behavior of solids like superionic conductors at elevated temperatures. The calculations enabled to understand the microscopic picture of the dynamics of various solids leading to the manifestations of several unique properties.

Lattice dynamics studies have been done using empirical model potentials in case of all the compounds studied by the author. Empirical potentials makes most sense in studying phonons in the entire Brillouin zone in case of large compounds like YAG, which contain 240 atoms in an unit cell. First principle methods have been used to study Li_2O, $LiMPO_4$ and tungstates; the results of interatomic potential models are found to be in very good agreement with both first principle results and available experimental results. In case of superionic oxides and battery materials, high temperature diffusion has been studied using classical molecular dynamics simulations, as ab-initio molecular dynamics was not feasible. The model used for the molecular dynamics was formulated using calculated and experimental lattice dynamics results.

The salient features of this study are summarized below:

(1) A shell model has been successfully used to study the phonon properties of all the compounds studied. The interatomic potential is able to reproduce the elastic constants, bulk modulus, equilibrium lattice constant, and phonon frequencies, which are in good agreement with the reported data. The lattice dynamical studies for various compounds show that differences in the phonon spectra of various compounds of the same family arise from both the mass and potential variations. The calculated partial density of states helps us in understanding the dynamical contributions arising from various species of atoms in a compound.

(2) The measured neutron inelastic scattering data of $LiMPO_4$ (M = Fe, Mn) and AWO_4 (A = Sr, Ba, Pb and Ca) are in very good agreement with results of the interatomic potential developed. In case of $SrWO_4$, this model has been used to plan and execute the measurement of phonon dispersion relation using single crystal.

(3) The formulated interatomic potential has been used in the molecular dynamics simulations to understand the high temperature properties of the various compounds studied, like superionic conduction.. In case of superionic Li_2O, UO_2 this study is able to understand the microscopic pathway of diffusion. Instantaneous snapshots of the movement of lithium ions depict they move from one tetrahedral site to another via an

octahedral site, but they never occupy the octahedral site. The model has also been used to understand the role of phonons in the initiation of diffusion at elevated temperatures.

Similarly, studies on $LiMPO_4$ using neutron inelastic scattering experiments, potential model calculations on $LiMPO_4$ (M=Mn, Fe) at ambient and high temperature help to understand the microscopic picture of Li sub-lattice. Molecular dynamics simulations with increasing temperature indicate large mean square displacement of Li as compared to other constituent atoms. The computed pair-correlations between various atom pairs show that there is local disorder occurring in the lithium sub-lattice with increasing temperature, while other pairs show minimal changes.

(4) Lattice dynamics simulations have been carried out up to very high pressures in YAG, to understand the elastic stability of these compounds. At 100 GPa, YAG develops a large phonon band gap (90-110 meV) and its microscopic and macroscopic physical properties are found to be profoundly different from that at ambient pressure phase. There are significant changes in the high pressure thermal expansion and specific heat. The mode Gruneisen parameters show significant changes in the low energy range with pressure. The studies show that the YAG structure becomes mechanically unstable around P = 108 GPa due to the violation of the Born stability criteria. Although this does not rule out thermodynamic crossover to a lower free energy phase at lower pressure, this places an upper bound of P = 110 GPa for the mechanical stability of YAG.

(5) Molecular dynamics studies predict that all the four tungstates amorphize at high pressure. This is in good agreement with available experimental observations which show amorphization at around 45 GPa in $BaWO_4$ and 40 GPa in $CaWO_4$. With increase in pressure, there is a gradual change in the AO_8 polyhedra, while there is no apparent change in the WO_4 tetrahedra, But on amorphization, there is an abrupt increase in the coordination of the W atom while the octahedra around A atom is considerably distorted. The pair correlation functions of the various atom pairs corroborate these observations.

(6) Apart from the above mentioned details, this thesis also reports the involvement of the author in the pressing, testing and alignment of Cu-single crystals installed on the focusing double crystal monochromator. This setup is to be installed on the TAS, Dhruva, India.

6.2 FUTURE DIRECTION

The experience gained from the study of superionic conductors, $LiMnPO_4$, $LiFePO_4$ and their behavior with temperature will be of immense help in understanding the physics of several other technologically useful battery materials, wherein the phenomena of diffusion plays an important role. It would be worthwhile to understand the physics behind the novel properties exhibited by such technologically important compounds. The study of elastic instabilities in Y based garnets would help in better understanding of such phenomena in future. Pressure induced amorphization displayed by tungstates and phase transitions found in vanadates has definitely increased the depth of understanding of the response of compounds to pressure. A combination of experimental inelastic scattering, classical and first principle studies would provide an enriching treasure trove of knowledge. I would like to carry out a combination of ab-initio, classical lattice dynamics and molecular calculations along with experimental work to understand superionic and high temperature behavior in Bi_2O_3, Li based garnets like $Li_7La_3Zr_2O_{12}$ and other novel compounds. My aim would be to understand the mechanism of diffusion, role of phonons in initiation of diffusion and find its signature in the vibrational spectra with temperature. Knowledge of these basic phenomena would definitely be useful in the effective utilization of such oxides and compounds. The experience gained while working on instrument development would be worthwhile during future endeavors.